Modelling-Assisted Investigation of Degradation Phenomena in LSM-based SOFC Composite Cathodes

THÈSE N^O 5004 (2011)

PAR

Pietro TANASINI

$(\!(\text{PFL})$

ÉCOLE POLYTECHNIQUE
FÉDÉRALE DE LAUSANNE

Suisse
2011

Acknowledgments

First of all, I would like to gratefully thank Prof. Christos Comninellis and Dr. MER Jan Van herle for having given me the opportunity to do a thesis in EPFL on fuel cells, a very interesting and challenging subject. I have really appreciated their joint direction, each one giving me, in their own way, support, advices and trust during my research work. I would like to thank them both even more for sharing with me their experience on matters beyond the professional level; I always found their personal touch warm and comforting in many situations where I needed it.

This thesis has been financially supported by the SOF-CH, the Swiss SOFC Consortium, co-financed by the Swiss Federal Office of Energy (SFOE), contract number 152210 and Swisselectric Research, which are gratefully thanked for having made this work possible. We would like to express gratitude to our industrial partners SOFCpower Srl (Trento, I), HTceramix SA (Yverdon, CH) and Hexis Ltd. (Winterthur, CH) for the jointed collaboration, material supply and use of equipment. In particular, thanks are due to Stefano Modena, for his interest and useful advices. A special thank goes to Prof. Paola Costamagna from the University of Genova, for the fruitful and pleasant collaboration. Many thanks to Prof. Wilson Chiu from the University of Connecticut, both for the fruitful collaboration and for offering me the opportunity to spend a week in his laboratory, during which he and his collaborators didn't economize the efforts for making me feel at home.

Many thanks to Prof. Wilson K. S. Chiu, Prof. Lioubov Kiwi-Minsker, and Dr. Andreas Mai for accepting to review my thesis, as well as to Prof. Jacques Moser for presiding the thesis jury. Thanks also to all the people who reviewed earlier drafts of the work presented

To my grandfather, that is no more, and to my son, that will arrive soon

"Chacun appelle idées claires celles qui sont au même degré de confusion que les siennes propres."

– Marcel Proust

"An expert is a man who has made all the mistakes which can be made, in a narrow field."

– Niels Bohr

Abstract

This thesis focuses on the degradation pathways occurring in composite solid oxide fuel cell (SOFC) cathodes based on lanthanum-strontium manganite (LSM), combining modeling at the electrode level with experimental data. LSM composite electrodes are one of the most promising candidates for SOFCs cathodes, yet life-time is currently one of the limiting factors for the deployment of this technology. The combination of modelling tools and analysis of experimental data permitted to achieve a better *comprehension* of the mechanisms controlling the performance loss during operation and a *quantification* of the degradation.

By acquisition and formalization of knowledge of degradation processes, this thesis offers new tools to predict the life-time of a cell, hypothesize technological solutions for limiting the performance losses, and evaluate the impact of such solutions.

A *new experimental strategy* for SOFC button cell testing has been developed and validated during this work, namely the simultaneous operation of several cathode segments on the same cell support. This allowed, on the one hand, the production of reproducible and reliable data for the evaluation and investigation of degradation processes and, on the other hand, the possibility of rapid identification of experimental problems affecting one segment. The approach has been validated both experimentally and theoretically - through finite element calculations. The vast majority of the experimental results contained in this work has been obtained using this testing configuration.

Furthermore, *investigation techniques with unprecedented resolution in the SOFC research field have been developed* in collaboration between EPFL and external partners, namely a fast Cr quantification in operated cells, and 3D non-destructive reconstruction

of cathode microstructures by X-ray computed tomography, giving new instruments for the study of SOFC performance and degradation.

Finally, a set of data has been gathered concerning the reactivity of LSM-based systems, aging composite pellets for different times and temperatures and analyzing them with Rietveld-XRD, in order to map and assess the loss of performance caused by the formation of insulating phases in the electrode.

A steady-state electrode model present in literature has been selected and improved for simulating the performance of composite cathodes in presence of degradation phenomena, converting it into a *time-dependent model*. The first phenomenon that has been integrated is the variation of the microstructure of the composite electrode, allowing the prediction of variation in performance for a number of case studies: coarsening of only one phase, coarsening of both phases, coarsening of both phases with variation of porosity.

Experimental results obtained by microstructural analysis and electrochemical characterization of cells aged for different times were compared to the simulations of the correspondent case study, showing that *the morphological variation of the anode electrode in the early cell operation (first few hundreds hours) is well predicted* by the time-dependent model. No cathode morphological variation on this time scale could be detected.

Another degradation pathway analyzed was poisoning by Cr species. The phenomenon has been modelled assuming an *overpotential-driven deposition of Cr blocking species* on the electrode active sites. Validation has been performed comparing the simulations to Cr profiles obtained experimentally from cell tested for relatively short time (1000 h); one conclusion reached was that increased electrode thickness has a beneficial effect in limiting Cr poisoning.

The simulation was extended to operation times on the order of several 10 kh, difficult to achieve experimentally, describing the progressive deactivation of the electrode material. *The model provides an estimation of the expected life-time of an electrode and predicts quantitatively the performance loss during time*; this allows individuating technological solutions to hinder Cr poisoning, and the evaluation of the impact of such solutions. In

particular, it has been found that the conductivity and amount of the electrolyte phase are critical, and that a three-fold decrease of the degradation related to Cr poisoning is expected while passing from 50%LSM/50%YSZ (standard composition for most LSM based cathodes) to 42%LSM/58%ScSZ electrodes (new composition).

Finally, it has been found that cathode composition may have an indirect effect on the amount of deposited Cr: experimental evidences supporting a Mn-catalyzed deposition of Cr species have been found, suggesting that the presence of excess Mn in the cathode system can be detrimental.

KEYWORDS: solid oxide fuel cell, Cr poisoning, percolation, electrode micromodeling, LSM, cathode, composite electrode, degradation, 3D characterization, multicathode, segmented electrode, coarsening.

Résumé

Cette thèse se focalise sur les différents types de dégradation qui ont lieu dans les cathodes composites pour piles à combustible à oxyde solide (SOFC) à base de manganite de lanthane dopée au strontium (LSM), en combinant la modélisation avec des résultats expérimentaux. Les électrodes LSM composites sont des cathodes SOFC parmi les plus prometteuses, cependant la durée de vie est actuellement un des facteurs limitant l'application de cette technologie. La combinaison d'instruments de modélisation et d'analyse de résultats expérimentaux a permis d'atteindre une meilleure *compréhension* des mécanismes contrôlant la perte de performance et la *quantification* de la dégradation.

À travers de l'acquisition et formalisation de la connaissance des procédés de dégradation, cette thèse offre de nouveaux instruments pour prédire la durée de vie d'une cellule SOFC, envisager des solutions technologiques pour limiter la perte de performance, et évaluer l'impact de ces solutions.

Une *nouvelle stratégie expérimentale* pour le test de "button cells" SOFC a été développée et validée pendant ce travail, notamment la possibilité d'opérer simultanément plusieurs segments de cathode sur le même support cellule. Ceci a permis d'un côté la production de données reproductibles et fiables pour évaluer et investiguer les procédés de dégradation et, de l'autre côté, a donné la possibilité d'une identification rapide de problèmes expérimentaux affectant un des segments. Cette approche a été validée à la fois expérimentalement et théoriquement - à travers calcul par éléments finis. La plus grande partie des résultats expérimentaux a été obtenue en utilisant cette configuration de test.

De plus, *ont été développées des techniques d'investigation avec une résolution sans précédent dans la recherche sur les SOFC* en collaboration entre l'EPFL et des partenaires

externes, notamment une méthode de quantification rapide de contamination en Cr de cathodes et la reconstruction 3D non-destructive de la microstructure cathodique par tomographie numérique à rayons X. Ceci donne de nouveaux instruments pour l'étude de la performance et la dégradation des SOFC.

Enfin, un set de données a été recueilli concernant la réactivité de systèmes à base de LSM à travers le vieillissement de pastilles composites pour différents temps et températures et l'analyse XRD-Rietveld dans le but de cartographer et évaluer les pertes de performance causées par la formation de phases résistives dans l'électrode.

Un modèle d'état stationnaire présent en littérature a été selectionné et amélioré pour simuler la performance de cathodes composites en présence de phénomènes de dégradation, en le convertissant en un *modèle dépendant du temps*. Le premier phénomène intégré est la variation de la microstructure de l'électrode composite, permettant la prédiction de la variation de performance pour plusieurs cas d'étude: grossissement d'une seule phase, des deux phases, et frittage de deux phases avec variation de la porosité.

Des résultats expérimentaux obtenus par analyse de la microstructure et caractérisation électrochimique de cellules vieillies pour différent temps ont été comparés avec les simulations du cas d'étude correspondant, montrant que *la variation morphologique de l'anode au début du fonctionnement (les premières centaines d'heures) est bien décrite par le modèle*. En revanche, aucune variation morphologique de la cathode a pu être détectée pour cette échelle de temps.

La deuxième voie de dégradation analysée était l'empoisonnement par le chrome. Le phénomène a été modélisé en supposant une *déposition d'espèces bloquantes induite par le surpotentiel cathodique* sur les sites actifs de l'électrode. La validation de cette supposition a été faite en comparant les simulations aux profiles de Cr obtenus expérimentalement de cellules testées pour de temps relativement courts (1000 h); une conclusion a été que l'épaisseur accrue de la cathode a un effet bénéfique pour limiter l'empoisonnement par le Cr.

La simulation a été étendue pour des temps d'opération de l'ordre de plusieurs dizaines de milliers d'heures, difficilement accessibles expérimentalement, en décrivant la désactivation progressive du matériau cathodique. *Le modèle fournit une estimation de la durée de vie attendue de l'électrode, et prévoit quantitativement la perte de performance en fonction du temps*; ceci permet d'envisager des solutions technologiques pour limiter l'empoisonnement par le Cr, et l'impacte de ces solutions. En particulier, il a été trouvé que la conductivité et la quantité de la phase électrolyte dans le composite sont des paramètres fondamentaux, et l'on prévoit une durée de vie trois fois plus élevée en passant de 50%LSM/50%YSZ (composition standard pour beaucoup de cathodes à base d'LSM) à électrodes composés de 42%LSM/58%ScSZ (nouvelle composition).

Enfin, il a été trouvé que la composition cathodique peut influencer indirectement la quantité de Cr déposé: des preuves expérimentales supportent l'hypothèse d'une déposition de Cr catalysée par le Mn, ce qui suggère que la présence d'un excès de Mn dans la cathode peut être préjudiciable.

MOTS-CLÉS: pile à combustible à oxyde solide, empoisonnement au Cr, percolation, micro-modélisation, LSM, cathode, électrode composite, dégradation, characterisation 3D, multicathode, électrode segmentée.

Sommario

Questa tesi si focalizza sulle diverse vie di degradazione che hanno luogo nei catodi compositi a base di manganite di lantanio-stronzio (LSM) per pile a combustibile ad ossidi solidi (SOFC), combinando la modellizzazione con risultati ottenuti sperimentalmente. Nonostante gli elettrodi LSM compositi siano tra i migliori candidati come catodi per le SOFC, la loro non sufficiente durabilità impedisce una diffusione tecnologica su larga scala. La combinazione di strumenti di modellizzazione e di analisi di risultati sperimentali ha permesso di raggiungere una migliore *comprensione* dei meccanismi che controllano la perdita di prestazione e di *quantificare* la degradazione.

Attraverso l'acquisizione e la formalizzazione di conoscenza sui processi degradativi, questa tesi offre dei nuovi strumenti per prevedere la durata di vita di una cella SOFC, per ipotizzare delle soluzioni tecnologiche al fine di limitarne la perdita di prestazione, e per valutare l'efficacia di queste soluzioni.

Durante questo lavoro, una *nuova strategia sperimentale* per i test "button cell" SOFC è stata sviluppata e convalidata, consistente nel test simultaneo di più segmenti di elettrodo sullo stesso supporto. Questo ha permesso da un lato la produzione di dati riproducibili e affidabili per valutare e studiare i processi degradativi e, d'altro lato, ha fornito la possibilità di un'identificazione rapida di problemi sperimentali eventualmente presenti su uno dei segmenti. Questo approccio è stato convalidato sia sperimentalmente che dal punto di vista teorico - attraverso il calcolo col metodo degli elementi finiti. La maggior parte dei risultati sperimentali di questo lavoro sono stati ottenuti usando questa configurazione di test.

Inoltre, *sono state sviluppate delle tecniche di ricerca con una risoluzione senza prece-*

denti nella ricerca sulle SOFC, in collaborazione con partners sia interni che esterni all'EPFL, e in particolare un metodo di quantificazione rapida del Cr in celle dopo operazione e la ricostruzione 3D non distruttiva della microstruttura catodica attraverso la tomografia computerizzata a raggi X. Ciõ fornisce nuovi strumenti per lo studio delle prestazioni e degradazione delle SOFC.

Infine, un insieme di dati preliminari è stato ottenuto riguardo alla reattività di sistemi a base di LSM, eseguendo un invecchiamento di pastiglie composite a diversi tempi e temperature e un'analisi XRD-Rietveld, al fine di aprire nuove prospettive per lo studio delle perdite di prestazione dovute alla formazione di fasi resistive nell'elettrodo.

Un modello allo stato stazionario presente in letteratura è stato selezionato e migliorato per simulare la prestazione di catodi compositi in presenza di fenomeni degradativi, convertendolo in un modello dipendente dal tempo. Il primo fenomeno integrato è la variazione della microstruttura dell'elettrodo composito, arrivando alla predizione della variazione della prestazione in vari casi: ingrossamento di una delle due fasi, di entrambe le fasi ed infine sinterizzazione di entrambe le fasi con diminuzione della porosità.

I risultati sperimentali ottenuti dall'analisi della microstruttura e dalla caratterizzazione elettrochimica di celle operate per tempi diversi sono stati comparati con le simulazioni del caso corrispondente, mostrando che *la variazione morfologica dell'anodo all'inizio dell'operazione (le prime centinaia di ore) è ben descritta dal modello*. Nessuna variazione morfologica del catodo è stata osservata nell'arco temporale in cui l'esperimento è stato condotto.

La seconda via di degradazione analizzata è l'avvelenamento al cromo. Il fenomeno è stato modellizzato assumendo una *deposizione di specie bloccanti indotto dalla sovratensione* sui siti attivi dell'elettrodo. La convalida di questa ipotesi è stata eseguita comparando le simulazioni ai profili di Cr ottenuti sperimentalmente da celle operate per tempi relativamente brevi (1000 ore); un risultato intermedio è la verifica di un effetto benefico dello spessore dell'elettrodo nel caso in cui sia presente il Cr.

La simulazione è stata successivamente estesa per tempi di operazione dell'ordine di varie decine di migliaia d'ore, difficilmente realizzabili dal punto di vista sperimentale, descrivendo la disattivazione progressiva del materiale elettrodico. Il modello fornisce una stima della durata di vita attesa, e predice quantitativamente la perdita di prestazione in funzione del tempo; questo permette di ipotizzare delle soluzioni tecnologiche per limitare l'avvelenamento al Cr e di stimarne l'efficacia. In particolare, è stato trovato che la conduttività e la quantità della fase elettrolita nel composito sono dei parametri fondamentali, e si prevede una triplicazione della durata di vita passando da 50%LSM/50%YSZ (composizione standard per molti catodi a base d'LSM) a elettrodi composti di 42%LSM/58%ScSZ (nouva composizione).

Infine, è stato riscontrato che la composizione del catodo può aver un effetto indiretto sulla quantità di Cr che si deposita: in effetti, sono state trovate prove sperimentali che sostengono l'ipotesi di un meccanismo di deposizione del Cr catalizzato dal Mn, il che suggerisce che un eccesso di Mn nei catodi potrebbe avere effetti negativi.

PAROLE-CHIAVE: pila a combustibile a ossidi solidi, avvelenamento al Cr, percolazione, micro-modellizzazione, LSM, catodo, elettrodo composito, degradazione, caratterizzazione 3D, multicatodo, elettrodo segmentato.

Contents

RESULTS AND DISCUSSION 63

4 Degradation by morphological change 65

5 Degradation by chromium poisoning 99

6 Other cathode degradation and analysis aspects 137

7 Conclusion and perspectives 163

List of symbols

Acronyms

10GDC gadolina-doped ceria: 10% Gd_2O_3 - 90% CeO_2

10ScSZ scandia-stabilized zirconia: 10% Sc_2O_3 - 1% CeO_2 - 89% ZrO_2

8YSZ yttria-stabilized zirconia: 8% Y_2O_3 - 92% ZrO_2

AC   alternate current

ASR   area specific resistance

CCD   charge coupled device

CCL   current collection layer

CGO   gadolina-doped ceria: Gd_2O_3-CeO_2

CIME   centre interdisciplinaire de microscopie électronique

CSD   cumulative size disribution

DEM   discrete element method

EDX   energy-dispersive X-ray (detector)

EPFL   École Polytechnique Fédérale de Lausanne

EsB   energy selective back-scattered electrons

EsBSE energy selective back-scattered secondary electrons

FG   functionally graded

FIB   focused ion beam

LBM   lattice Boltzmann method

LSCF lanthanum-strontium cobaltite-ferrite: $La_xSr_{1-x}Co_yFe_{1-y}O_{3-\delta}$

LSM   lanthanum-strontium manganite: $(La_xSr_{1-x})_yMnO_{3\pm\delta}$

LSM25 lanthanum-strontium manganite: $(La_{0.75}Sr_{0.25})_{0.95}MnO_{3\pm\delta}$

LSM30 lanthanum-strontium manganite: $(La_{0.70}Sr_{0.30})_{0.90}MnO_{3\pm\delta}$

LSM35 lanthanum-strontium manganite: $(La_{0.65}Sr_{0.35})_{0.95}MnO_{3\pm\delta}$

MIC   metallic interconnector

MIEC mixed ionic-electronic conductor

MLEM maximum-likehood expectation maximisation

ORR   oxygen reduction reaction

PAA   poly-acrylic acid

PDF   powder diffraction file

PSD   particle size distribution

RVE   representative volume element

ScSZ scandia-stabilized zirconia: Sc_2O_3-ZrO_2

SEM   secondary electron microscopy

SOFC solid oxide fuel cell

TPB   triple phase boundary

TXM   transmission X-ray microscope

XCT   x-ray computed tomography

YSZ   yttria-stabilized zirconia: Y_2O_3-ZrO_2

Roman Symbols

A active area per unit volume [m^2 m^{-3}]

a electrode thickness [m]

a_{CCL} current collector layer thickness [m]

ASR area specific resistance [Ω m^2]

C capacitance [C V^{-1}]

C concentration [mol m^{-3}]

C^* bulk concentration [mol m^{-3}]

C^0 concentration in the feeding gas [mol m^3]

D diffusivity [m^2 s^{-1}]

$d_{v,50}$ volumetric average diameter [m]

F Faraday's constant, 96484 [C mol^{-1}]

f frequency [s^{-1}]

h oxide scale thickness [m]

i current density [A m^{-2}]

$i_{0,Cr}$ exchange current density for the electrochemical deposition of Cr [A m^{-2}]

i_0 exchange current density [A m^{-2}]

i_n transfer current density per unit of active area [A m^{-2}]

I_{tot} overall current density [A m^{-2}]

j_{Cr} current density related to the Cr deposition [A m^2]

k kinetic constant [s^{-1}]

M molar mass [kg mol^{-1}]

N number of particles [-]

n adimensional factor defining the deviation of a capacitor from the ideal case [-]

n fraction number of particles [-]

n^* overall number of particles per unit volume [m^{-3}]

o probability of occupation [-]

P $\frac{r_m}{r_i}$ ratio [-]

p_k probability of belonging to a percolating cluster of a generic phase k [-]

q_{Cr} deposited Cr [mol m^{-2}]

R gas constant [J mol^{-1} K^{-1}]

R resistance [Ω]

r particle radius [m]

r ratio between final and initial porosity $\varepsilon^{min}/\varepsilon^0$ [-]

$R_{\mathrm{Cr},tot}$ total rate of Cr deposition [mol s^{-1}]

$r_{\mathrm{Cr},tot}$ Cr deposition rate per unit of electrode surface [mol m^{-2} s^{-1}]

$R_{C_{\mathrm{CrO_2(OH)_2}}}$ reaction rate for Cr oxide-hydroxide deposition per unit volume of electrode [mol m^{-3} s^{-1}]

r_{Cr} reaction rate for Cr deposition per unit area of active surface [mol m^{-2} s^{-1}]

T temperature [K]

t time [s]

t_{cb} time of blocking of the electrode/electrolyte interface [s]

V phase volume [m^3]

V potential [V]

x spatial coordinate along the electrode thickness [m]

y gas molar fraction [-]

Z average coordination number [-]

Z impedance [Ω]

Z_{xy} average number of contacts that particles of phase x have with particles of phase y [-]

δZ_{real} Jensen function. Derivative of Z_{real} with respect to ln$f$ [Ω]

Greek Symbols

β symmetry factor [-]

η local overpotential [V]

η_0 overall electrode overpotential [V]

Γ dimensionless variable defined in Eq. 2.30 [-]

γ dimensionless parameter defined in Eq. 2.22 [-]

μ dimensionless parameter defined in Eq. 2.19 [-]

ω period [s^{-1}]

Φ Thiele modulus [-]

ρ resistivity [Ω m]

σ conductivity [S m^{-1}]

τ_s characteristic time [s]

θ contact angle [°]

θ phase difference [rad]

ε porosity [-]

φ volume fraction [-]

ξ adimensional parameter defined in Eq. 4.6 [-]

τ_{pore} pore tortuosity [-]

Subscripts

c critical

el electronic conductor phase

i inclusion phase

$imag$ imaginary part

io ionic conductor phase

j, k phase in a composite

m matrix phase

max maximum

min minimum

p product

r reactant

$real$ real part

tot total

Superscripts

0 initial

eff effective value, taking into account the effect of the microstructure

eq equilibrium

Preface

I have the impression that most people perceive a scientist as a person that first thinks intensively in his office, maybe with complicated mathematical formulae, comes up with a Bright Idea, goes to the lab to do the Right Experiment, and finds The Invention.

It is also my opinion that even undergraduate students are conditioned by the protected environment that professors and assistants create for them, making the best effort to provide them knowledge presented in the most clear and ordered way. They are used to the fact that a fair amount of effort will correspond to a fair result, they may be comforted and flattered by the good marks they obtained during the examinations, and they suppose it will be the same during a PhD; at least, this was my case - before beginning my thesis.

Well, I found out that both these visions don't accurately describe the activity of a researcher, at least not the researchers I've met (including myself). There are no exams or good marks in the everyday life, nor Right Experiments that bring immediate and definitive results.

The first big difference with the student life is that you are alone. Accompanied and advised by your supervisor, colleagues, collaborators and the scientific community in which you work, but nevertheless independent in most of your choices. Probably a good school of life, yet sometimes difficult.

Another element is that the objective is far if not vague, and it is more difficult to find the path than actually walking through it. For most of the chemists I know, this was a frustratingly slow process, obtained through the "fornication with the matter" (Primo Levi): two steps forward, one step backwards. In effect, another unexpected fact is that results obtained one day can contradict those obtained the following day. This can be

due to an erroneous assumption you made, justified by one experiment but refuted by the other. But there is another option: one (or both) experiments were somehow wrong. One day I estimated that if every component of my installation (thermocouples, controllers, PC, etc. for a total of roughly 30 elements) had a 99.9% chances of working correctly each day, there would only be a 30% probability that, at the end of a 1000-hours experiment, nothing had failed. Indeed, in my four-year thesis, many experiments had some failure which, depending on the gravity, implied the acquisition of partial data or the complete loss of the test.

To describe my personal vision I figured out a metaphor: the research in a PhD is like a labyrinth run for a lab rat seeking a piece of cheese. In my opinion, a student willing to begin a PhD should be aware of what awaits her/him. I wasn't; and still, I think the cheese is worth the run.

Chapter 1

Introduction

This thesis focuses on the study of cathodic degradation pathways in solid oxide fuel cells (SOFC), combining modeling with experimental data.

The aim of a thesis centered on a technological device is to achieve both a theoretical understanding of the system and a quantification of the phenomena, and finally to suggest solutions for improving the device.

On the one hand, a number of modifications were applied to an existing steady-state micro-model, in order to introduce the variation of performance caused by time-dependent degradation processes. The modeled degradation processes include the variation of the electrode microstructure and the poisoning by chromium species. The modelling gives the advantage of providing predictions on the performance loss and the expected life-time of an electrode on a scale of several dickers of thousands of hours of operation, which are difficult and expensive to achieve experimentally.

On the other hand, experimental data were gathered in a complementary way, with cells operated in controlled conditions for thousands of hours, in order to validate the predictions obtained by modeling and to provide a starting point for implementing more elaborate models.

The parallel advancement of modelling and experimental work permitted to achieve (and required) a comprehension of:

- how the single degradation phenomenon happens

- how it modifies the system

- how and how much this impacts on the functionality of the electrode

Thus, the essence of this work resides in the use of experimental techniques, some of which were developed during this thesis, to support and validate the modelling of the degradation phenomena in a SOFC cathode.

1.1   Context and motivation

Over the past few years, clean energy conversion has become increasingly important. On the one hand, this is reflected by the establishment of several international agreements such as the Kyoto Protocol [1], and on the other hand, by an increasing public awareness concerning climate change and the greenhouse effect. Among the numerous ways to reduce the emissions of carbon dioxide and pollutants, two of the simplest ones are the improvement in efficiency of energy conversion devices and the adoption of zero-emission fuels such as hydrogen obtained from renewable resources. In applications where small or medium energy amounts are required, fuel cells are currently considered as a possible answer to such demands.

Solid oxide fuel cells are high-temperature fuel cells (600–1000 °C). They are constituted by ceramic or cermet electrodes separated by a dense membrane of an ion-conducting ceramic [2] such as u-stabilized zirconia (YSZ); high temperature is necessary to guarantee sufficient ionic conduction of the electrolyte and good activity of the electrodes.

Operating at high temperature leads to a number of advantages: high activity of the Ni used as anode catalyst (instead of the noble metals that are necessary at lower temperature) and high flexibility of the fuels that can be used (natural gas, syn-gas, H_2 and CH_3OH in a wide composition range). For the cathode catalyst, relatively inexpensive materials like lanthanum-strontium manganite (LSM), a ceramic perovskite, can be used instead of Pt. Moreover, the heat that is released during operation has high energy

value and can be converted or used in several ways. However, although operating at high temperature leads to such advantages, the drawback lies in the fact that harsher conditions cause the SOFC to steadily decrease their performance during operation, and thus their conversion efficiency is reduced with time [3]. A clear understanding of all deactivation phenomena has not been reached yet [4]. Cell degradation may be considered as the greatest technological issue prior to SOFC commercialization and the target life-time should be extended to at least 40.000 hours of operation [5] for products introduced into the market.

As SOFC life-time is a key issue for introduction into the market, several solutions have been proposed in the last years to hinder deactivation processes while maintaining or even increasing the performances. From a materials point of view, the quality of the raw materials has been improved to limit segregation of impurities, and the catalyst electrodes as well as their compositions have been tuned to limit the formation of foreign phases. From a technical point of view, system components, like metallic interconnectors or heat exchangers, have been chosen or treated to limit the emission of pollutants. Furthermore, operating conditions (e.g. temperature, fuel utilization, cell overpotential) are optimized to limit degradation. Nevertheless, degradation phenomena are reduced, but not completely eliminated and life-time is still an issue from an industrial point of view.

As a consequence of the recent improvements allowing to achieve performance losses below 1% over 1000 h of continuous operation, the study of slow, simultaneous, interrelated degradation mechanisms is difficult due to the long testing time needed to measure significant variations in performance; further, the separation and quantification of the contributions of each phenomenon is even more challenging.

Degradation studies need robust and stable test benches permitting to identify changes on the order of 1% after months of aging. Operating conditions must be rigorously the same for all the tests of an experimental campaign, since even small changes in temperature or gas distribution affect the cell behavior and mask the influence of a given studied variable. Reproducibility and testing time are key issues in SOFC research.

In this context, modelling is not only the natural formalization of new knowledge, but

also a necessary tool to limit the number and the extension of the aging experiments and to give predictions on time scales hardly reachable in the laboratory.

The *finality of this work* is to *provide experimentally validated models* that **describe** the degradation processes, **predict** the performance loss, and **indicate solutions** for further improvement. As a parallel objective there is the *development of new experimental techniques* permitting to **achieve a better understanding** of such processes and opening new perspectives for further studies.

1.2   Structure of the present work

The present thesis is articulated around the combined use of modelling and experimental tests in order to develop an understanding of the degradation phenomena in SOFC cathodes, quantify them, and suggest possible solutions to hinder or eliminate the performance loss during operation.

In Chapter 2, a review of the current state of the art in the study of SOFC cathodic degradation mechanisms and characterization techniques is presented. Particular attention has been paid to the description of a model, based on percolation theory, describing SOFC electrodes.

In Chapter 3 the emphasis is put on the experimental techniques, some of which were developed during this thesis.

A new experimental strategy for SOFC button cell testing has been developed and validated, namely the simultaneous operation of several electrode segments on the same support. This allowed, on the one hand, the production of reproducible and reliable data for the evaluation and investigation of degradation processes and, on the other hand, the possibility of rapid identification of experimental problems affecting one segment. The approach has been validated both experimentally and theoretically - through finite element calculations.

A fast Cr quantification in operated cells developed at EPFL is shown, permitting to recover the concentration profile of deposited Cr species from operated cells.

In Chapter 4, the percolation-based steady-state electrode model described in Chapter 2 is improved for simulating the performance of composite cathodes in presence of morphological variation, converting it into a time-dependent model. The model allows predicting the variation in performance for a number of case studies: coarsening of only one phase, coarsening of both phases, coarsening of both phases with variation of porosity.

Experimental results obtained by microstructural analysis and electrochemical characterization of cells aged for different times is compared to the simulations of the correspondent case study, showing that the morphological variation of the anode in the early cell operation (few hundreds hours) is well predicted by the time-dependent model.

In Chapter 5 the cathode poisoning by chromium species is analyzed. The phenomenon has been modeled assuming a overpotential-driven deposition of Cr species blocking the cathode active sites. The validation of this assumption has been performed comparing the simulations to Cr profiles obtained experimentally from cells tested for relatively short time (1000 h); an intermediary conclusion achieved was that the electrode thickness has a beneficial effect towards limiting Cr poisoning.

The simulation was extended to operating times on the order of several 10 kh, difficult to achieve experimentally, describing the progressive deactivation of the electrode material. The model provides an estimation of the expected life-time of an electrode and predicts quantitatively the performance loss during time; this allows individuating technological solutions to hinder the Cr poisoning, and the evaluation of the impact of such solutions. In particular, it has been found that the conductivity and amount of the electrolyte phase are critical for extending the life-time.

Chapter 6, presents additional results obtained during the thesis that open interesting perspectives for further investigation.

Within a collaboration with the University of Connecticut, a 3D non-destructive reconstruction of cathode microstructures has been developed by X-ray computed tomography

with unprecedented resolution in the SOFC research field. The results have been compared with those obtained independently by FIB nanotomography performed at EPFL and show the possibility to perform high resolution microstructural characterization as an investigation method to understand and quantify degradation processes.

Furthermore, a set of data has been gathered concerning the reactivity of LSM-based systems, aging composite pellets for different times and temperatures and analyzing them with Rietveld-XRD, in order to propose new perspectives for the quantitative study of the loss of performance caused by the formation of insulating phases in the electrode.

Finally, other results indicate that Cr is deposited via a Mn-Cr intermediate. As a direct consequence, we believe that the presence of Mn in the cathode can have a detrimental effect in the case of presence of volatile Cr species.

Chapter 2

Bibliography

In this Chapter, the current state of the art in the study of SOFC cathodic degradation mechanisms and characterization techniques is presented. In subsequent sections, particular attention is paid to the discussion of the percolation theory and a percolation-based model of the electrodes (Section 2.2) that has been used as a basis for the modelling work in this thesis.

2.1 The solid oxide fuel cell

2.1.1 Operating principle

Fuel cells convert the chemical energy involved in the combustion of fuel with an oxidant (usually air) directly into electrical energy through an electrochemical reaction. The electrochemical conversion is not subject to the thermodynamic limitations typical of combustion engines, has a excellent thermodynamic efficiency (50-90%) and a high final efficiency in real devices (up to 40-60% [6]).

Fuel cells are generally composed of two compartments containing fuel and air, which are separated by a dense, impermeable and electronically insulating membrane. This membrane must be ionically conductive and, in solid-state electrochemistry, has the same

9

function as the liquid electrolyte in classical electrochemistry i.e. connects the two compartments by carrying an ionic current.

Fuel cells are mostly classified following the type of material used for this solid electrolyte membrane. Operating temperature, performance and degradation issues and most relevant technological aspects are related to this element. Solid oxide fuel cells are characterized by the use of a ionic conductive ceramic; since the ionic conductivity is acceptable only at relatively high temperature, SOFCs are designed to operate between 600°C and 1000°C.

The electrochemical reaction occurs, split into two half reactions, on the porous, electronic conducting electrodes that are deposited on both sides of the solid electrolyte. The electrochemical reactions occur in an area defined by the immediate proximity of the electronic conductor, ionic conductor and gas phases and therefore defined triple-phase boundary, TPB. The need of the simultaneous presence of the three phases is due to the necessity of the transport of electric current, ionic current and gaseous reacting species that participate in the electrochemical reaction. In order to increase the extension of the TPB, the composition is often obtained by mixing phases, one of which is the electronic conductor and electrocatalyst, and the other the ionic conductor i.e. an extension of the electrolyte inside the electrode.

A number of different types of SOFC exist, depending of the material choice for the electrodes and the electrolyte: the cathode can be composed by of lanthanum-strontium manganite (LSM), on which this thesis is focused, presenting the advantage of generally good stability, good electronic conductivity and catalytic activity but a very limited ionic conductivity. Other possible cathode materials include perovskites like lanthanum cobaltites or cobaltites-ferrites, also containing La,Sr on the A-site; these are ionic-electronic conductive (MIEC) perovskites have often higher electronic conductivity and higher catalytic activity; the ionic conductivity allows the reaction not to be confined to the TPB only and therefore it is not necessary to mix the perovskite in a composite with a ionic conductor. Unluckily, they are usually more reactive, requiring milder operating conditions and a careful choice of other materials so as not to undergo fast degradation.

The electrolyte of choice is often zirconia which, in order to be conductive, must be stabilized in the cubic phase with yttrium (yttria-stabilized zirconia, YSZ) or scandium oxide (scandia-stabilized zirconia, ScSZ). It has a relatively good intrinsic stability, but tends to react with LSM to a certain extent, and it is very reactive towards MIEC perovskites. Alternatively, ceria-doped gadolina (CGO) could be used, having a better stability towards all perovskites; but this material develops electronic conductivity under reducing conditions, and cannot be used as a thin dense electrolyte, due to short-circuiting the cell when exposed to the reducing atmosphere on the anode side. It is usually used as an interlayer between the reactive MIEC perovskites and a zirconia-based electrolyte.

The most commonly used anode is a Ni-based composite, containing as a ionic conductor either stabilized zirconia or CGO in order to extend the TPB area and, at the same time, consolidate the microstructure against sintering of the metallic Ni particles. CGO has the additional advantage of being an electronic conductor in hydrogen-rich atmospheres. A last element differentiating SOFCs is the choice of the element giving the mechanical support to the cell. Anode-supported cells rely on a layer of 200 to 1000 µm of Ni-electrolyte composite, while electrolyte-supported cells consist in thin electrodes deposited on a relatively thick electrolyte ($\geq$ 150 µm). The electrolyte supports present a higher ohmic resistance for the transport of the ionic current from one compartment to the other; on the other hand, anode supports can have fuel diffusion limitations because of their thickness and can present mechanical failures if sudden oxidation occurs, causing a deformation and the formation of cracks.

The operating principle of SOFC is shown in Figure 2.1, using as an example a LSM/YSZ cathode, a YSZ electrolyte and a Ni/YSZ anode. The oxygen of the air diffuses in the pores of the cathodes until it reaches the TPB; the oxygen reduction reaction (ORR) occurs involving electrons delivered by the electronic conductor. The oxygen ions produced (O^{2-}) are integrated in the ionic conductor nearby, then carried through the electrolyte membrane, and finally delivered to the anode side. In the anode compartment the oxidation of the fuel takes place (commonly H_2 and/or CO), the counter-diffusion of reactants and products in the pores and the transport of electrons to the external circuit.
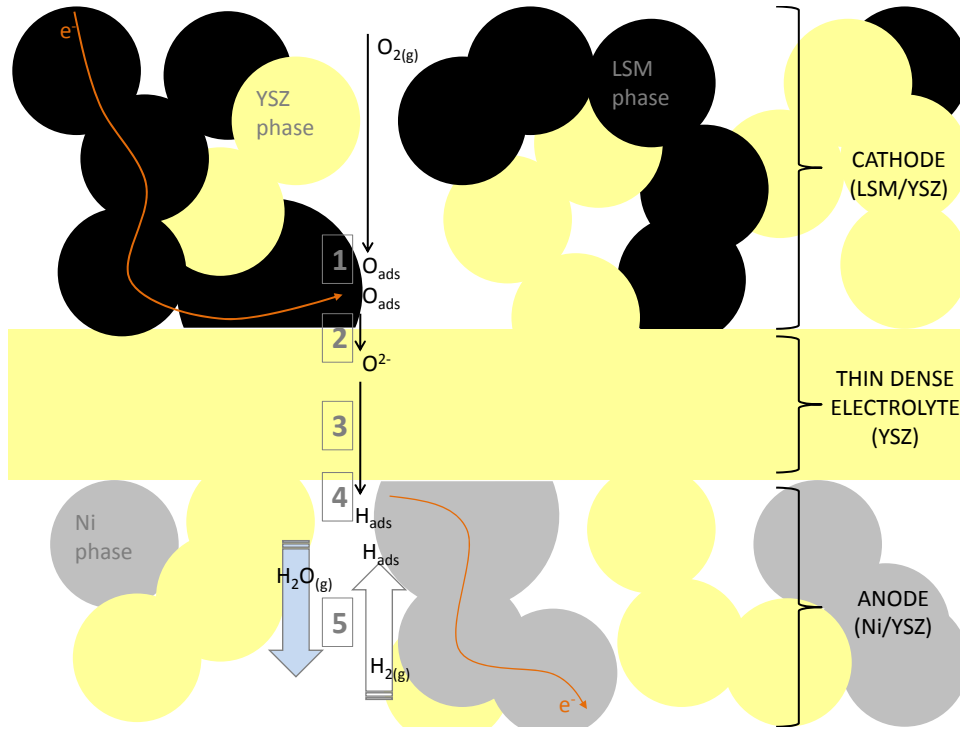
Figure 2.1. Reaction scheme for a SOFC composed by LSM/YSZ cathode, YSZ electrolyte and Ni/YSZ anode. ⬤YSZ phase ⬤LSM phase ⬤Ni phase. 1) $O_{2(g)}$ adsorption/dissociation 2) Oxygen transfer at the LSM/YSZ interface 3) O^{2-} conduction in the electrolyte 4) Charge transfer at Ni/YSZ interface 5) Diffusion in the gas phase of $H_{2(g)}$ towards the dense electrolyte and $H_2O_{(g)}$ towards the anode surface.

The difference in electrochemical potential between anode and cathode gas composition builds up the difference in electrical potential between the two electrodes, exploitable to provide electrical power.

The two half reactions, in the case of hydrogen as a fuel, are:

$$O_{2,(g)} + 4e^- \rightarrow 2O^{2-}_{YSZ} \tag{2.1}$$

$$O^{2-}_{YSZ} + H_{2,(g)} \rightarrow H_2O_{(g)} + 2e^- \tag{2.2}$$
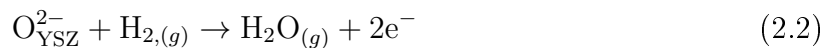
In reality, the two half reaction are decomposed into several intermediate steps involving adsorption, diffusion and charge transfer processes, as also indicated in Figure 2.1. The

exact sequence of elementary steps and transport paths and their relative importance on the overall kinetics depends on the gas composition, the materials used and the operating conditions [7, 8, 9].

One of the main advantages of SOFCs is the possibility to use a variety of fuels, in particular methane (natural gas or bio-gas), methanol, ethanol etc. In this case, the oxidation reaction requires a fuel processing step before the electrochemical conversion (partial oxidation or reforming). The pre-processing can be done at least partially in a separate unit before the SOFC, but at high temperature, reforming can be induced also inside the anode support since Ni is a good reforming catalyst. In fact, CH_4 can be converted to CO and H_2 through reactions 2.3 to 2.5.

$$CH_{4,(g)} + CO_{2,(g)} \rightarrow 2CO_{(g)} + 2H_{2,(g)} \tag{2.3}$$

$$CH_{4,(g)} + H_2O_{(g)} \rightarrow CO_{(g)} + 3H_{2,(g)} \tag{2.4}$$

$$H_2O_{(g)} + CO_{(g)} \rightarrow CO_{2,(g)} + H_{2,(g)} \tag{2.5}$$
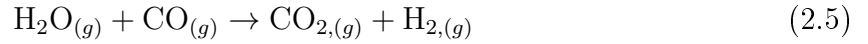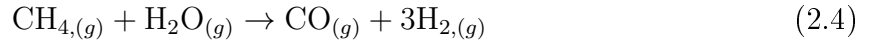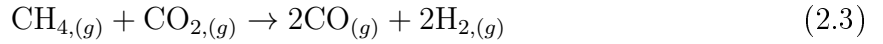
In the technological device several cells are connected in series to add the voltage developed by each cell and increase the total power output. The cells exist in two main geometries, planar and tubular. In the planar case, on which this thesis is centered, the cells are separated by metallic plates called metallic inter-connect (MIC) that guarantee the physical separation between the two neighboring compartments but also conduct the current along the stack and are designed for permitting the gas distribution on the electrode surface.

2.1.2 Degradation mechanisms

A number of degradation pathways occurring during SOFC operation have been identified and are briefly described below. The present work focuses on microstructural changes, poisoning by Cr and reaction between LSM and YSZ; it is worthwhile mentioning that

microstructural changes may affect both cathode and anode, while Cr poisoning and zirconate formation are responsible only for loss of cathode performance.

Microstructural changes

As mentioned earlier, high temperature favors SOFC operation, since both the electronic and ionic conductivity of the materials increase exponentially with temperature [10] and so does the catalytic activity of the electrodes. However, high temperature operation also causes microstructural changes like densification and particle coarsening. This phenomenon is particularly evident in the anode because of the sintering of Ni particles [11, 12, 13], causing loss of Ni-Ni contacts, decrease of Ni surface and TPB to catalyze the hydrogen oxidation and change in porosity. Several authors in literature report a cell performance loss related to a degradation of the anode microstructure [14, 15], typically with an investigation based on electrochemical impedance spectroscopy that allows relating the increase in cell resistance to the degradation of one or more anode processes (decrease of conductivity and/or of catalytic activity).

The morphological change happens mainly as a redistribution of material inside the electrode and has as a driving force the tendency to reduce free surface energy. On the one hand, typical temperatures for SOFC operation are relatively close to its melting point (~1450°C) and therefore the mobility of Ni atoms is high, allowing diffusion mechanisms. On the other hand, the presence of water vapor favors the evaporation/condensation of Ni species through the formation of hydroxides [16]. Both paths lead to a formation of bigger particles in average, with the consequent decrease of TPB, and possible loss of contacts.

Ni evaporation can also cause a net material loss [16]; this case differs from the evaporation/condensation process in the sense that part of the Ni abandons the system with the exiting flow, instead of being displaced from one to another location inside the electrode.

Morphological variation has also been observed at high temperatures (900–1000 °C) for typical cathode materials such as LSM, especially in the case of A-site deficient compositions [17]; in this case, the phenomenon is less dramatic because of the better stability and interfacial compatibility between the ceramics of the composite. However, the search for

increase of electrochemical performances leads to the utilization of finer microstructures, with the extreme case of the introduction of nanoparticles in the porosity to increase the number of active sites ([18] and references therein). In this context, morphological variation increases in importance as a degradation phenomenon for the cathode.

Poisoning by chromium

As already reported above, in state-of-the-art SOFC stacks, cells are electrically connected by MIC plates which also ensure gas separation between the anode compartment of one cell and the cathode compartment of the next [19]. MICs are usually made of heat-resistant steels containing chromium, so that the Cr-rich oxide scale formed on the surface in oxidizing conditions protects the metallic material underneath. Balance-of-plant (BoP) components like tubing, heat exchangers etc. are often made of similar materials, and may also form chromia scales. Under SOFC operating conditions, such Cr-rich layers exposed to air flow release volatile Cr(VI) species like CrO_3 and, if water vapor is present, $CrO_2(OH)_2$ [20] that diffuse inside the porosity of the composite electrode.

In literature, those species are reported to poison SOFC cathodes by deposition of Cr(III) species like Cr_2O_3 or Cr,Mn oxides [21, 22]. A correlation between presence of Cr and degradation of cell performance is well known; small amounts of Cr, even as low as fractions of atomic percent, can cause severe increase of the total electrode overpotential [21, 23, 24]. However, a deep understanding of the mechanism through which Cr species are transported to the electrochemical active sites and (totally or partially) block them is not reached yet. Recent studies admit that it was not possible to find a close correlation between the amount of Cr deposed measured during post-mortem analysis and the degradation rate during operation [25, 26]. Moreover, although there is some agreement on the fact that Cr deposition occurs preferentially at the electrode/electrolyte interface [23, 27, 28], some studies in literature report presence of Cr distributed in the electrode or even in the current collection layer (CCL) [29, 28, 30, 31] - which cannot have significant electrochemical activity.

In our opinion, this disagreement and the difficulty of finding a quantitative correlation

between deposited Cr and measured performance loss has part of its origin in the fact that the quantification of a small amount of Cr in a LSM-containing material is challenging: indeed, there is overlapping between Cr X-ray emission lines with those of La, O and Mn spectra, which are abundant in the layer so that classic scanning electron microscopy with energy-dispersive X-ray microanalysis (SEM-EDX) can be affected by a significant error at low Cr concentrations.

In any case, in literature two main mechanisms are proposed for Cr deposition. The first one is the direct electrochemical reaction of the volatile Cr(VI) species to solid Cr(III) species blocking the active sites, according to the following reactions [21, 23, 32]:

$$CrO_{3(g)} + 3e^- \rightarrow \frac{1}{2}Cr_2O_{3(s)} + \frac{3}{2}O^{2-} \tag{2.6}$$

$$CrO_2(OH)_{2(g)} + 3e^- \rightarrow \frac{1}{2}Cr_2O_{3(s)} + H_2O_{(g)} + \frac{3}{2}O^{2-} \tag{2.7}$$
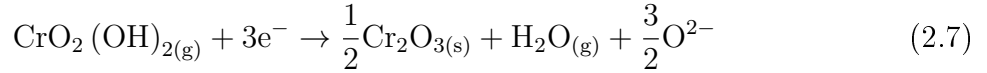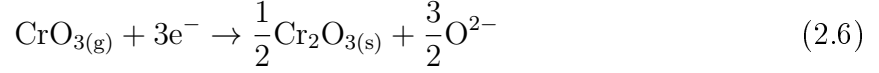
This mechanism is based on the fact that it is thermodynamically favored by a negative $\Delta_r G$ of the reactions [32] and implies that the electrochemically-driven deposition, happening in parallel to the oxygen reduction, is localized on the cathodic active sites.

The second mechanism, proposed in the form of unbalanced reactions by Jiang et al. [33], assumes the formation of a Cr-Mn intermediate and is therefore chemical and not necessarily localized to the TPB sites:

$$Mn^{2+} + CrO_{3(g)} \rightarrow Cr - Mn - O_{(nucleus)} \tag{2.8}$$

$$Cr - Mn - O_{(nucleus)} + CrO_{3(g)} \rightarrow Cr_2O_{3(s)} \tag{2.9}$$
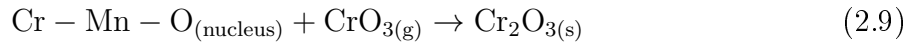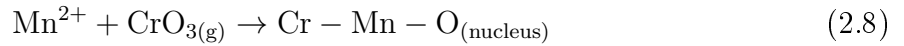
The possible formation of a Cr-Mn spinel is also included:

$$Cr_2O_{3(s)} + CrO_{3(g)} + Mn^{2+} \rightarrow (Cr, Mn)_3 O_{4(s)} \tag{2.10}$$
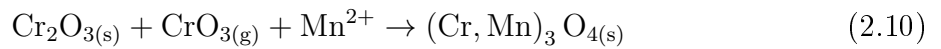
However, the indirect effect of the cathode polarization of LSM electrodes, causing the reduction of Mn with higher oxidation states (Mn^{3+} and Mn^{4+}) to Mn^{2+}, creates the nucleation sites for the deposition of the Cr oxide especially near to the active sites.

Reactions between LSM and electrolyte

The reactivity of Zirconium oxide towards La and Sr can lead to the formation of non-conducting phases like $La_2Zr_2O_7$ or $SrZrO_3$ at the interface between LSM and YSZ, deteriorating the catalytic activity of the cathode. The performance loss is due to increased diffusion paths, the blocking of reaction sites on LSM, or the blocking of sites for the integration of O^{2-} in the YSZ lattice [34].

The presence of those phases has been detected experimentally through microscopic observation [35, 36] and thermodynamically modeled with multi-component phase diagrams [34, 37, 38, 39]. Generally the multiphase modelling begins with the binary diagrams and proceeds combining them to ternary and quaternary diagrams.

There are several parameters that influences the formation of zirconates: the composition of LSM, and in particular the amount of Sr, is a key parameter to limit the tendency towards the formation of unwanted phases [40, 41] and a Sr content of about 30% appears to be optimal against the formation of unwanted phases. Furthermore, non-stoichiometric manganites with A-site deficiency and the general formula $A_{1-x}MnO_{3\pm\delta}$ have been proved to be more stable and to form zirconates to a lesser extent or only after larger operation times [34, 37, 39]. Finally, the sintering and operation conditions play an important role: high sintering temperatures favor the formation of $La_2Zr_2O_7$ at the interface [35, 36] but their decomposition has been observed during cathodic polarization [35, 42]. Other authors reported that zirconate are formed at high cathodic overpotentials [43, 15] and at low oxygen partial pressure [44]. In conclusion, observations are contradictory or, at least, show an apparent lack of consistency.

In summary, the LSM-YSZ system shows a complex behavior because it is dominated by two main and contrasting phenomena, giving rise to a number of different situations.

Firstly, the formation of $La_2Zr_2O_7$ is an *oxidative* process, causing the increase of the average valence state of the Mn in the perovskite with the following reaction:

$$LaMnO_3 + x\, ZrO_2 + 0.75x\, O_{2(g)} \rightleftharpoons 0.5x\, La_2Zr_2O_7 + La_{1-x}MnO_3 \qquad (2.11)$$
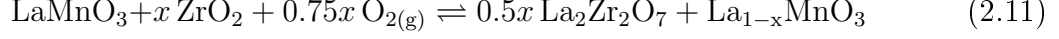
Mn is present in LSM with several valencies (Mn^{2+}, Mn^{3+}, Mn^{4+}) due to the dismutation of Mn^{3+} to Mn^{2+} and Mn^{4+} [45]; the relative amount determines the average valence. The A-site deficiency influences the average valence of Mn; in Eq 2.11, for instance, it passes from 3 to $3(1+x)$ [37]. The depletion of cations in the A-site means that the composition of the perovskite becomes $La_{1-x}MnO_3$; this increases the average valence of Mn and hinders the zirconate formation while displacing the equilibrium of Eq. 2.11 towards the left. A similar effect is achieved with the introduction of Sr instead of La (which is the case of commonly used LSM), at least until the formation of $SrZrO_3$ becomes dominant. The fact that the formation of $La_2Zr_2O_7$ is oxidative for Mn as shown in Eq. 2.11 explains the observed stability related to the A-site deficiency and the introduction of Sr. In effect, the dissolution during operation of the $La_2Zr_2O_7$ grains can be also explained with the fact that the zirconates formed at high temperature and in oxidizing conditions during sintering, are eventually dissolved due to the reducing environment induced by the cathodic polarization.

The second phenomenon is the possibility of Mn dissolution inside YSZ; Kawada et al. [46] showed that the amount of Mn dissolved inside YSZ can be important, to reach a few molar percent. The dissolution happens according to the following reaction [34]:

$$MnO_{n(LSM)} \overset{YSZ}{\rightleftharpoons} MnO_{n'(YSZ)} + \frac{(n-n')}{2}\, O_{2(g)} \qquad (2.12)$$
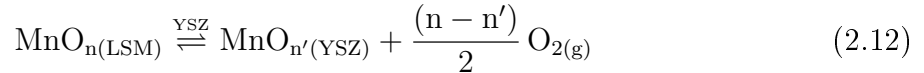
The Mn is dissolved inside the YSZ as Mn^{2+} [45] and therefore Eq. 2.12 represents a *reductive* reaction. So, reductive conditions as high cathode overpotentials and low oxygen partial pressures are not directly promoting Eq. 2.11, but favor the progressive dissolution of Mn into YSZ and the depletion of LSM at the interface. The process can continue only

until a certain limit, after which the LSM is destabilized by increase of the activity of $La_2O_{3(LSM)}$, leading to the formation of zirconates.

In state-of-the-art material cells, the stoichiometry of LSM is optimized with respect to A-site deficiency and Sr content to be as inert as possible towards YSZ. In addition, operating conditions are carefully controlled in order to avoid high overpotential or low oxygen partial pressure. However, a localized high temperature (hot-spot) or a localized degradation (causing a correspondingly localized high cathode overpotential) can induce the formation of zirconates [47].

Crack formation in the electrolyte

The introduction of oxygen in the anode compartment due to leakages or mishandled on/off cycles can lead to the re-oxidation of the anode support. As there is a considerable difference in the molar volume of Ni and its oxides, the expansion of the oxidized Ni particles may lead to the formation of internal stresses. In an anode-supported design, these internal stresses bring the thin electrolyte under tension with the consequent formation of cracks [48, 49, 50]. The permeation of gases through the electrolyte causes an obvious loss in performance and an accelerated local degradation because of a change in composition and the formation of a hot spot.

Carburisation on nickel particles

At high temperature, Ni anode supports show sufficient cracking and reforming activity to allow for the use of different fuels. During internal reforming, hydrocarbons or alcohols are converted along with the formation of water during the anode reaction, in ready-to-react gases such as H_2 and CO. During this process, there is the possibility of carbon deposition on the catalyst, thereby poisoning it and decreasing both its reforming and electrochemical activity, and eventually hindering gas diffusion through the support [51, 52].

Formation of nickel sulphide

When using untreated hydrocarbon fuels, the presence of sulfur-containing compounds may lead to the formation of Ni sulphide, with consequent degradation of the activity in the anode catalyst [53, 54].

Loss of conductivity of the electrolyte

A phase change of the electrolyte or the segregation of impurities or dopants can decrease the ionic conductivity [55, 56, 57].

2.2   Percolation theory

In order to accurately describe an electrode, its functioning and the possible variations with time, it is necessary to do so in a way that grasps the influence of the constituting elements on the electrochemical reaction; this is defined "micro-modelling" and can have a variety of forms. Generally speaking, we may divide roughly the micro-models into pore models [58, 59], random resistor network models [60, 61, 62], and random packing sphere models [63, 64, 65]. In the last case, percolation theory [66, 67] can be applied to calculate the physical parameters that characterize the system.

In our opinion, micro-modelling based on percolation theory is particularly attractive because, while being relatively simple in form, it can reach a high level of accuracy. In the next section, the basic elements of percolation theory and its state-of-the-art applications in the SOFC field are described.

Introduction

Many processes in Nature are based on disordered systems, and some of them are of high scientific interest. The gelification of a polymeric system through the interconnection of branched monomers, the propagation of a fire in a forest or the spreading of a plague in a crowded city are examples that give an idea of how broad range of important phenomena

can happen in *disordered structures.* Disordered structures are so far from the possibility of deterministic description that they can be considered *random:* the morphology of the system is so complex that, from our point of view, it has an apparent randomness.

The description of a morphology characterized by randomness, too complex for a deterministic approach, requires the use of statistics. The aim of statistical physics is to provide methods to derive macroscopic properties of a system from laws governing the microscopic, random constitutive elements or, inversely, to deduce microscopic properties from macroscopic information observed experimentally.

Percolation theory is a statistical physics tool taking into account not only the *geometry* of a disordered system, i. e. size and shape of the constituting elements, but also the *topology*, that means the interconnectiveness of these individual microscopic elements. Flory [68] developed percolation theory for the first time in 1941 for describing gelification during the polymerization of branching molecules, leading to the formation of very large macromolecules and a dramatic increase of the viscosity.

In order to introduce the concept of percolation, an example can be useful. Let us imagine a forest, in which trees separated by less than a certain distance (10 meters, for instance) are considered neighboring. A fire starting at one end of the forest can propagate through neighboring trees, but it will be blocked in a dead end if it touches a tree that has, as only neighbors, the tree(s) already on fire. Obviously, as an extreme case, a forest formed only by sparse trees with no neighbors will be fire-safe (and it would be a quite sad forest). In order to prevent the spreading of the fire in a dense forest without having to eradicate the vast majority of the trees, it would be possible to eradicate only some trees so that, statistically speaking, there is no path from one end of the forest to the other. Starting from such a dense forest and eliminating progressively trees in random positions, there will be a specific moment in which we attain the probability of no traversing path. This will happen long before the forest has only isolated trees, when clusters of neighboring trees still exist but are *macroscopically* disconnected. This point marks a transition from a system that is macroscopically open (to fire, in the specific case) to one that is macroscopically close, and is called *percolation threshold.* If we idealize the

forest of the example, we can divide it with a mesh and occupy each site with a tree with a certain probability o, or have it vacant with probability $1-o$. The percolation threshold is defined as the largest p below which there is no traversing cluster of occupied sites through the sample. Figure 2.2 shows a schematic representation of the forest, above and below the percolation threshold.

A last important remark is that, when the first spanning cluster is formed at the percolation threshold, there is some part of the occupied sites that do not belong to it and are therefore "inactive". This concept is important because it means that the efficiency of transport can be improved while increasing the occupation of sites above the percolation threshold, increasing the fraction of active sites that belong to a spanning cluster.

Effective properties of a random sphere packing of binary powders

Percolation theory can be applied with very satisfactory results to electrical systems, permitting to calculate properties like the effective conductivity of a network of conducting particles in a mixture with non-conductive particles. The case of composite LSM/YSZ electrodes is of particular interest since LSM is an electronic conductor and YSZ an ionic conductor so that each particle must be considered non-conductive for the transport characteristic of the other phase. Therefore there are simultaneously two entangled and competing percolating networks that must guarantee both transports; they are competing because the increase of occupation of one phase has a positive effect on its connectivity but automatically has the opposite effect on the second solid phase.

For a composite electrode made of an electronic and a ionic conductor, the evidence of a relatively sharp transition between the regions with only one phase spanning through the sample and the central region in which both phases are percolating has been given by Nairn et al. [69] both from an experimental and computational point of view. In a successive study [70], by computer simulation they showed that percolation theory predicts well the behavior of electrodes with thickness much bigger than the constituting particles. In the case of a thin electrode, a smooth transition happens near the expected percolation
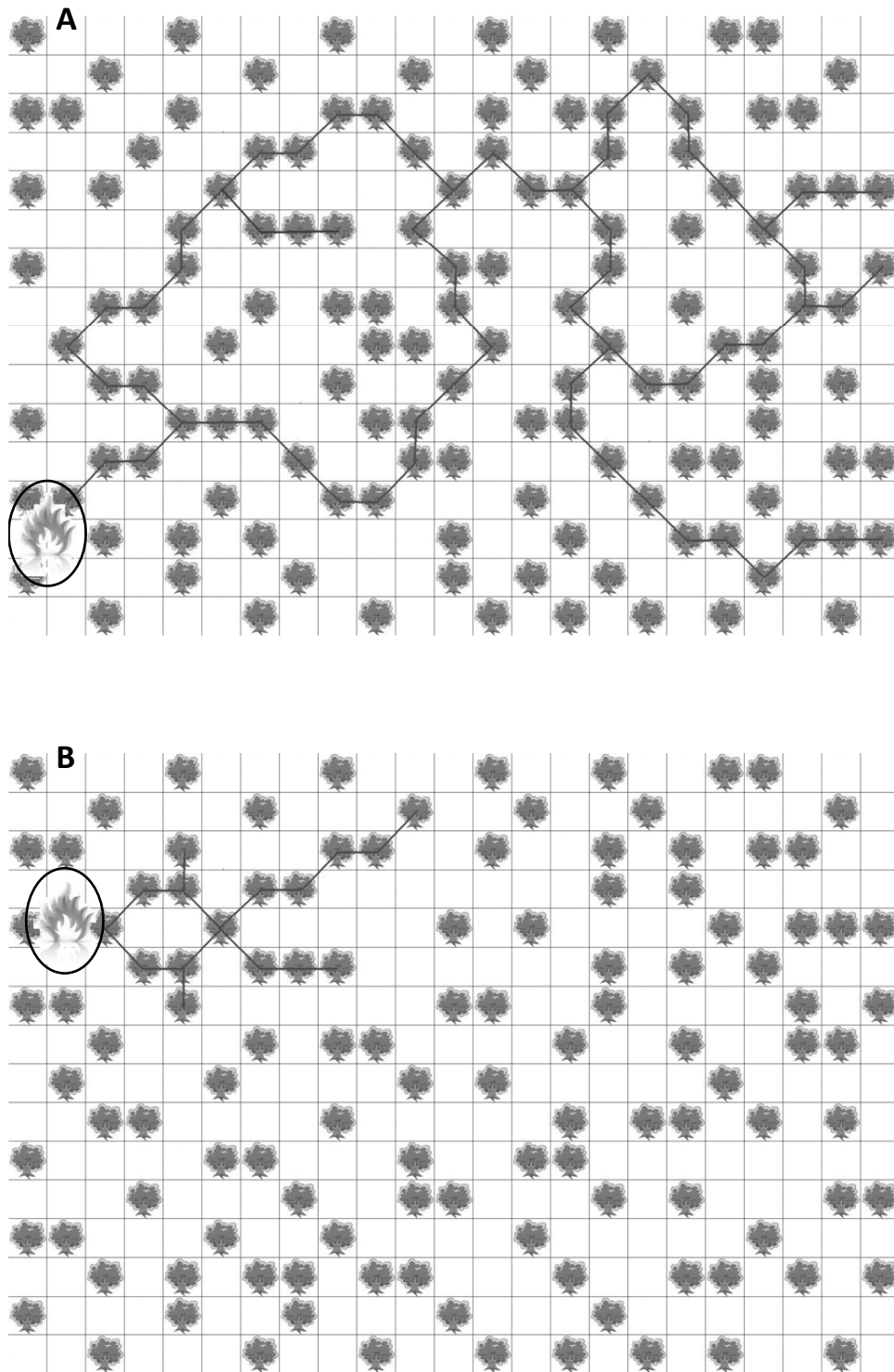
Figure 2.2. The "forest-on-fire" example of percolation. A) a spanning cluster of occupied sites permits the propagation of the fire through the whole system. B) Isolated clusters exist, but the system is macroscopically disconnected and cannot be traversed by the fire

threshold instead of an abrupt cut-off.

Composite electrodes like LSM/YSZ cathodes or Ni/YSZ anodes are binary powder mixtures. In materials science, binary powder mixtures have been studied because of the relevance of processing and properties of composite materials. In effect, the connectivity of ceramic, non-deformable inclusions in a metallic powder material has impact on the plastic consolidation of the composite as a whole [71]. The results obtained indicate that the network of ceramic particles supports an increasing fraction of the applied pressure after a certain volume fraction occupied by the inclusions ($\sim$0.2), implying the necessity of a higher applied pressure for consolidating the densification of the composite.

Bouvard et al. [72] proposed a model based on physically meaningful equations that is based on the particle coordination number in a random packing of spheres. The generic coordination number Z, i.e. the average number of contacts of each particle (without distinction of phase) with its neighbors. In a model represented as a mixture composed by a random sphere packing of matrix particles with inclusions of a different phase, it is possible to calculate the coordination number of either the m (matrix) or i (inclusion) particles as follows:

$$Z_m = 3 + \frac{(Z-3)\,P^2}{n_i + (1-n_i)P^2} \tag{2.13}$$

$$Z_i = 3 + \frac{Z-3}{n_i + (1-n_i)P^2} \tag{2.14}$$

where the average coordination number Z is 6 for random sphere packing [73], P is the ratio between the particle radius of the two phases $P = \frac{r_m}{r_i}$, and n_i is the fraction *in number* of the inclusion particles. n_i is related to the composition of the mixture and the particle dimensions, and can by calculated as (derived from [72]):

$$n_i = \frac{\varphi_i P^3}{\varphi_i P^3 - \varphi_i + 1} \tag{2.15}$$

φ_i is the inclusion volume fraction of the solid volume (voids excluded); obviously $\varphi_m = 1 - \varphi_i$.
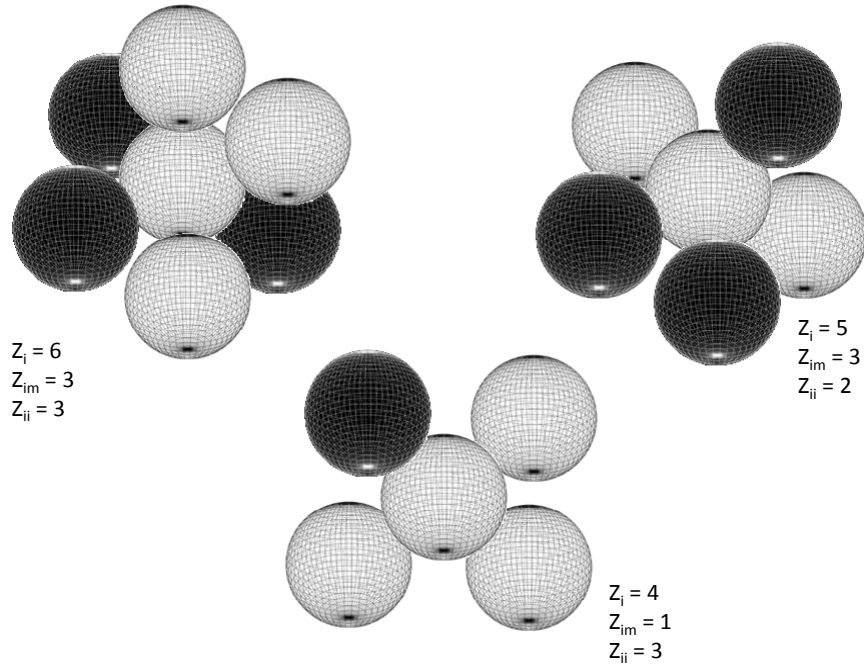
Figure 2.3. Particle coordination numbers. For three different packings, the coordination number of an inclusion particle is illustrated, along with the two values Z_{im} and Z_{ii}, representing the number of contacts between the central particle and the surrounding particles of each phase. In a statistical significant system, all these three values represent an average and can therefore be non-integer values.

Bouvard calculated the number of contacts between inclusion particles and matrix particles as:

$$Z_{im} = (1 - n_i) \frac{Z_i Z_m}{Z} \tag{2.16}$$

The percolation of the inclusion phase is obtained when the average number of contacts between inclusion particles reaches $Z_{ii} = 2$; obviously $Z_{ii} = Z_i - Z_{im}$. In the same way it is possible to calculate the percolation threshold of the matrix particles, in the case of inclusion particles becoming the majority. Figure 2.3 illustrates different scenarios, with Z_i, Z_{im} and Z_{ii} specified.

In both cases the minimal volume fraction φ of a percolating phase is $\varphi = 0.33$ in the

case of spheres of the same diameter, i.e. $P = 1$. The authors validated their model by numerical simulation, and they found that the overall porosity ε is expected to be around 40%.

This value of φ found with this model is near to the experimental results reported by a number of authors [74, 75, 76] although other authors [77, 78] showed that the percolation threshold can be at much lower value of φ and/or characterized by a smooth transition when the microstructure cannot be assimilated to a packing of spheres as a consequence of a preparation method different from the classic sintering of binary powders.

On the other hand, the model proposed by Suzuki et al. [79] has been shown to be in better agreement with experimental results predicting the percolation threshold, in particular if P is different from 1 [80]; according to Suzuki's model,

$$Z_{ii} = \frac{Z\, n_i}{[n_i + (1 - n_i)\, P^2]} \tag{2.17}$$

and $Z_{ii} = 1.764$ (instead of the value of 2 assumed by Bouvard) corresponds to the percolation threshold. Using Eq. 2.17, the volume fraction needed for percolation is $\varphi = 0.294$ in the case of spheres of the same diameter, i.e. $P = 1$.

Other important results that can be obtained with percolation theory based on the coordination number of particles: the probability that a single particle belongs to a cluster spanning through the whole electrode is:

$$p_i = \left(1 - \left(\frac{4 - Z_{ii}}{2} \right)^{2.5} \right)^{0.4} \tag{2.18}$$

This is a very important value, because it permits to calculate if a single contact is made between two particles, each belonging to a percolating cluster.

Electrode models based on percolation theory in SOFC

Juhl et al. in 1996 [81] pointed out that not only the geometry, but also the topology and the interconnectiveness of LSM and YSZ particles is important to determinate the performance of a SOFC cathode. They based their observation on electrochemical results

obtained with cathodes of different composition; they concluded that a large potential was present for performance improvement through control of the microstructure and thickness.

Costamagna et al. [63] proposed in 1998 a detailed electrochemical model for composite electrodes based on elements of the theory developed by Bouvard and Lange [72, 71] and Suzuki [79]. They adopted Bouvard's coordination theory for calculating the average number of contacts between particles of the same phase or of different phases and the deriving probabilities (Eq. 2.13-2.16 and 2.18), but they used Suzuki's model to predict more accurately the percolation thresholds (Eq. 2.17). Starting from Eq. 2.13-2.18 they estimated some important macroscopic properties such as the TPB lenght, the effective resistivities of the two percolating networks and the specific active area for the electrochemical reaction; these macroscopic parameters have been used for feeding a one-dimension electrochemical model with a distributed Butler-Volmer reaction distributed along the electrode thickness. This model is described more deeply in the following section.

In effect, the calculation of the resistivity of a mixed conducting-non conducting medium is a problem classically treated in percolation theory; according to [66], the conductivity of a packing of conducting and insulating particles above the percolation threshold is:

$$\frac{1}{\rho} = \sigma \propto (n - n_c)^{\mu} \tag{2.19}$$

where n_c is the critical number fraction at the percolation threshold, and μ is a universal parameter that in three dimensions is 2.

A similar way has been used by Dusastre et al. [82], comparing the resistivity of a lanthanum-strontium cobaltite-ferrite cathode on a gadolina-doped ceria electrolyte support (LSCF/CGO) from simulations and experimental results. The agreement was acceptable between simulations and experimental results, with a good qualitative correspondence of the resistivity as a function of the composition and some discrepancy between the expected percolation threshold and the observed one. In any case, their treatment focused on the conductivity as an indicator for predicting the best performance, but lacked a

geometrical treatment for predicting the active area for the electrochemical reaction.

A last example of the application of percolation theory in SOFC has been proposed more recently by Deseure et al. [83] and Schneider et al. [84] from the University of Grenoble. A numerically generated electrode has been studied by a discrete element method (DEM) with a non-uniform distribution of phases along the thickness, defined functionally-graded (FG) electrodes; the performance of the electrode has been simulated idealizing the binary mixture as a resistance network. The conclusion reached is that a FG electrode does not work significantly better than a well-percolating homogeneous electrode, since in the regions with low content of one of the two phases the isolated clusters act as dead material. On the other hand, a FG that guarantees percolation of both phases in every point of the electrode improves percolation and can give some advantage.

It is worth mentioning some limitations of percolation models applied to composite electrodes:

- the particles are not spherical in reality, but they are considered such in the model. This can lead to irregular contact areas, that are modelled as circular shapes, and to differences between the real and predicted values.

- there might be wetting effects, causing packing not to be random. This has been demonstrated to be the case for Ni/CGO anodes [85].

Costamagna's percolation model for composite electrodes

Costamagna's model has been chosen as a suitable one in order to simulate the performance of composite cathodes and introduce degradation phenomena. The geometrical approach guarantees the possibility to extract meaningful parameters such as the active area for the electrochemical reaction and the effective resistivities of the percolating networks, which can be used for an extension of the model for including degradation. In this section the model is presented in a complete way, since it is the basis for the degradation model elaborated in this thesis.

One of the most interesting features of the model is the electrochemically active surface area per unit volume A. It is calculated taking into account that an active site must be a point of contact per unit volume between particles of different phases which, according to Eq. 2.13-2.16 is equal to $n_i Z_{im}$. Obviously these interfaces are not always electrochemically active, since it is required that both particles belong to the corresponding percolating network for the transport of electrons and ions. This happens with a probability equal to the composite probability $p_i\, p_m$. From geometrical considerations, Costamagna and co-authors arrive at an equation permitting to calculate the active area per unit volume A:

$$A = \pi \sin^2 \theta \, r_i^2 n^* n_i n_m \frac{Z_i Z_m}{Z} p_i p_m \tag{2.20}$$

θ is the angle of interpenetration of the two particles, determining the extension of the interfacial area, as shown in Figure 2.4. n^* is the number of particles (of both phases) per unit volume, given by:

$$n^* = \frac{i - \varepsilon}{\frac{4}{3}\pi r_i^3 \left[n_i + (1 - n_i) P^3\right]} \tag{2.21}$$

Costamagna et al. use the work from Bouvard for calculating p and Z_{im} (and therefore for calculating A from Eq. 2.20) and Suzuki's model for calculating the percolation thresholds. Suzuki's theory is not suitable for calculating A since, although predicting better the percolation thresholds, it does not satisfy the requirement that $n_i Z_{im} = (1 - n_i) Z_{mi}$.

A second point is the estimation of the effective conductivity of a percolating network, taking into account the necking and current restriction in the contact between two particles of the same phase. This is done modifying Eq. 2.19 as follows:

$$\frac{1}{\rho_{eff}} = \sigma_{eff} = \gamma \sigma_0 \frac{(n - n_c)^\mu}{(1 - n_c)^\mu} \tag{2.22}$$

so that when $n = 1$, $\sigma_{eff} = \gamma \sigma_0$, with γ taking in account the additional resistance given by the necking.
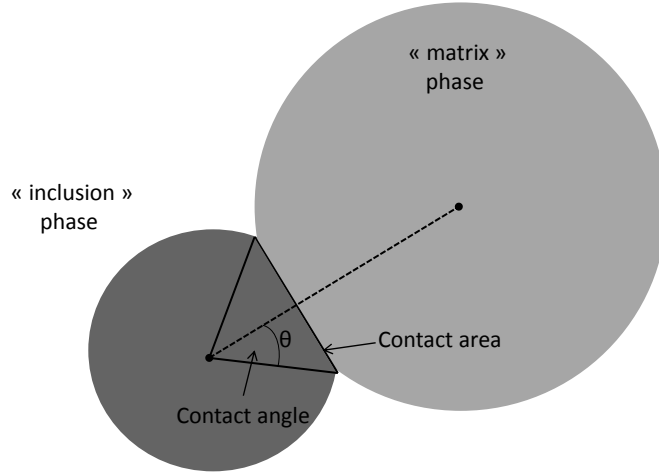
Figure 2.4. Contact angle between two intersecting spheres for calculating the active area for the oxygen reduction reaction in Costamagna's model. The angle is taken with respect to the inclusion particle, considered by default the smallest.

Once obtained σ_{eff} and A, an electrochemical model is put in place under the following assumptions:

1. Steady state conditions

2. Temperature and pressure uniform through-out the electrode

3. One-dimensional model along the electrode thickness

4. Homogeneous σ_{eff} and A in the whole electrode

On the basis of Ohm's law and charge conservation equations, it is assumed that:

$$\begin{cases} \nabla V_{io} = -\rho_{io}^{eff} i_{io} \\[2mm] \nabla V_{el} = -\rho_{el}^{eff} i_{el} \\[2mm] \text{div}\,(i_{io}) = -\text{div}\,(i_{el}) = A\,i_n \end{cases} \tag{2.23}$$

Assuming for simplicity a one-step, single electron transfer process for the electrochemical reaction, the related kinetics is given by a Butler-Volmer equation with the following form:

$$i_n = i_0 \left\{ \frac{C_r}{C_r^*} e^{\left(\beta \frac{\eta F}{RT}\right)} - \frac{C_p}{C_p^*} e^{\left[-(1-\beta)\frac{\eta F}{RT}\right]} \right\} \tag{2.24}$$

i_0 is the exchange current density for the electrochemical reaction, C is the surface concentration of the reactant or product, C^* is the bulk concentration, β the symmetry factor and η the local overpotential. η is defined as the local displacement from equilibrium at one specific distance x from the electrode/electrolyte interface:

$$\eta_{(x)} = (V_{io}^{eq} - V_{el}^{eq}) - (V_{io(x)} - V_{el(x)}) \tag{2.25}$$

as opposed to the overall electrode overpotential η_0, defined as:

$$\eta_0 = (V_{io}^{eq} - V_{el}^{eq}) - (V_{io}|_{x=a} - V_{el}|_{x=0}) \tag{2.26}$$

where a is the electrode thickness. Eq. 2.24 can be simplified assuming a constant gas composition along the electrode. Indeed, it is possible to evaluate the Thiele modulus defined as $\Phi = \sqrt{t_{diffusion}/t_{reaction}} = a\sqrt{k/D_{eff}}$ assuming that k, considered constant as an approximation, can be estimated as: $k \approx \frac{I_{tot}}{n_{e^-} FC^0 a}$. Assuming $I_{tot} \approx 0.5$ A/m^2, $n_{e^-} = 4$ (number of electrons exchanged per molecule), $a \approx 50$ μm$\approx 5 \cdot 10^{-5}$ m, $C^0 \approx 2$ mol/m^3 and $D_{eff} \approx 10^{-5}$ m^2/s, we obtain $\Phi \approx 0.18$; diffusion is considered much faster than the reaction when $\Phi \leq 0.3$ (or $\Phi^2 \leq 0.1$), which is the case. We can therefore consider a constant concentration of reactive species and no impact of the diffusion on the performance of the cathode.

Moreover, Eq. 2.24 is simplified assuming a linear behavior and $\beta = 1/2$, leading to:

$$i_n = i_0 \frac{\eta F}{RT} \tag{2.27}$$

The preceding equations allows arriving at the following system:

$$
\begin{cases}
\frac{\mathrm{d}V_{io}}{\mathrm{d}x} = -\rho_{io}^{eff} i_{io} \\[2mm]
\frac{\mathrm{d}V_{el}}{\mathrm{d}x} = -\rho_{el}^{eff} i_{el} \\[2mm]
\eta = (V_{io}^{eq} - V_{el}^{eq}) - (V_{io} - V_{el}) \\[2mm]
\frac{\mathrm{d}^2\eta}{\mathrm{d}x^2} = i_0 \frac{AF\left(\rho_{el}^{eff} + \rho_{io}^{eff}\right)}{RT} \eta \\[2mm]
\hline
x = 0 \quad i_{io} = 0 \quad i_{el} = I_{tot} \\[2mm]
x = a \quad i_{io} = I_{tot} \quad i_{el} = 0
\end{cases}
\tag{2.28}
$$

where a is the electrode thickness and I_{tot} the total current density passing through the cell. The simplifications adopted permit to reach an analytical solution:

$$\eta_{(x)} = \frac{I_{tot}a}{\Gamma \sinh(\Gamma)} \left\{ \rho_{io}^{eff} \cosh\left(\Gamma\frac{x}{a}\right) + \rho_{el}^{eff} \cosh\left[\Gamma\left(1 - \frac{x}{a}\right)\right] \right\} \tag{2.29}$$

Γ is a parameter similar to Thiele modulus, defined as:

$$\Gamma = \sqrt{\frac{i_0 AF(\rho_{io}^{eff} + \rho_{el}^{eff})a^2}{RT}} \tag{2.30}$$

The physical meaning of Γ is the square root of the ratio between the combined ohmic resistivity of the electrode ($\rho_{io}^{eff} + \rho_{el}^{eff}$) and the resistivity of the electrochemical reaction. The difference with the Thiele modulus resides in the fact that in a composite electrode the transport is binary in the two conducting phases. Using the analytical solution it is possible to describe the way in which the reaction happens along a cathode thickness, converting progressively the electronic current into an ionic current, and vice versa in an anode; an example is brought by Figure 2.5.

The performance of the electrode is estimated as the reciprocal area specific resistance (ASR) of the electrode, i. e. the ratio between the total current density I_{tot} and the overall electrode overpotential η_0. η_0 can be obtained through integration of the system:
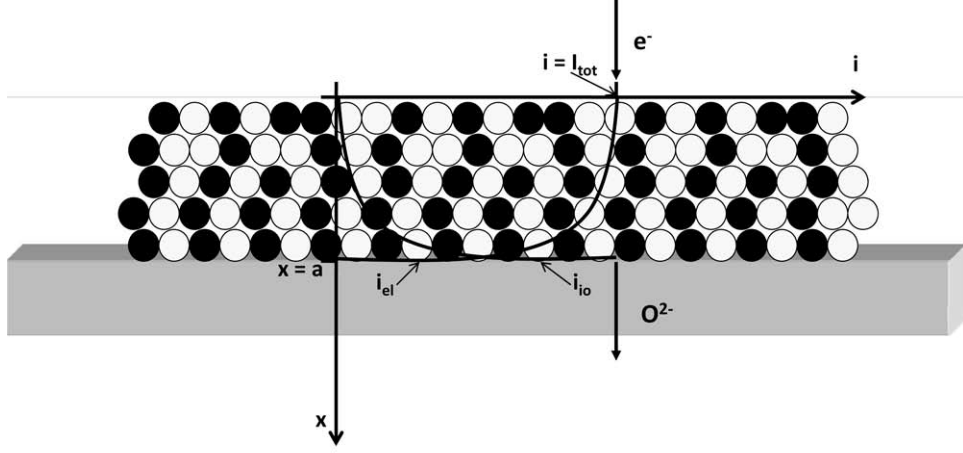
Figure 2.5. Progressive conversion of the electronic current to ionic current induced by the electrochemical reaction of the cathode. The reaction takes place progressively along the thickness, in particular near the interface with the electrolyte due to the lower conductivity of the YSZ percolating network.

$$\eta_0 = \frac{a(\rho_{io}^{eff} + \rho_{el}^{eff})I_{tot}}{\Gamma \sinh(\Gamma)} \left\{ \cosh(\Gamma) + \frac{\rho_{io}^{eff}\rho_{el}^{eff}}{(\rho_{io}^{eff} + \rho_{el}^{eff})^2} \left[2 + \Gamma \sinh(\Gamma) - 2\cosh(\Gamma) \right] \right\} \quad (2.31)$$

Therefore the performance of the electrode is:

$$\frac{1}{ASR_{electrode}} = \frac{I_{tot}}{\eta_0} = \frac{\Gamma \sinh(\Gamma)}{a(\rho_{io}^{eff} + \rho_{el}^{eff}) \left\{ \cosh(\Gamma) + \frac{\rho_{io}^{eff}\rho_{el}^{eff}}{(\rho_{io}^{eff} + \rho_{el}^{eff})^2} \left[2 + \Gamma \sinh(\Gamma) - 2\cosh(\Gamma) \right] \right\}}$$
$$(2.32)$$

The parametric study performed by the authors with the model permitted to reach a very interesting conclusion: the optimal performance is not always reached at the electrode composition guaranteeing the highest value of A. In effect, a trade-off can be reached between the number of active sites available and the efficiency of current transport in the two percolating networks. For instance, SOFC anode composites are characterized by a large difference in conductivity between Ni and YSZ and, at the same time, by a very efficient electrochemical reaction; in such conditions, the conduction in YSZ is by far the limiting factor for the electrode performance. If $P \simeq 1$, the highest A is obtained

at roughly 50% v/v (i.e. the composition that statistically provides the highest number of contact per unit volume between Ni and YSZ, and the highest combined probability $p_i p_m$), but the optimal performance is found at around 35% v/v of Ni, which is close to the minimal amount needed for having the percolation in the Ni phase.

The situation is less extreme for LSM/YSZ composite cathodes, because of a smaller difference in conductivity between the two phases. Moreover, the electrochemical reaction is less efficient for this system, so that A has more relative importance. In any case, it was found that, if the microstructure is fine enough to provide abundant A, then an enrichment in YSZ can be beneficial for the electrode performance.

2.3 Electrochemical impedance spectroscopy (EIS)

Introduction

Electrochemical impedance spectroscopy (EIS) is one of the most common and powerful techniques for the characterization of electrochemical systems, and it is widely used to investigate SOFC materials and assemblies.

EIS measures the impedance of the investigated electrochemical system over a wide range of frequencies. In effect, electrochemical processes can be considered like elements of an equivalent circuit, with associated resistances, capacitances etc. Such complex circuits have a complex behavior and have to be characterized through the measurement of the impedance, which is a physical property extending the concept of resistance. The impedance, like the resistance, is a measure of the ability of the circuit to resist the flow of electrical current; however, it is a property affected by the frequency of an AC signal so, unlike the resistance, takes into account the time parameter.

When an AC sinusoidal signal is applied to the system, the response, either a potential difference in galvanostatic mode or a current in potentiostatic mode, is obtained and measured. When the excitation is small (linear conditions), the response is a sinusoid with the same frequency but shifted in phase. This implies that the impedance of a

system contains two different information i.e. the change in amplitude between imposed and measured signal and the phase shift. In effect, a common representation for impedance is the use of a complex number that, because of the real and imaginary part necessary to define it, can carry these two information.

So, if impedance is represented as an imaginary quantity in polar form, it captures both magnitude and phase characteristics:

$$Z = \|Z\| \, e^{j\theta}$$

where $\|Z\|$ represents the ratio between the imposed signal and the measured response, while is the phase difference between the two.

Another way to represent an imaginary quantity is to use the Cartesian form; in this way, the impedance is divided in its "real" and "imaginary" component, Z_{re} and Z_{im} respectively, so that

$$\sqrt{Z_{real}^2 + Z_{imag}^2} = Z$$

and

$$\arctan\left(\frac{Z_{imag}}{Z_{real}}\right) = \theta$$

It must be noted that "imaginary" is used here as a definition, by analogy with the representation of complex numbers; as described above, both Z_{real} and Z_{imag} have a very real physical meaning.

So, when a system is excited with a sinusoidal signal of a given frequency, the measured impedance will have a magnitude and phase (or Z_{real} and Z_{imag} , alternatively) specific for that frequency. The measurement of impedance in a broad range of frequencies gives then rise to the impedance spectrum of the investigated electrochemical system. As an example, resistors have an impedance which is real and independent of the frequency ($Z_R = R$), while capacitors give a pure imaginary response, which is frequency-dependent ($Z_C = \frac{1}{C\omega j}$).

Electrochemical processes in a SOFC can be imagined as a sequence of equivalent circuits. Every elementary reaction step, as a first approximation, has an associated resistance R_p (related to the inverse of the rate constant) and an associated capacitance C_{dl} (related to the accumulation of reactive species, for instance a double layer of charged products or reactants). On the other hand, an electrochemical device presents a series of pure ohmic resistances put in series (R_s) with the reactive system, such as the electrolyte resistance, the contact resistance at the current collection, etc. Such a simple equivalent circuit, called a Randles circuit, is presented in Figure 2.6 A. At very high frequencies, the impedance measured on this circuit will be fully real (no phase shift between imposed signal and measured response) and will correspond to R_s; this is because the imposed frequency is too high for the process to adapt, and the alternate signal "short-circuits" the associated capacitor. In the other extreme case, at very low frequency, there will be at every moment the equilibrium of the process with the imposed signal; in this situation the capacitor is "fully charged", the signal will be forced to measure the resistance associated with the process, and the impedance measured will correspond again to a real value, equal to $R_s + R_p$. An intermediate situation happens when the signal frequencies are near the "characteristic frequency" of the process; in this case, the process will "resonate" with the signal, and give rise to a phase shift.

A common representation for the spectrum obtained is called a Nyquist plot, where values of Z_{imag} are displayed as a function of Z_{real}. Figure 2.6 B illustrates the Nyquist representation of the spectrum associated to a Randles circuit. In a Nyquist plot, each ideal process generates a semi-circle; the characteristic frequency of the process ($f = \frac{\omega}{2\pi}$) is the one giving the highest phase shift, i.e. the frequency of the point at the apex of the semi-circle.

When measuring the impedance spectrum of an electrochemical cell, the response is much more complex than the one presented in Figure 2.6. On the one hand, there are multiple processes happening at the same time, and on both electrodes; on the other hand, the behavior of real systems differs from ideal circuits. There is an obvious difference between the simple elements of an idealized electrical circuit and the three-dimensional,
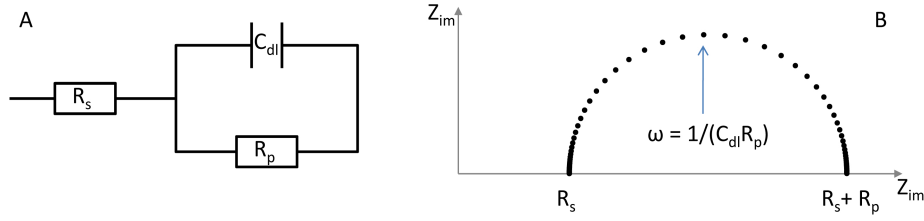
Figure 2.6. A) Equivalent circuit of a simple process, the Randles circuit B) Nyquist plot originated numerically for a Randles circuit.

multi-layered, porous structure of a technological SOFC electrode, which leads to non-ideal responses. The simplest way in which the deviation from the ideal situation can manifest itself is a depression of the semi-circle associated with a given process. Such depressed semi-circle is fitted with an alternative circuit containing a so-called Constant Phase Element (CPE), representing an imperfect capacitor and whose impedance is $Z_{CPE} = \frac{1}{Q(\omega j)^n}$. Here n contains the deviation from the ideal situation: when $n = 1$ the CPE behaves like a ideal capacitor, while for $n = 0$ it behaves like a resistor.

Electrochemical impedance spectroscopy in SOFCs

EIS is a very sensitive technique, and is able to capture all the processes occurring in the cell. Diffusion of gas component towards and from the active sites, adsorption and disso-ciation of molecules, charge transfer, incorporation of ions in the lattice of the electrolyte all give their contribution to the impedance of the cell and have been classified in the lit-erature [86, 87], each one with a determined characteristic frequency domain. Figure 2.1 shows a schematic reaction path in a fuel cell, while table 2.1 reports the characteristic frequencies of the elementary steps and their dependence to operating parameters [86, 87]. In standard fuel cells, the thickness of the anode support (200 to 1000 μm) is much bigger than in cathode layers (few tens of μm), so that pore diffusion processes are usually consid-ered only in the former, including H_2 diffusion towards the active sites and H_2O diffusion towards the surface. Another process included in the table and not presented in Figure 2.1 is the gas conversion impedance, involving a change of composition of the gas flow at very

Process	Frequency	Temperature	Sensitivities
O^{2-} transfer at the LSM/YSZ interface	10 kHz - 50 kHz	700 - 850 °C	$pO_2 \rightarrow$ low current $\rightarrow$ low
Charge transfer at the Ni/YSZ interface	300 Hz - 20 kHz	700 - 850 °C	fuel composition
O_2 adsorption and dissociation on LSM	10 Hz - 1 kHz	700 - 850 °C	$pO_2 \rightarrow$ low current $\rightarrow$ high
Diffusion (anode)	20 Hz - 100 Hz	700 - 850 °C	pH_2 /pH_2O
Conversion (anode)	0.5 Hz - 10 Hz	700 - 850 °C	pH_2 /pH_2O current

Table 2.1. Elementary steps for the electrochemical reaction in SOFC

low frequency at the anode surface because of the small polarization necessary to perform the EIS measurement. To complete the description, it must be added the contact resistances and the resistance of the electrolyte (which would represent the stand-alone R_s in the equivalent circuit), and an inductive element L, due to the positioning and lenght of the measurement wires. The latter, with an order of magnitude of 10^{-7} - 10^{-8} H, gives a contribution in the high frequency part of the spectra and can introduce an error in the estimation of the R_s.

So many processes with characteristic frequencies relatively close to each other cause an EIS spectrum to be difficult to analyze because of the partial overlapping of depressed semicircles. The identification and quantification of the processes can be problematic and deconvolution can lead to errors. In the next sections more details about measurements and their analysis will be given.

Chapter 3

Experimental

In this chapter the experimental setup, methods and protocols used for the preparation of the electrochemical cells are presented. Furthermore, the validation of segmented multicathode testing, an original testing strategy developed in this thesis, is presented. Characterization techniques will be introduced; if necessary, more details will be provided in chapters containing experimental results.

Results concerning the multicathode testing strategy exposed in this chapter were published in the following papers:

- P. Tanasini, J. A. Schuler, Z. Wuillemin, M. L. Ben Ameur, C. Comninellis, and J. Van herle. Segmented cell testing for cathode parameter investigation. Journal of Power Sources, In Press, corrected proof. doi :10.1016/j.jpowsour.2010.08.034.

- J. A. Schuler, P. Tanasini, A. Hessler-Wyser, and J. Van herle. Rapid chromium quantication in solid oxide fuel cell cathodes. Scripta Materialia, 63(8) :895-898, 2010.

3.1 Electrochemical cell

Two types of anode-supported cell configurations have been used in the present work, the button cell, and the multicathode cell. The anode-supported cell configurations reproduce closely the operation of a stack cell, with the additional advantage of homogeneous and controlled conditions.

3.1.1 Anode-supported button cell

Button cells have been obtained by the deposition of a cathode layer on an anode-supported cell covered with a thin electrolyte (Anode Support and Electrolyte, ASE). Anode supports consisted of a 250 μm thick cermet layer manufactured by tape casting (HTceramix SA, Switzerland) using 55 wt% NiO and 45 wt% yttria-stabilized zirconia co-sintered at 1400 °C with a 5 μm thick 8% yttria-stabilized Zirconia (8YSZ) electrolyte (fig. 3.1). The composite cathode layer ($S = 1$ cm^2) was made of lanthanum-strontium manganite, either $(La_{0.75}Sr_{0.25})_{0.95}MnO_{3\pm\delta}$, indicated as LSM25 (Praxair, U.S.), or $(La_{0.70}Sr_{0.30})_{0.90}MnO_{3\pm\delta}$, indicated as LSM30 (Fuel Cell Materials, U.S.) mixed with 8YSZ in a 1:1 v/v ratio. The composite layer was deposited by screen printing and sintered typically at 1100 °C for 1 hour. Current collection was performed on cathodes through the application of a non-sintered $(La_{0.65}Sr_{0.35})_{0.95}MnO_{3\pm\delta}$ (LSM35, Fuel Cell Materials, U.S.) layer and of a fine platinum mesh connected to the leads. The anode side was contacted with a piece of Ni foam, placed opposite to the cathode and connected to the leads (Fig. 3.2).

Such cells were used for electrochemical testing such as steady-state polarization in order to study long-term behavior, electrochemical impedance spectroscopy (EIS) and I-V curves; figure 3.2 shows the electric configuration adopted for testing and data acquisition.

3.1.2 Multicathode anode-supported cell

An original segmented cell configuration has been adopted in order to perform simultaneous testing of several cathodes deposited on the same ASE. Multicathode cells used in
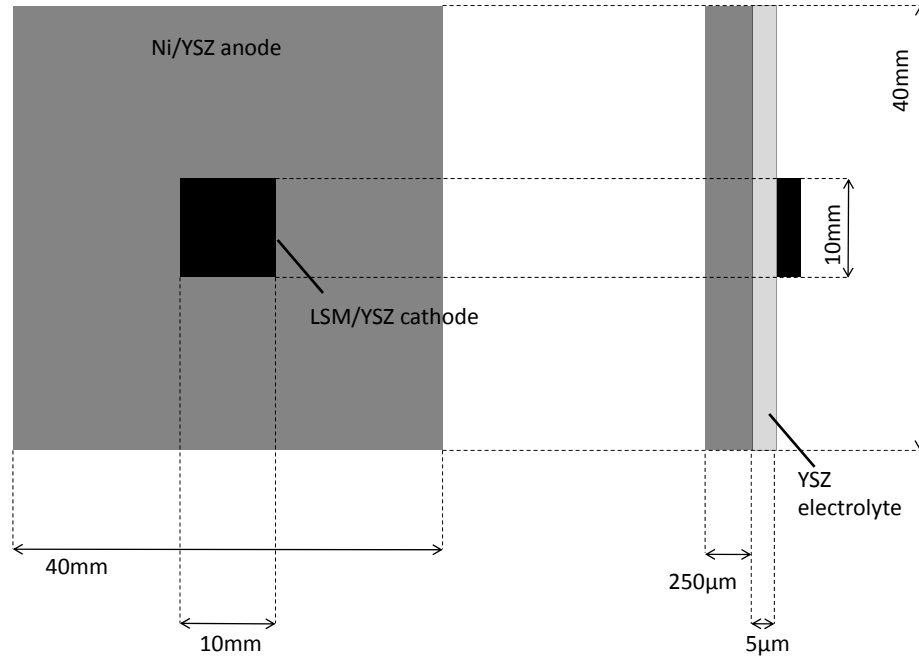
Figure 3.1. Schematic representation of a button cell on anode support and electrolyte (ASE).

this work allowed carrying out four tests in parallel, as shown in figure 3.3. This allows decreasing the total experimental time and ensuring the same operating conditions for the four segments. Multicathode cells have been used to investigate the effect on long-term operation of variables like current density, cathode composition and cathode thickness.

The ASE that have been used have the same characteristics of those described in 3.1.1. Cathode layers varied their composition and thickness depending on the test; sintering was performed typically at 1050 °C for 1 hour. Current collection was performed on cathodes through the application of a non-sintered LSM35 layer and the application of a fine gold mesh connected to the leads. The anode side was contacted with a single piece of Ni foam connected to the leads, centered on the anode support and covering the surface opposite of the four cathodes.

Such cells were used for electrochemical testing such as steady-state polarization to study aging, EIS and IV curves characterization; figure 3.4 shows the electric configuration
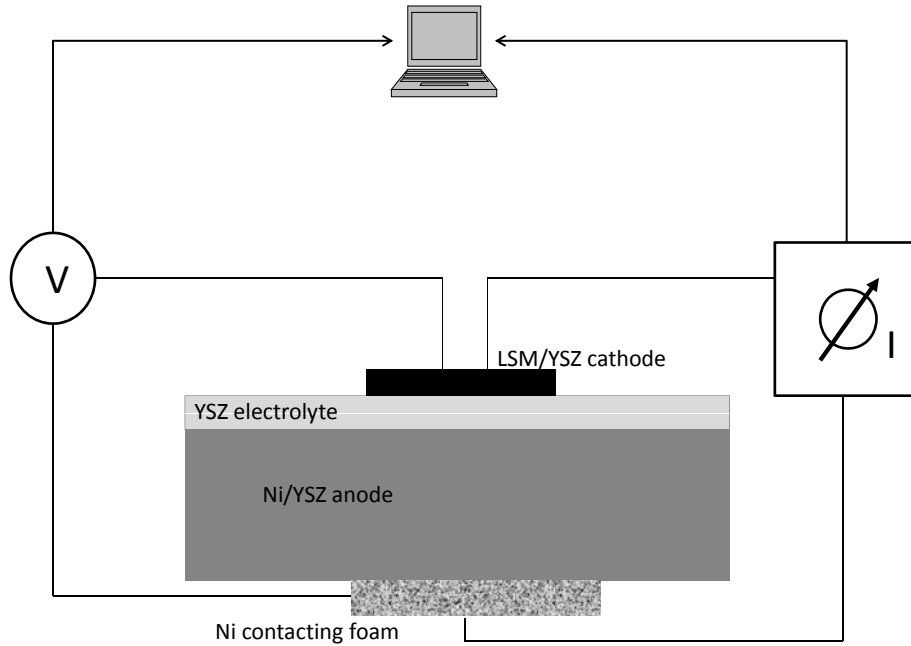
Figure 3.2. Electric scheme for button cell testing.

adopted for multicathode testing and data acquisition.

3.1.3   Development and validation of segmented cell testing

Motivation

As a consequence of the recent improvements allowing to achieve performance losses below 1% over 1000 hours of continuous operation, the study of slow, simultaneous, interrelated degradation mechanisms is difficult due to the long testing time needed to measure significant variations in performance; further, the separation and quantification of the contributions of each phenomenon is even more challenging. Furthermore, degradation studies need robust and stable test benches permitting to identify changes of the order of 1% after months of aging. Operating conditions must be rigorously the same for all the tests of an experimental campaign, since even small changes in temperature or gas distribution affect
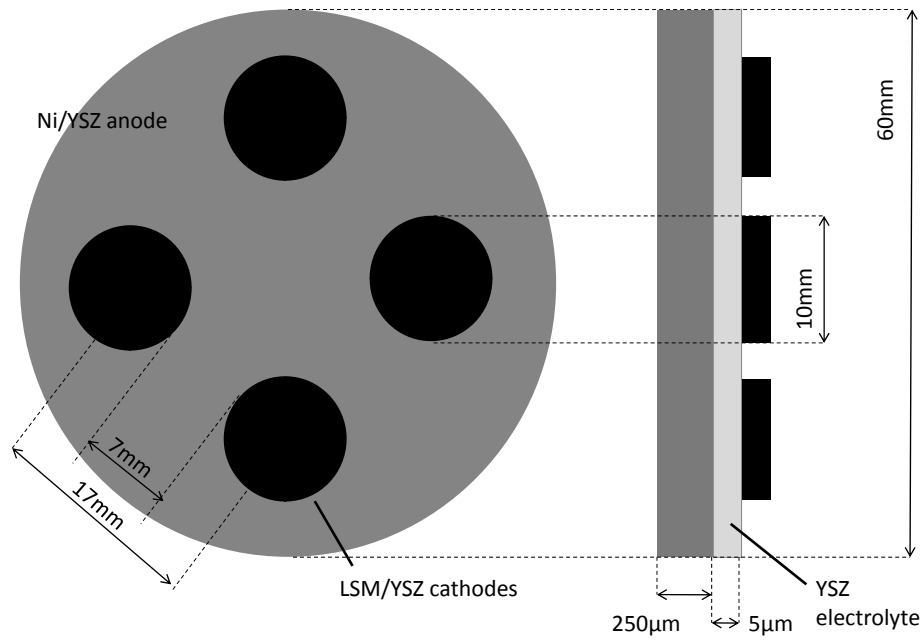
Figure 3.3. Schematic representation of a multicathode cell on anode support and electrolyte (ASE).

the cell behavior and mask the influence of a given studied variable. Moreover, the influence of unavoidable impurities from installation, gas phase, raw materials can strongly affect the results [88], jeopardizing the success of a series of tests. Reproducibility and testing time are key issues in SOFC research.

An original segmented cell configuration [89] has been adopted in order to carry out four tests in parallel, as shown in 3.1.2, aiming on the one hand to reduce the time needed for an experimental campaign and, on the other hand, to ensure reproducibility of operating conditions. These two objectives are achieved by the so-called segmentation of a cell, allowing parallel simultaneous testing of each segment under the same operating conditions.

Segmentation had been adopted by Wuillemin and co-workers [90, 91] from this group, to give spacial resolution of degradation phenomena in a stack repeat element, which has
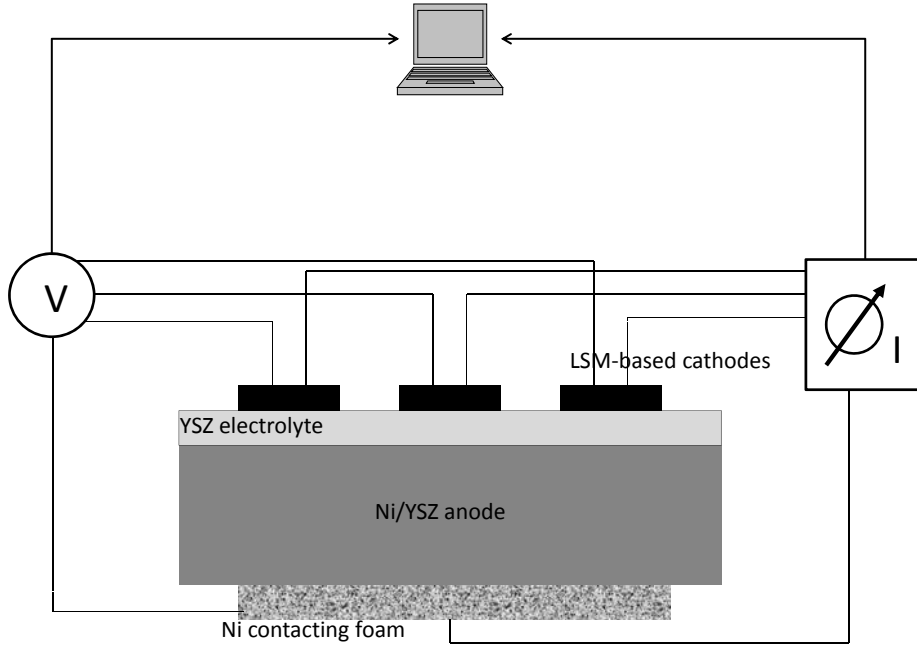
Figure 3.4. Electric scheme for multicathode cell testing.

distributed values of important parameters such as temperature, gas concentration and current density. In the present work, the presence of separate cathodes (segments) on the same support permitted the investigation of the influence of a single variable (such as cathode thickness and composition, or current density) in the same testing environment and on the same anode support. Moreover, in the time span needed for long-term testing, the unavoidable and unpredictable small fluctuations of experimental conditions (gas feeding, furnace temperature etc.) have the same effect on all the segments, giving higher reliability for the analysis of the results.

Even so, in SOFC testing experimental procedures and preparation are critical to ensure reproducible results; the following sections explain the theoretical modelling of the cell and then the development and improvement of the experimental procedures to perform segmented cell testing and the validation done to confirm the reproducibility of the results.
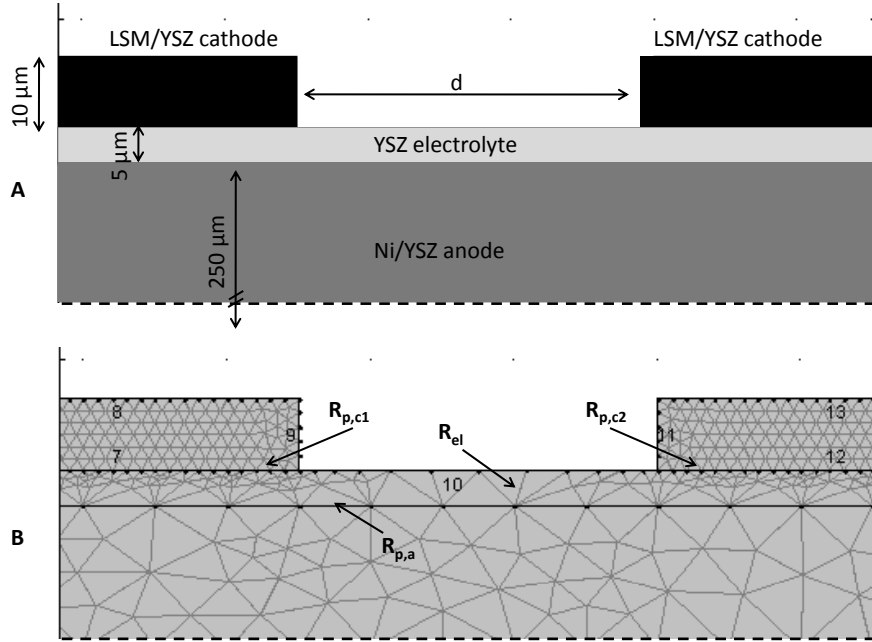
Figure 3.5. A) Geometry used for calculating the distribution of potential through computer simulation. The distance d has been fixed here at about 60 μm, a value much more conservative than the 70 mm of the real cell. B) Meshing used for the finite element calculation. It is fine in the cathode and coarse in the anode; the electrolyte presents a mesh progressively finer near the interface with the cathode, where the bigger gradient is expected.

Modelling of potential distribution

Computer simulations have been carried out in order to estimate the possible interaction of two cathodes deposited on the same anode support, with the geometry used for the multicathode cells. In effect, an influence of one cathode on the other would have negative effects on both the real operation conditions during the test and the interpretation of the results. The point of interest in determining if there is an influence of one cell on the others is the so-called secondary distribution of current and potential, which is determined by the geometry of the cell, the conductivity of the electrolyte and the overpotential at the electrode interfaces. The system studied is shown in Figure 3.5 A, with a geometry related to a cross-section of the cell presented in Figure 3.3.

The calculations for the distribution of the potential in the system have been done using Ohm's law:

$$\nabla V = -\rho i \qquad (3.1)$$

Which, combined with the principle of charge conservation valid in a conductor ($\nabla i = 0$) gives the following differential equation:

$$\nabla \left(-\frac{\nabla V}{\rho} \right) = 0 \qquad (3.2)$$

Assuming a constant resistivity in the whole domain, we obtain Laplace's equation, used in Comsol for deriving the distribution of overpotential:

$$\nabla^2 V = 0 \qquad (3.3)$$

- The boundary conditions are: $V = $ const on the external surface of the anode.

- $\frac{\partial V}{\partial \vec{l}} = 0$ on the insulating surfaces (all the faces in contact with the gas, for instance). $\vec{l}$ is the vector normal to the surface.

- $i_{cathode} = -i_{anode}$; the current entering the cathode must be equal to the one exiting the anode

In order to simplify the problem, we introduced the polarization resistances as if they where interfacial resistances located at the electrode/electrolyte junctions. It is possible to consider this junction as volume with very small thickness, and with a resistance equal to the polarization resistance of the corresponding electrode [92]. The resistances have been considered constant for anode and cathode, meaning that their dependence from the current density has been ignored. The resistivity of the electrolyte has been calculated from typical values for the ohmic resistance of SOFC cells; the contribution of the contact resistances to the ohmic resistance of the cell has been neglected.

Comsol Multiphysics®, a simulation program based on the finite elements method, has been used to solve Eq. 3.1-3.3 along with the boundary conditions presented above in the

2D geometry illustrated in Figure 3.5 A. Three domains have been identified: the anode, the electrolyte, and the cathode; only the electrolyte has a considerable resistance (R_{el}); in addition, interfacial resistances have been applied at the cathode/electrolyte ($R_{p,c1}$ and $R_{p,c2}$) and anode/electrolyte ($R_{p,a}$) interfaces to represent the polarization resistances. The meshing applied to the system and the resistances mentioned above are shown in Figure 3.5 B. Such a simplified system can be simulated as a simple electrical circuit to derive the potential distribution.

Figure 3.6 shows the case of two identical electrodes operated at the same current density. It is possible to see that the edge effect extends over a small distance of about 10 μm away from the cathode's boundary, i.e. much smaller than the actual distance between two cathodes shown in Figure 3.3.

In practice, two cathodes are seldomly used in the exact same conditions, since either they have a different polarization resistance or they are operated at different current density. This situation brings necessarily to a difference in potential between the two cathodes, and therefore there could be the possibility of a deformed distribution of potential caused by the passage of current between the two cathodes. Simulations have been carried out at the same current density and different polarization resistance and vice versa, and the results are shown in Figure 3.7 A and Figure 3.7 B, respectively. As it can be seen, the two potential distributions are not overlapping even at a distance as small as 10 μm.

In conclusion, computer simulations prove that the multicathode cell testing is not affected by undesirable interactions between segments.

Gas distribution

Four nominally identical cathodes have been deposited on one ASE and tested. After reduction, the segments have been tested at 850 °C in 3% humidified H_2.

Figure 3.9, which reports the I-V curves taken at the beginning of the test, shows that a difference of about 40 mV is present between the open circuit voltages (OCV) of the different segments; the difference persists but is reduced when passing to higher current densities. This could be related to a inhomogeneous distribution of $H_2O_{(g)}$ back-diffusion
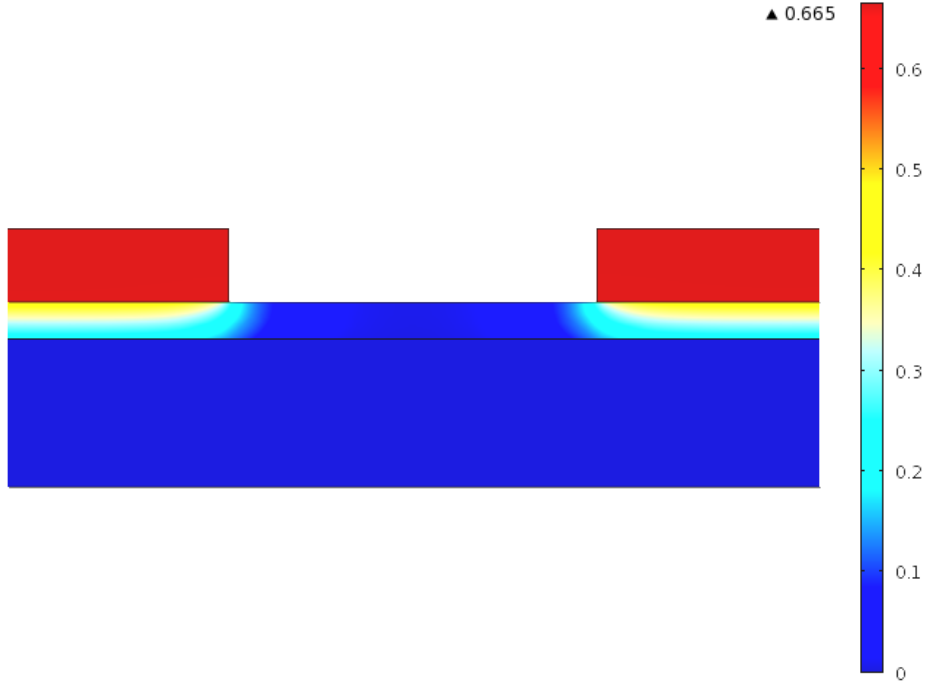
Figure 3.6. Simulations obtained for two identical cathodes operated under the same conditions. The parameters used for the simulation are: $i_{c1} = i_{c2} = 1.2$ A/cm^2, $R_{p,c1} = R_{p,c2} = 0.4\,\Omega\,\text{cm}^2$, $R_{el} = 0.2\,\Omega\,\text{cm}^2$, $R_{p,a} = 0.2\,\Omega\,\text{cm}^2$.

from the combustion front at the cell edge (Fig. 3.12) since an insufficient steam content of the fuel (3% in this case), combined with an ill-positioned cell and/or insufficient gas flow to the anode side can lead to unequal diffusion of $H_2O_{(g)}$ at the anode side; this hypothesis was confirmed by EIS. In effect, Figure 3.8 shows the Nernst potential of the cell calculated versus fuel composition, considering a progressive substitution of $H_{2(g)}$ with $H_2O_{(g)}$; it is clear form the slope of the curve that at low water content the potential of the cell is highly sensitive to variations in composition, such as the increase in water content caused by cell operation. Calculations show that the sensitivity is lowered by a factor of 2 passing from 3% to 7% water content in the feeding gas.

Indeed, the increase of the water content in the fuel feed to 7% and a careful positioning of the cell permitted to achieve a uniform gas composition, confirmed by the close value
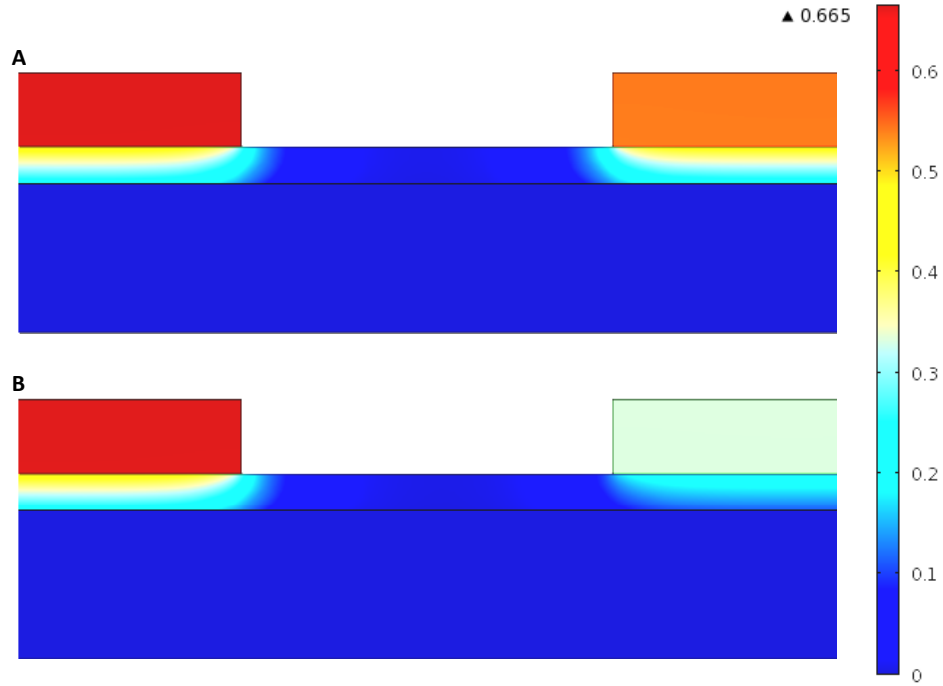
Figure 3.7. A) Two cathodes with different polarization resistance are operated at the same current density: $i_{c1} = i_{c2} = 1.2$ A/cm^2, $R_{p,c1} = 2R_{p,c2} = 0.4\,\Omega\,\text{cm}^2$. B) Two cathodes with the same polarization resistance are operated at different current density: $i_{c1} = 2i_{c2} = 1.2$ A/cm^2, $R_{p,c1} = R_{p,c2} = 0.4\,\Omega\,\text{cm}^2$. In both cases, $R_{el} = 0.2\,\Omega\,\text{cm}^2$, $R_{p,a} = 0.2\,\Omega\,\text{cm}^2$.

range of the segments' OCVs in successive tests.

Cell contacting

Four segments of different thickness have been tested at 850 °C in 7% humidified H$_2$ at 0.6 A/cm^2 for about 1100 hours. With respect to 3.1.3, the increase of the water content in the fuel feed (from 3% to 7%) and a careful positioning of the cell permitted to achieve a uniform gas composition.

Figure 3.10 shows the operating voltage of the four segments during operation; the monolayer cathode (5 μm) showed worse performances than the three other cathodes, which had a quite similar behavior after activation. This has been attributed to the limiting effect of the layer thickness, which is smaller than the theoretical active layer for
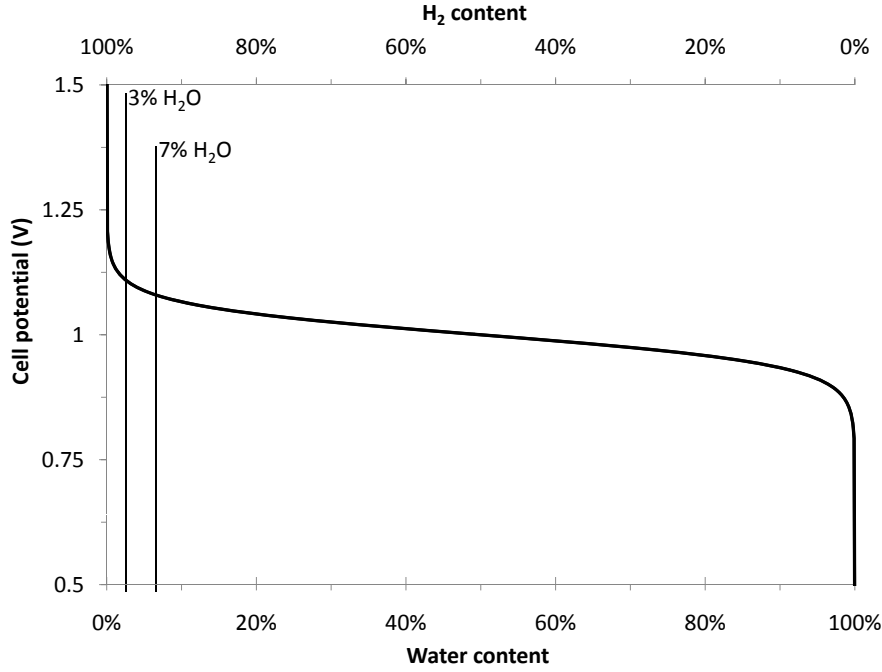
Figure 3.8. Cell potential at equilibrium for fuel compositions corresponding to different $H_{2(g)}$ / $H_2O_{(g)}$ mixtures, showing that the cell potential is sensitive to $H_2O_{(g)}$ fluctuations at low water contents.

the 5 μm cathode [63, 64].

The 15 μm-thick cathode has an initial performance worse than the 10 μm-thick and 20 μm-thick cathodes, which evolve towards a similar performance with time. At the beginning of the test the ohmic resistance, found with EIS measurements, is higher for segment with the 15 μm-thick cathode (about 0.5 Ωcm^2) than for the other three segments, which showed similar value of about 0.2 Ωcm^2. During operation at high temperature and under the pressure of the metallic flanges, the contacting meshes increase their adhesion to the electrodes and improve the electrical contact. While this effect increases the quality of all contacts, it is particularly important on the cell showing a higher resistance, leveling up the differences. At the end of the test, all ohmic resistances were close around a value of 0.12 Ωcm^2.
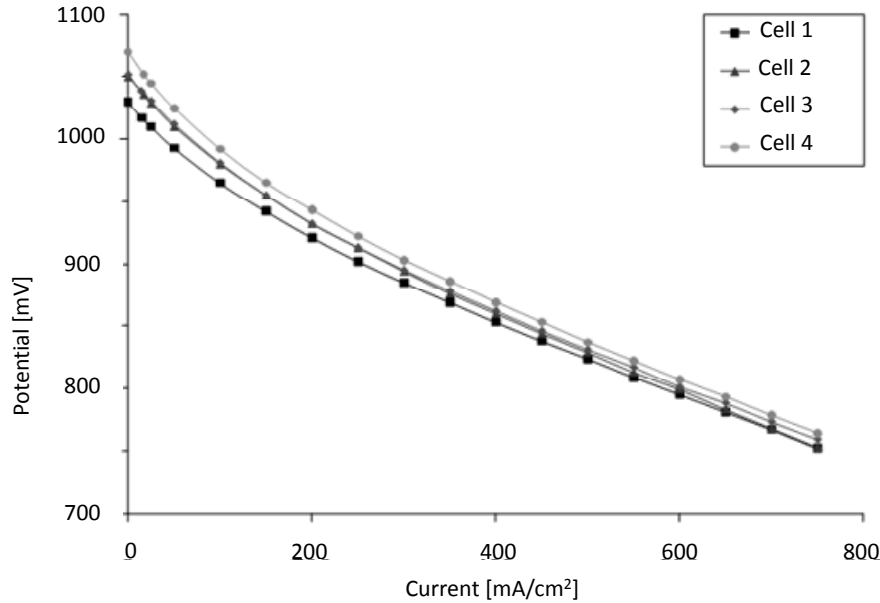
Figure 3.9. Current-voltage curves taken on nominally identical segments. A difference of several mV is present at OCV, attesting a non-homogeneous gas distribution at the fuel side. The difference is reduced while passing current; the general behavior of the segments is very similar

In order to increase the contact quality of the current collection, a thin layer of gold paint has been applied on the gold meshes on the cathode side before pressing it against the cathode. This methods gives satisfying results, permitting to obtain better starting conditions. However, a general improvement of the contacts usually happens on all segments in the first hundred hours of operation.

Validation

Four cathodes made of LSM30 and Mn-enriched 8YSZ were deposited. The dissolution of Mn oxide into the 8YSZ powder was carried out by heating for 100 hours a mixture of 8YSZ powder and Mn-acetate at different temperatures (900 °C, 1000 °C and 1100 °C). The heat treatment temperature controlled the theoretical amount of Mn oxide dissolved
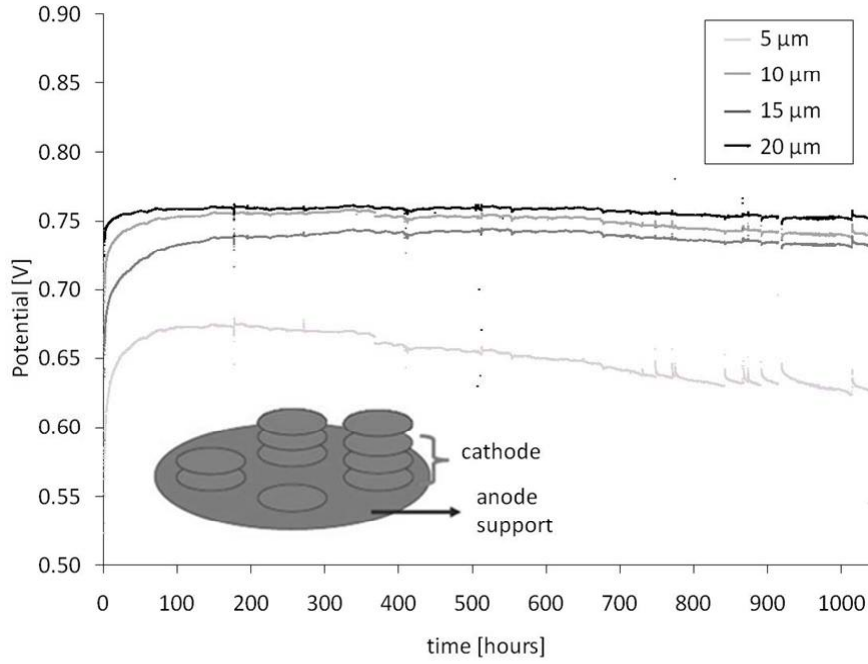
Figure 3.10.   Operating voltage of segments of different thicknesses.   After activation, cell 1 (5µ thick) has limited performance while thicker segments have a similar and better performance. Cell 3 (10µ thick) begins with a poorer performance than cell 2 and 4 because of a worse contacting; the difference is leveled out after some time at operating temperature.

into the 8YSZ phase; the concentrations have been calculated by extrapolating literature data [46, 93] and were expected to be 2.5%, 4.5% and 6.5% moles of Mn oxide per mole of YSZ for 900 °C, 1000 °C and 1100 °C, respectively. The Mn-enriched powders, as well as the as-received 8YSZ powder, were ground mechanically in order to decrease the average particle size and were then mixed with LSM30 to prepare the cathode pastes deposited on the anode support. The 2.5% Mn-enriched YSZ was over-ground to a $d_{v,50}$ of 0.2 µm unlike the other Mn-YSZ powders, including the as-received 8YSZ, all ground to 0.3 µm; the as-received LSM30 also had a $d_{v,50}$ of 0.3 µm. The cell was then sintered at 1050 °C for 1 hour; the cathodes, covered with a pure LSM35 current collection layer, were contacted with gold meshes.

The segments have been tested at 850 °C in 7% humidified H_2. Initial characterization
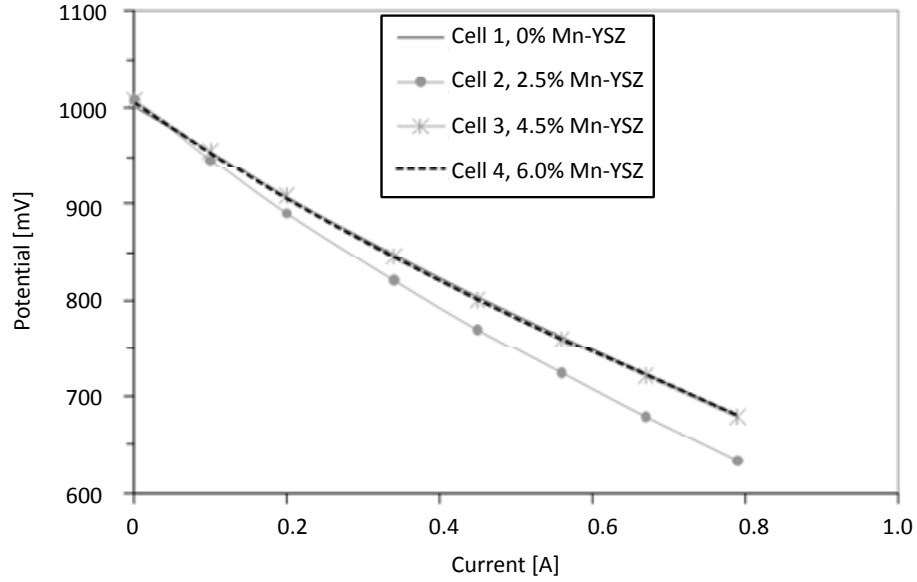
Figure 3.11. Current-voltage curves taken on segments of different composition. The curves are overlapped for segments with the same microstructure while cell 2, containing over-ground YSZ particles, shows the same OCV but poorer performances.

showed a very good reproducibility for the three cells with the same microstructure while the cell with finer YSZ (2.5% Mn-enriched) had poorer performances (Fig. 3.11).

Electrochemical characterization with EIS could be done at different operation times, temperatures, gas compositions and current densities. The fuel composition was obtained by mixing H_2 and Ar in different proportions. The analysis of EIS data permitted to characterize the system, as described in Section 5.1.

Conclusions

Segmented cell testing has been proved, theoretically and experimentally, to be a reliable strategy to achieve better reproducibility for SOFC measurements by avoiding the inevitable fluctuation for a series of successively run tests. Moreover, simultaneous testing

increased n-fold the data output per experiment, implying a considerable economy of time.

This analysis demonstrates that several parameters like current density, electrode composition, electrode thickness, and gas phase composition can be varied maintaining the flexibility of single button-cell configuration.

Moreover, the segmented cell test has shown that typical artifacts affecting SOFC measurements (e.g. difference in initial ohmic drop) can be easily identified by comparing the operation potential of the segments.

3.2 Electrode preparation

3.2.1 Preparation and characterization of the active material (ceramic powder)

Particle size of the active electrode material is an important parameter affecting the morphology and thus performances and aging behavior of SOFC electrodes (see 4). Particle size distributions (PSD) and average particle diameters ($d_{v,50}$, defined as the diameter that, in the PSD, separates the powder in two halves of the same volume) have been measured by laser diffraction on a Mastersizer (Malvern Instruments, UK).

In certain cases, as-received powders have been ground to decrease their average particle size. A typical case was the grinding of YSZ powder in order to achieve an average particle diameter ratio $d_{v,50,LSM} : d_{v,50,YSZ}$ in a composite powder close to unity, which is a key parameter for percolation. Grinding was performed mixing a suspension containing the ceramic powder and a 4% solution of poly-acrylic acid (PAA) in water. The ratio powder:PAA solution was about 1:1 by weight. An axial mixer with Teflon® blades was inserted in a covered ceramic cylinder containing the suspension, in presence of zirconia balls of 2 mm diameter. The ratio powder:spheres was about 1:10 by weight. Grinding was then performed for several hours (up to 24 hours) at 1500 r.p.m., in presence of external water cooling. Periodic $d_{v,50}$ measurements were performed in order to stop the grinding when the desired value was reached.

The suspension was then dried overnight in a furnace at 90 °C, followed by the burn-out of the PAA for 4 hours at 400 °C in a crucible while feeding 300 Nml/min of air for the oxidation of organic compounds.

3.2.2 Cathode preparation

Cathode layers have been deposited by screen-printing technique, consisting in the application of an ink - composed by the ceramic powders, a solvent and a thickener - through a fine metallic grid. The grid is partially covered with a plastic material so that non-printing areas are blocked off. The ink is wiped across the screen with a rubber blade to pass through the unblocked zones and reach the substrate. Screen-printing is a reproducible technique that permits the control of the surface and thickness of the deposited layer if parameters like viscosity and solid content are carefully controlled. This technique has the advantage to be easy to scale up from lab scale to industrial production: the deposition on the industrial scale is automatically performed by programmable machines, on the same principle.

The inks were made of powders Lanthanum-Strontium Manganite (LSM25 or LSM30) with different composition mixed with an electrolyte powder, either yttria-stabilized zirconia (8% Y_2O_3 - 92% ZrO_2, Tosoh, Japan, indicated as 8YSZ) or scandia-stabilized zirconia (10% Sc_2O_3 - 89% ZrO_2 - 1% CeO_2, Praxair, US, indicated as SSZ). The composite powder was prepared mixing the LSM and electrolyte powder with ethanol and an organic dispersant (courtesy of SOFCpower, confidential composition) in a ball-mill for 24 hours in presence of zirconia spheres. After evaporation of the ethanol, the inks were obtained mixing the composite powder on an alumina triple-roll mill with 3.2% ethyl-cellulose in terpineol as a binder (ratio powder/binder around 1.36).

Inks were printed layer by layer through stainless steel mesh on the supports; each layer consisted of approximately 5 μm of cathode material. Drying of the terpineol was performed on a hot plate at 70 °C for 10 minutes. The cells were then sintered at high temperature (between 1050 °C and 1100 °C) for 1 hour, with an intermediate debinding
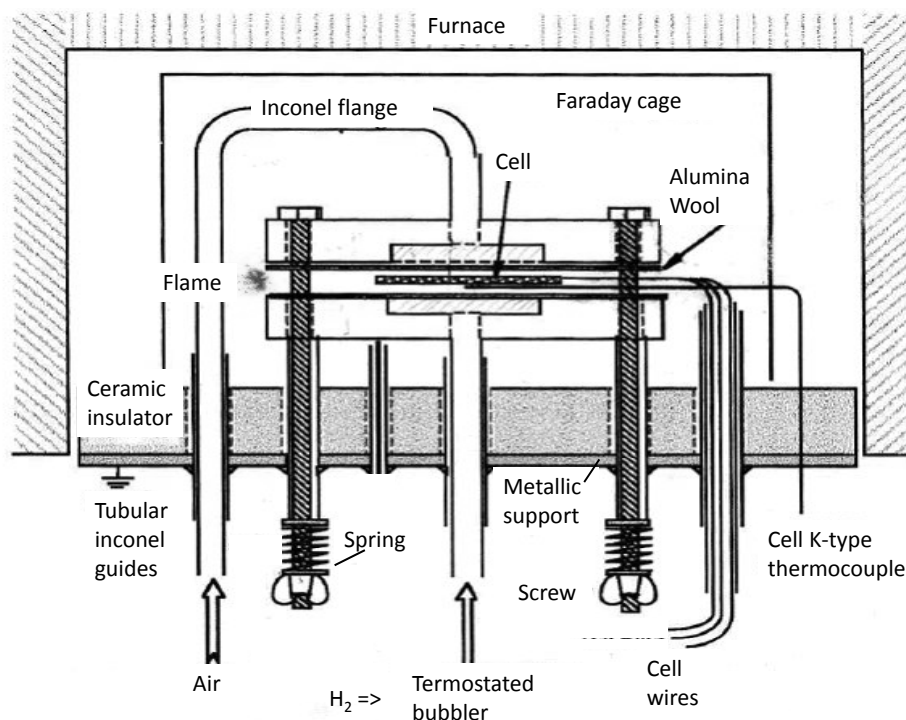
Figure 3.12.   Schematic representation of the experimental setup during operation.

period of 1 hour at 400 °C to allow burning the organic compounds. The cathodes were then covered with a current contacting layer made of pure LSM35 ink with 3.2% ethyl-cellulose in terpineol as a binder (ratio powder/binder around 1.5), deposited by screen printing.

3.3   Cell testing

Cell operation with both types of anode supports was carried out in a furnace (Rohde, Germany) with a Bentrup TC 505 temperature controller. The cells were placed between two alumina felts and inserted between two metallic flasks (figure 3.12); the test rig was then compressed with calibrated springs in order to maintain the metallic meshes under constant pressure on the electrodes. The flasks had central gas inlets in order to feed air to the cathode side and humidified H_2 to the anode side.

There was no sealing between the two compartments so that, during the fuel cell testing, excess H_2 was post-combusted around the cell. Gas flow was adjusted in order to maintain the flame front far from the electrochemical reaction and to minimize H_2O diffusion toward the center of the support. Typical values for air and H_2 flow rates were 600 Nml/min and 300 Nml/min respectively. Local temperature measurement was done through a thermocouple placed near the center of the support, placed on the air side. Reduction of the anode supports was conducted at 850 °C while feeding air to the cathode side and H_2 diluted in Ar to the anode side. The reduction of the NiO took place by a stepwise replacement of argon by hydrogen (H_2 content varied from 10% to 100%).

The polarization of the cell was done in galvanostatic mode; for multicathode testing a four-channel active load built in-house was used, while for button cell testing the load was applied with a galvanostat (Amel Srl, Italy). Measurements were performed in a four-wire configuration. Potential difference, current and temperature data were acquired and stored in a computer through a multichannel on-line acquisition device (Agilent, US). Electrochemical impedance spectroscopy measurements (EIS) and current-voltage curves were taken with an Autolab® PGstat30 (Eco Chemie, the Netherlands).

3.4   Characterization techniques

3.4.1   Electrochemical impedance spectroscopy (EIS)

EIS measurement conditions

Measurements were performed with a computer-controlled Autolab® PGstat30 (Eco Chemie, the Netherlands), using the Autolab® software Frequency Response Analyzer. Generally galvanostatic mode was used, imposing a $\pm$ 30 mA/cm^2 AC current signal and measuring the voltage response. A current bias was imposed, usually between 0 to 0.7 mA/cm^2 and the spectrum was measured sweeping from high to low frequencies over the range from 500 kHz to 0.1 Hz.

Measurements were taken with the same gas flow conditions used for operation and aging: typically air and H_2 flow rates were 600 Nml/min and 300 Nml/min respectively. However, in order to achieve a better understanding of the processes controlling the polarization resistance of the cell, some EIS measurements were done with variation in gas composition, diluting either the H_2 or the air with Ar. Also, measurements were carried out at different temperatures, between 700°C and 900°C.

Analysis of EIS spectra

Spectra were analyzed in order to extract information.

The EIS Spectrum Analyzer freeware program (© A. S. Bondarenko and G. A. Rago-isha, http://www.abc.chemistry.bsu.by/vi/analyzer/) was used to perform fitting with equivalent circuits, enabling to determine the resistance and capacitance of each fitted process. However, fitting on full cells demands a pre-calibration of the fitting parameters [86, 87]. In effect, each process brings two adjustable parameters (three if the process is represented as a CPE), and the fitting of a 100-points spectrum with a set of fifteen parameters corresponding to the process presented in table 2.1 has too many degrees of freedom; a solution obtained in these conditions is not necessarily representative of the reality, and the values obtained are not reliable. The fitting made on spectra coming from pellet measurements are more easy to fit reliably, since only cathodic processes are present.

A Matlab® code developed in-house by Z. Wuillemin at EPFL [91] was used to perform analyses on complex spectra. A module developed during the present work enabled the extraction of data from a series of Autolab® data-files, in the form of a 3D matrix. Several routines working on the data matrix permitted:

- the correction of the parasitic inductance of the measurement wires

- the smoothing of the spectra through a fitting polynomial

- the re-sampling of all the spectra, in order to have values at the same frequencies (necessary if the measurements were not done in the same range and with the same intervals)

- the point-by-point subtraction of one spectrum to others, in order to capture the variations of processes from one set of conditions

- the δZ_{real} function [94] as a function of the frequency, obtained as the derivative of Z_{real} This function shows peaks at characteristic frequencies, and a better resolution than the more common Z_{imag} plotted as a function of frequency (Bode plot).

This tool allowed a good investigation of limiting processes; in the case of long-term tests, it was possible to identify which processes were affected by degradation.

3.4.2   Scanning electron microscopy (SEM)

SOFC samples have been studied by Scanning Electron Microscopy (SEM) with a FEI XL-30 SFEG Sirion in order to have both qualitative information and quantitative measurements. SEM was used to investigate the microstructure of porous electrodes, identifying the phases and measuring the average particle diameter. Furthermore, it has been used to do post-mortem analyses on tested cells in order to localize and measure the presence of contaminating substances such as chromium species.

Sample preparation

Preparation was necessary prior to SEM imaging: usually a part of the cell from the center of the cathode area was cut and the section was polished in order to investigate the microstructure. To preserve the microstructure during grinding, especially the small pores (down to tens of nanometers), the porous samples were impregnated using different mixtures of epoxy embedding kit (Fluka no 45359) with acetone. The first impregnation was done in 3 volumes of acetone with 1 volume of epoxy, under mild vacuum (200 mbar) for 30 minutes. The following steps were successive changes in the mixture composition as 1:1 (acetone:resin), 1:3 and finally only epoxy [95]. The resin cure occurred for 24 hours at 60 °C. Samples were polished with diamond lapping films down to 0.1 μm, with water as cooling and lubrication medium.

Imaging conditions

Investigation on the microstructure with phase separation was carried out taking cross-section images at low acceleration voltage. Back-scattered electrons (BSE) could also be used to reach a chemical contrast and distinguish the phases present in the electrodes, but they need to reach a quite elevated minimum energy in order to be detected by the semiconductor BSE detector. Moreover, detector yield coefficients for nickel and YSZ in the anode are similar and high voltage and high current density must then be used to distinguish the phases [96]. Drawbacks of high voltage are: first, a lower resolution due to bigger interaction volume between electron and matter and then, difficulties to distinguish Ni and YSZ phases due to the equal back-scattered yield coefficient. Another consequence of using a high acceleration voltage is the charging of the sample, which is partially non-conductive because of the impregnation. For this reason, the samples are usually coated with conductive layers, such as carbon or gold; imaging with low acceleration voltage considerably limits the charging effects and permits to avoid the coating, thus permitting the investigation of the naked surface.

Secondary electron (SE) imaging at a low accelerating voltage of 1 kV was performed. These conditions gave a good contrast between Ni, YSZ and porosity in the anode and an acceptable contrast between LSM, YSZ and porosity in the cathode. Identical working distance (5 mm), magnification (2000x) and high beam current density (spot size 4 and 50 μm diaphragm) were fixed for the full batch of observations.

Chromium quantification

Chromium quantification was performed by EDXS with an EDS-analyzer coupled to the SEM, i. e. a silicon-drift detector from Oxford Instruments (UK) combined to Inca software. Detection and quantification of small quantities of Cr in LSM/YSZ cathodes by EDXS is not direct as Cr X-ray emission-lines are overlapping with La/Mn and O lines. In order to overcome this problem, images were taken at high acceleration voltage (30 kV) and then Cr was extracted using the relation (eq. 3.4) correlating the La Lβ2.5/Lα1 EDS

peak height ratio to Cr concentrations, as developed by J. A. Schuler in the CIME department of EPFL [97].

$$Cr\% = 16.24\frac{La_{L\beta2.15}}{La_{L\alpha1}} - 4 \tag{3.4}$$

Image processing

A Mathematica$^{®}$ code was developed in-house by A. Faes in the CIME department of EPFL using the add-on Digital Image Processing (Wolfram) to treat and analyze the original images and quantify phase proportions, average particle sizes and triple phase boundary (TPB) length [12].

Image treatment consists in converting the original gray-scale image to a three gray level map corresponding to the three phases (black for pores, gray for YSZ and white for Ni in the anode or LSM in the cathode). This is achieved by applying two thresholds to the gray level histogram of the original image to first obtain two binary images corresponding to the nickel (or LSM) and pore phases. Cleaning of the binary images (to remove isolated pixels) is then performed using morphological operations. These operations smooth irregular borders and fill in or remove isolated pixels and lines. After the cleaning, the recombination of the binary images will render the gray YSZ phase; Figure 3.13 shows, as an example, the SEM image of an anode taken from the cross section of a sample and the corresponding three-gray phase map of the YSZ-Ni composite.

Image analysis extracts quantitative microstructural information from the phase maps obtained from the pictures, such as volume fraction of the different phases, the average particle size of each phase, and the TPB density.
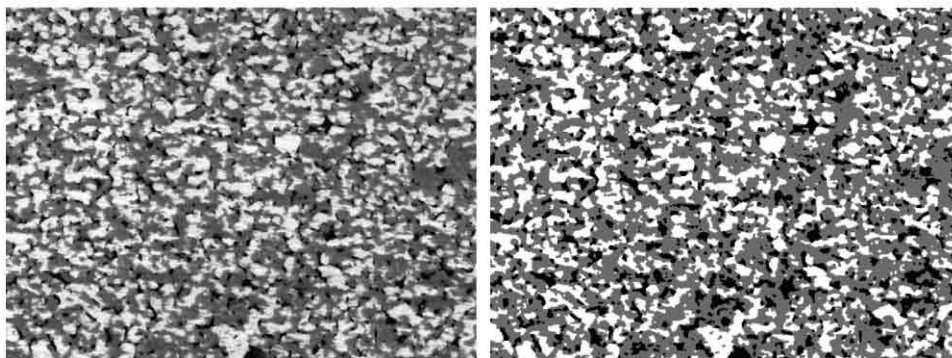
Figure 3.13. Left: SEM image obtained at low acceleration voltage on a Ni/YSZ anode cermet. Right: three-phase map obtained after image treatment

RESULTS AND DISCUSSION

Chapter 4

Degradation by morphological change

In this chapter, the percolation-based micromodel described in Section 2.2 is modified in order to take into account morphological variations in the electrode microstructure induced during operation. The inclusion into the model (proposed in [63]) of a time-dependent particle coarsening law permitted to convert a static model into a time-dependent model. This allows the prediction of performance loss during operation. The model is valid for both Ni/YSZ anodes and LSM/YSZ cathodes and, generally, for composite mixed ionic-electronic conductor electrodes; four different cases have been modelled.

Experimental validation has been performed (4.3). It has been demonstrated that it is possible to relate the experimentally measured cell degradation to the coarsening of Ni particles occurring in the anode, thus demonstrating the validity of the approach.

Results and modeling exposed in this chapter were published in the following paper:

- P. Tanasini, M. Cannarozzo, P. Costamagna, A. Faes, J. Van herle, A. Hessler-Wyser, and C. Comninellis. Experimental and theoretical investigation of degradation mechanisms by particle coarsening in SOFC electrodes. Fuel Cells, 9(5) :740-752, 2009.

4.1   Introduction

High temperature favors SOFC operation, since both the electronic conductivity of LSM and the ionic conductivity of YSZ increase exponentially with temperature and so does the catalytic activity of the electrodes. Nevertheless, high temperature operation also causes microstructural changes like densification and particle coarsening with the consequent decrease of triple phase boundary (TPB), possible loss of percolation and hindered diffusion, resulting in a decrease of the cell performance. This phenomenon is particularly evident in the anodes because of the sintering of Ni metal [11, 12, 13], but it has also been observed at high temperatures (900 − 1000 °C) for LSM [17].

The aim of this chapter is to individuate a correlation between the microstructural modification of the electrodes and the change in electrochemical performance. From a practical point of view, this permits to relate particle coarsening during operation with decay of performance of an experimental cell. In order to do so, a theoretical analysis has been carried out, starting from a detailed electrode micromodel based on percolation theory [63], described in Section 2.2. The morphological change in particle size has been described through suitable semi-empirical time-laws, which have then been included in the model itself. Such a transient model permits a quantitative prediction of the performance loss based on the knowledge of few fundamental physical parameters (particle sizes and their time dependence, phase conductivities etc.).

To validate the approach, four identical experimental SOFCs have been prepared and tested under identical operating conditions for different times. Galvanostatic operation of the cells has been conducted. After interruption of the operation, SEM analysis has been carried out on cross-sections of the samples, in order to individuate possible morphological modifications of the samples at different operating times. The observed changes in particle size have been used to evaluate the theoretical electrode degradation, which has been compared to the observed cell degradation.

4.2 Theoretical development

The model of composite electrodes described in Section 2.2 is a steady-state model, that can be equally applied to SOFC anodes and cathodes. The electrode is assumed to be an SOFC composite mixed ionic-electronic conductor electrode (Figure 2.1), made of a random mixture of spherical ionic and electronic conducting particles. The main phenomena occurring in an SOFC anode are charge transfer, mass transfer and the electrochemical reaction. The model is one-dimensional along the x-coordinate.

Charge transport, charge balance and electrochemical kinetics are represented by Eq. 2.27, 2.28. Ohm's law has been applied for the charge transport, for both the ionic and electronic species migrating along the clusters of ionic and electronic conducting particles, respectively.

Mass transfer of reactants and products is often not considered since, in the experimental conditions used for button cell testing (high gas flow rate, small electrode thickness, low fuel conversion), its effect on the electrode performance is considered negligible; indeed, in Section 2.2 it has been shown by simple estimation of the Thiele modulus that diffusion has low impact on the electrode performance and can usually be neglected. Furthermore, as all the electrical and electrochemical phenomena have characteristic times much faster than the times required for the growth of particles, those phenomena have been considered at steady-state at each simulation time during the transient simulation.

The model proposed in this work for the degradation of composite electrodes is based on Costamagna's steady-state percolation model, modified in order to take into account the increase of particle diameter with time. Time-laws for particle coarsening have been used to calculate the effective ionic and electronic resistivities, ρ^{eff}, and the active area for the electrochemical reaction (A). In this dynamic model both A and the percolation thresholds become time-dependent functions. Since the particles in the model are assimilated to spheres, the total volume of particles of one generic phase k at a given time can be calculated as

$$V_{k,(t)} = \frac{4}{3}\pi r_{k,(t)}^3 N_{k,(t)} \qquad (4.1)$$

where $V_{k,(t)}$ is the phase volume, $N_{k,(t)}$ the number of particles $r_{k,(t)}$ their radius at time t. Assuming the conservation of the total phase volume i.e. $V_{k,(t)} = V_k^0$, and indicating with the superscript ^{0} the value of the correspondent variable at $t = 0$, we obtain:

$$V_{k,(t)} = V_k^0 = \frac{4}{3}\pi \left(r_k^0\right)^3 N_k^0 \qquad (4.2)$$

From Eq. 4.1 4.2 the variation in the number of the particles is

$$N_{k,(t)} = N_k^0 \left(\frac{r_k^0}{r_{k,(t)}}\right)^3 \qquad (4.3)$$

In percolation theory, the information of particles dimension is better represented by the adimensional parameter $P = \frac{r_j}{r_k}$, the ratio between the particle radius of the two phases j and k, rather than the radii separately. Indeed, this parameter is used in Costamagna's steady-state model (Eq 2.13-2.15, 2.17) to calculate the geometric parameters of the microstructure. In our case, $P_{(t)} = \frac{r_{j,(t)}}{r_{k,(t)}}$ is the key parameter that, being a function of time, makes the model time-dependent.

It is important to note that in most practical cases, the dimension of the ionic conductor particles must be considered constant since coarsening is a phenomenon mainly observed for Ni in the anodes [11, 12, 13] and LSM in the cathodes [17]. In this case, Eq. 4.1-4.3 apply only to the electronic conductor phase.

4.2.1   Simulation of the electronic conductor phase coarsening

Case 1: Fixed maximum dimension for electronic conductor particles

The results obtained from the simulation of the coarsening of the electronic conductor phase in a composite electrode are reported. The particle size of the ionic conductor particles (or, equivalently, electrolyte particles) has been considered constant as well as the porosity - since the macroscopic volume of the electrode is preserved by the immobility

of the electrolyte backbone. The set of parameters necessary for the simulation contains typical values for SOFC anodes.

The variation with time of the dimensions of electronic conductor particles has been expressed as:

$$r_{el,(t)} = \left(r_{el}^{max} - r_{el}^0 \right) \left[1 - e^{(-t/\tau_s)} \right] + r_{el}^0 \qquad (4.4)$$

where el stands for electronic conductor phase, and io stands for ionic conductor phase. r_{el}^{max} is the maximum value allowed by the electrolyte backbone for the electronic conductor phase, at $t = \infty$; τ_s is the characteristic time for the coarsening process.

Consequently, it is found:

$$P_{(t)} = \frac{\left(r_{el}^{max} - r_{el}^0 \right) \left[1 - e^{(-t/\tau_s)} \right] + r_{el}^0}{r_{io}} \qquad (4.5)$$

Such a relationship is a form of a limited exponential growth that has been experimentally found by Faes and coworkers [12] for Ni particle growth in SOFC anodes. It has been called "charging capacitor" model because of the mathematical correspondence between the two phenomena. Eq. 4.4 shows a plateau, which is thought to be related to the presence of the YSZ network blocking an indefinite growth of Ni particles, as confirmed by experimental data in [12, 98].

Figure 4.1 presents the evolution of the parameter P with time, increasing as a consequence of the increase of the electronic conductor particle size until reaching a constant value.

P is used to evaluate the active area for the electrochemical reaction, and the value of the compositions corresponding to electronic and ionic percolation thresholds. In particular, since in the study of a binary and random mixture of two types of spheres illustrated in Section 2.2, the number of contacts of each particle with particles of the same type is function of the ratio of the dimension of the two types of spheres. In other words, if the dimension of the electronic conductor particles increases and the overall volumetric fraction occupied remains constant, and if the dimension of the electrolyte particles remains
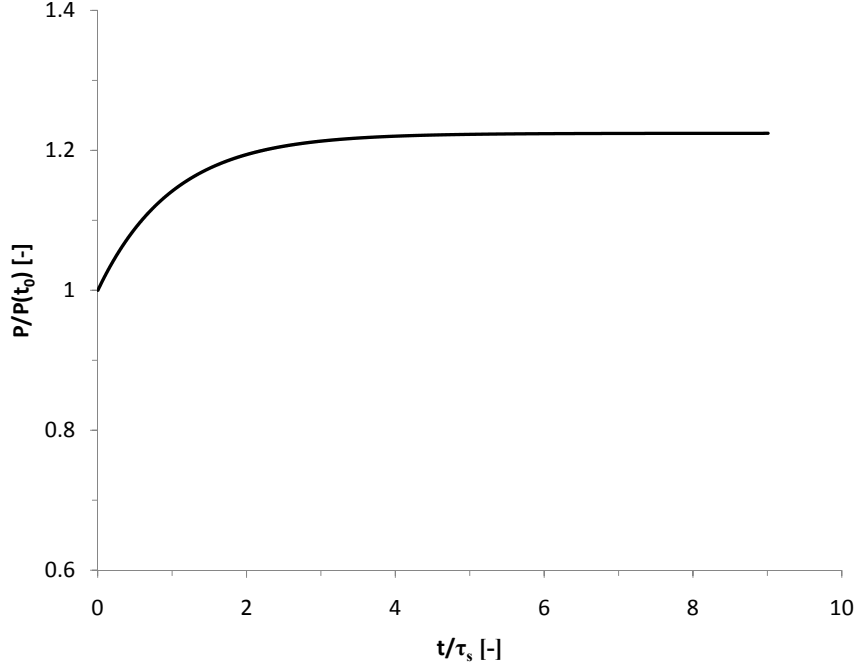
Figure 4.1. Temporal evolution of P with respect to its initial value from Eq- 4.5 during the coarsening of the electronic conductor phase. The time scale has been normalized through τ_s, the characteristic time for the coarsening process.

constant as well, then the number of electronic conductor particles becomes smaller and also each particle is surrounded by a smaller number of particles of the same type.

As the percolation thresholds are strongly influenced by the value of P which is a function of time, Figure 4.2 reports the variation of the percolation thresholds with time: the percolation thresholds shift to a bigger amount of electronic conductor during time as a consequence of the decrease of the size ratio P .

As already shown in Section 2.2, the active area is affected by two different phenomena tied to characteristics of the microstructure, namely

- a *geometric* factor: the particle size for a given composition determines the density of electronic conductor-electrolyte active sites per unit volume. The smaller the particle size, the bigger the number of particles in the unit volume and therefore of
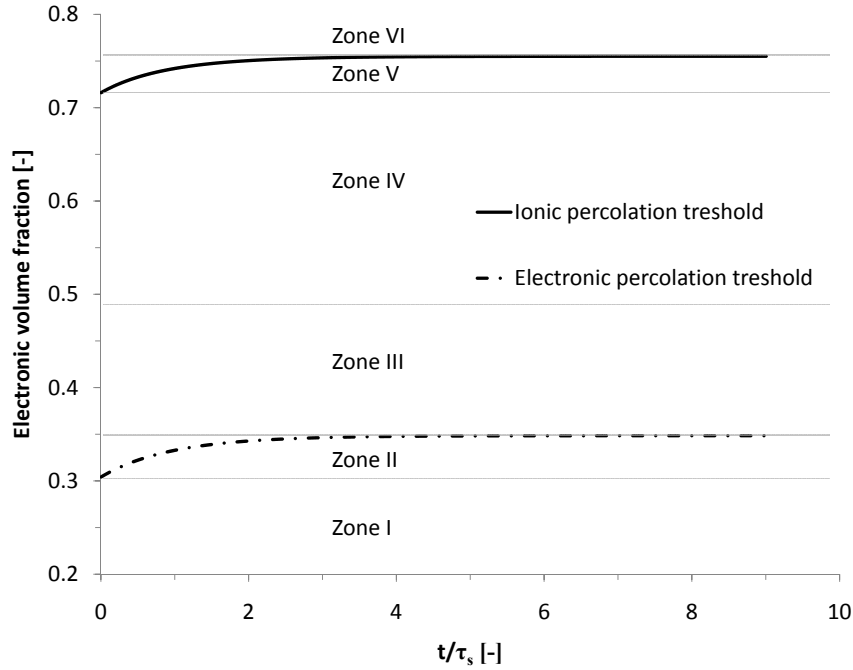
Figure 4.2. Temporal evolution of the percolation thresholds during the coarsening of the electronic conductor phase. The time scale has been normalized through τ_s, the characteristic time for the coarsening process. Composition zones with different behavior during coarsening have been indicated.

active sites;

- a *topological* factor: a composition that is far from both percolation thresholds has a high probability that a given active site belongs to both the electronic and ionic conductive networks. In other words, the particle size and the electrode composition do not affect only the absolute value of the TPB extension but, influencing the interconnectiveness of the particles, determine the probability that a specific TPB point belongs or not to both the electronic and ionic percolation network, making it electrochemically active.

Coarsening obviously always affects negatively the first factor due to the fact that electronic conductor particles increase their dimensions over time, exposing smaller and smaller

external surface, and thus the contact area with the electrolyte particles decreases as well. The second point, however, is more complex and a number of possible evolutions exist for an electrode during electronic conductor coarsening. Different behaviors are predicted by the theory, depending on the initial composition; the composition zones characterized by a behavior are indicated in Figure 4.2:

- zone I, there is no percolation of the electronic conductor phase at the beginning, and there will not be at any time;

- zone II, the initial microstructure has a percolating network of electronic conductor particles but the percolation threshold moves, eventually reaching and passing the electrode composition. In this case, there is loss of percolation and catastrophic loss of performances as soon as the percolation threshold reaches the electrode composition;

- zone III, the electrode composition is well inside the percolation window for all the operating times, and the electrode performance decreases during time;

- zone IV, the electrode is well inside the percolation window for all the operating times, and the electrode performance increases during time. To explain this effect, which might seem odd at a first glance, we must take into account that electrolyte particles are surrounded and isolated by electronic conductor particles, so that the probability of having non-active electrolyte particles is high. As time goes by, the increase in the dimensions of the electronic conductor particles, on one hand, hampers the connectivity of the electronic conductor clusters but with negligible negative effect - since the network is very dense and well connected in any case. On the other hand, there is a beneficial effect on the connectivity of the electrolyte clusters (and in fact the percolation threshold of electrolyte moves towards lower contents of electrolyte). A parallel benefit of the improvement of the connectivity of the electrolyte clusters is their increase in ionic conductivity; the fact that we are in a low perfor-

mance region, where the ionic conductivity of the electrolyte clusters is a dominant effect, explains the increase of performance over time in this region;

- zone V, the initial performance of the electrode is practically the same as that of an electrode entirely composed of electronic conductor particles, with no extension of the reaction zone inside the electrode thickness. At a certain operating time, a sort of activation occurs with formation of spanning electrolyte clusters and extension of the reaction zone throughout the electrode thickness;

- zone VI, the performance of the electrode is practically the same as that of an electrode entirely composed of electronic conductor particles, with no extension of the reaction zone inside the electrode thickness.

In the cases IV and V the topological effect, through an increase of the interconnectiveness of the electrolyte phase dominates over the absolute density of active sites and has a positive effect, enhancing the performances with time. The increase of connectivity of the electrolyte phase is predicted despite the fact that this phase is considered not to undergo morphological variation during time. It is indeed an indirect effect of the coarsening of the electronic conductor phase that can be physically explained as follows: during coarsening fewer, bigger electronic conductor particles are formed, and the redistribution of matter reduces the number of "barriers" between ionic conductor particles, therefore increasing their connectiveness.

Figure 4.3 shows the simulated electrode performance as a function of time for several electronic conductor compositions; the performance it is here represented as the reciprocal ASR (area specific resistance), of the electrode under operation, that means the reciprocal overall electrode resistance per unit area. For the calculations it has been considered that the conductivity is higher for the electronic conductor than for the ionic. The electrodes containing a low content of electronic conductor give the best performance at early operating times, because of the higher conductivity of electronic conductor. In effect, this is the case for both Ni and LSM, but for Ni the difference is much more important and this is the cause of the choice for technological electrodes. In effect, common compositions
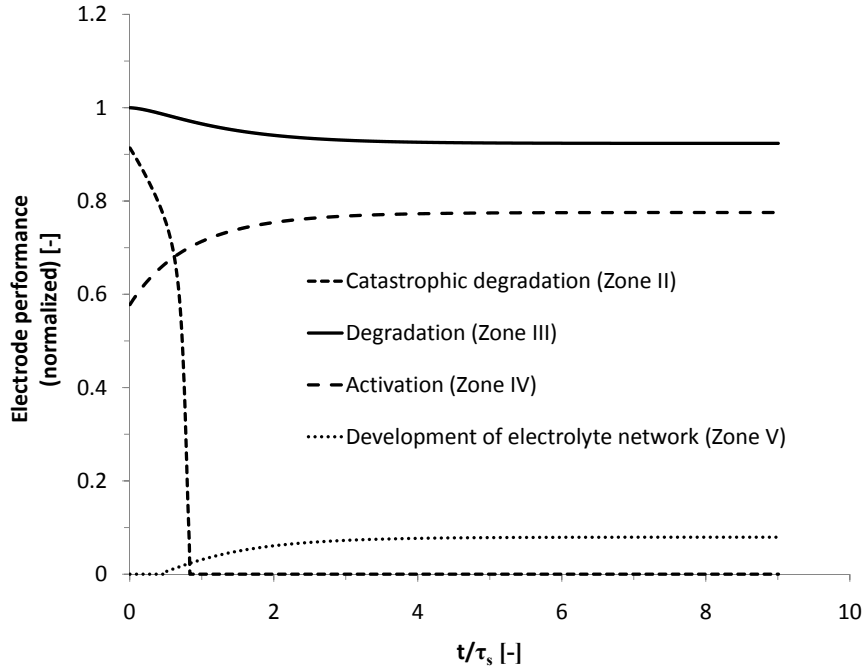
Figure 4.3. Temporal evolution of the electrode performance during the coarsening of the electronic conductor phase. Values have been normalized with respect to the maximum value obtained. The time scale has been normalized through τ_s, the characteristic time for the coarsening process.

for commercial electrodes have a Ni content very close to the Ni percolation threshold, since for anodes the minimum Ni content gives the densest ionic network, maximizing its conductivity - which is by far the most limiting factor [99, 63]. It is interesting to note that, in agreement with the analysis made for Figure 4.2, compositions near the electronic conductor percolation threshold undergo serious deterioration. On the contrary, the electrodes containing high electronic conductor content (above 50%) improve their behavior during time and display satisfactory performance after the coarsening has happened.

Figure 4.4 shows the evolution of the geometric TPB density for the different cases already examined in Figure 4.3; as it was expected, the best performance is not given by the compositions with the highest TPB density. This is due to the fact, already mentioned, that the conductivity of the electrolyte network is limiting; therefore, the

best performances are found at high ionic conductor contents, where the probability of dead clusters of electrolyte is minimal. However, in all cases there is a decrease of the geometric TPB density during coarsening. Figure 4.5 completes the picture, showing the evolution of the active area (which is the sum of the contacts between particles of Ni and YSZ, both topologically connected to the corresponding percolating cluster) for different times as a function of the initial electrode composition. Again, the behavior zones have been indicated. The active area obviously becomes zero at the percolation thresholds, and it displays a maximum for a composition between the two percolation thresholds. It is clear form this graphic that, even if the geometric TPB density is generally reduced by coarsening, near the steep edge at high electronic conductor fraction, the lateral displacement caused by the topological increase of interconnectiveness can cause an increase of the active area.

Case 2: Maximum dimension for electronic conductor particles as a function of the electrode composition

It must be noted that all the simulations done in the previous Section have been performed with the same growth law, i.e. Eq. 4.4. On the contrary, the upper limit for electronic conductor particle size is itself, intuitively, a function of the electrode composition: at low electrolyte contents the electrolyte backbone becomes loose and its retaining effect should be less effective. If we introduce such a dependence, then the final particle dimension r_{el}^{max} becomes a function of the initial electrode composition.

More precisely, we can assume that the hindering capability of the zirconia backbone towards coarsening is related to the average number of contacts an electronic conductor particle has with electrolyte particles. Eq. 2.13, 2.14, 2.16 permit to calculate the average coordination number of particles of the electronic conductor phase Z_{el} and the electrolyte phase Z_{io}.

Ideally the coarsening of electronic conducting particles is completely hindered when $Z_{el-io} \rightarrow Z_{el}$, meaning that each electronic conductor particle is mainly surrounded by electrolyte particles. On the other hand, $Z_{el-io} = 0$ means that each electronic conducting

Figure 4.4. Temporal evolution of the geometric TPB area during the coarsening of the electronic conductor phase. Values have been normalized with respect to the initial value of the "Degradation (Zone III)" curve. The time scale has been normalized through τ_s, the characteristic time for the coarsening process.

particles is in contact only with other particles of the same phase, so that there is no hindering effect at all and the coarsening can continue indefinitely.

We can assume a generic relation between these parameters, respecting the conditions described above:

$$r_{el(\varphi_{el}^0)}^{max} = r_{el}^0 \left(\frac{Z_{el(\varphi_{el}^0)}}{Z_{el-io(\varphi_{el}^0)}} \right)^{\xi} \tag{4.6}$$

Where ξ is an adjustable parameter of the model; the value of ξ has been calculated from the data contained in [98], and has been found equal to $\frac{1}{2}$. It is clear from Eq. 4.6 that $r_{el(\varphi_{el}^0)}^{max}$ goes to infinite values if $Z_{el-io} = 0$, while it remains equal to the initial value r_{el}^0 if $Z_{el-io} = Z_{el}$.
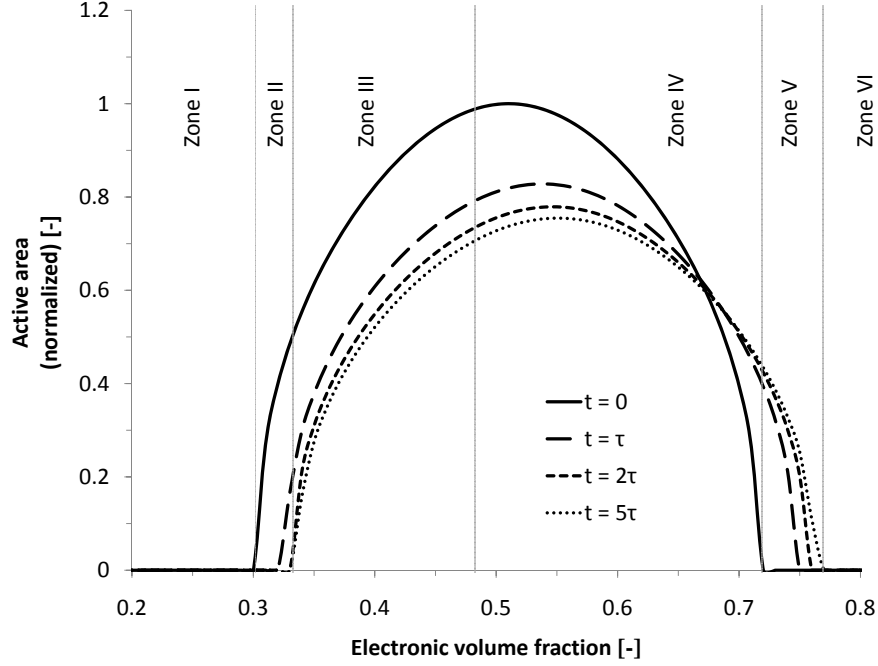
Figure 4.5. Temporal evolution of the active area as a function of the electrode composition (electronic volume fraction) during the coarsening of the electronic conductor phase. Values have been normalized with respect to the highest value obtained. The curves have been calculated at different multiples of τ_s, the characteristic time for the coarsening process.

Substituting Eq. 4.6 in Eq. 4.4, we develop the relationship

$$r_{el,(t,\varphi_{el}^0)} = r_{el}^0 \left\{ \left[\left(\frac{Z_{el(\varphi_{el}^0)}}{Z_{el-io(\varphi_{el}^0)}} \right)^{\frac{1}{2}} - 1 \right] \left[1 - e^{(-t/\tau_s)} \right] + 1 \right\} \tag{4.7}$$

Eq. 4.7 has been used for simulations and the results are shown in Figure 4.6, compared to those obtained with Eq. 4.4. As it can be observed, the general behavior is the same.

However, it is clear that for low electronic conductor compositions most of the particles around each particle of electric conductor are part of the electrolyte backbone. In this case, the coarsening is somehow hindered, and the negative effects diminished, as it is the case for compositions in the zone II, i.e. having catastrophic degradation. In practice, this effect gives some additional robustness to electrodes that, like commercial Ni/YSZ anodes,
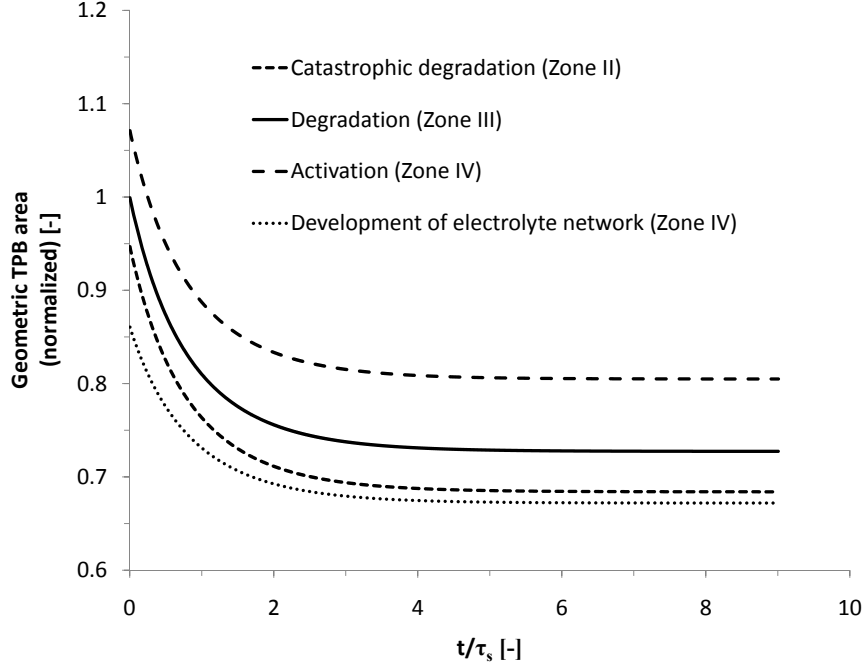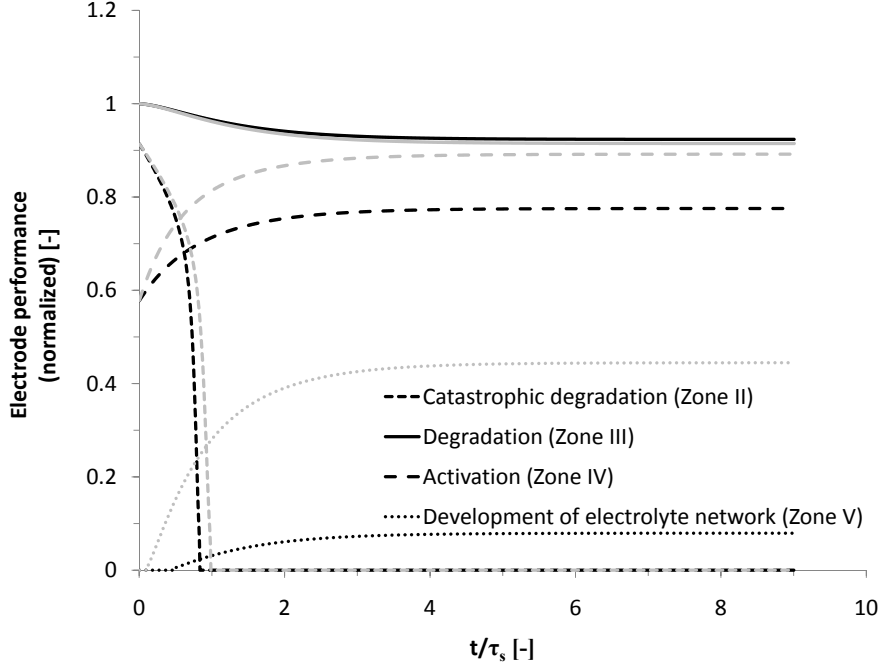
Figure 4.6. Temporal evolution of the electrode performance during the coarsening of the electronic conductor phase. Values have been normalized with respect to the maximum value obtained. The time scale has been normalized through τ_s, the characteristic time for the coarsening process. Black lines stand for calculations using Eq. 4.4, while gray lines stand for calculations made with Eq. 4.7, which takes in account the effect of the electrolyte backbone on the coarsening process.

contain a very low amount of electronic conductor, close to the percolation threshold. In effect, while coarsening tends to break the percolating network of Ni particles, the additional high amount of YSZ hinders the coarsening itself, limiting the maximum value that can be reached by the Ni particles.

On the opposite case, low fractions of ionic conductor leave place to an increased coarsening process, exaggerating the effects of the change in particle size. In the case presented in Figure 4.6, this increases both the degradation of an electrode belonging to zone III and the beneficial effect for electrodes belonging to zones IV and V.

4.2.2 Simulation of both ionic and electronic conductor phases coarsening

Case 3: Constant porosity

The results obtained from the simulation of the coarsening of both phases in a composite electrode are reported. The set of parameters necessary for the simulation contains typical values for SOFC cathodes. The coarsening of the electronic conductor phase has been expressed with Eq. 4.7, while the electrolyte phase, generally more insensitive to coarsening at typical operation temperatures of SOFC, has been expressed with Eq. 4.4, and considering $r_{io}^{max} = 1.2 r_{io}^0$. The time constant for the coarsening has been considered the same for both phases, assuming that the coarsening of each phase would somehow influence the other's, and the attainment of the equilibrium would mean the stabilization of both phases.

Figure 4.7 presents the evolution of the parameter P with time for different compositions; it is generally increasing as a consequence of the increase of the electronic conductor particle, apart for compositions rich in electrolyte. In that case, the relative increase of the size of electrolyte particle is bigger, and P decreases slightly.

The evolution of the electrode performance during coarsening is presented in Figure 4.8. In several cases the behavior is similar to that presented in Figure 4.3. However, the different trend obtained for P in the electrodes with low content of electronic conductor brings an enlargement of the percolation thresholds in this region, as it is observed at high electrolyte contents for both Figure 4.8 and 4.3. In effect, Equation 4.7 predicts a quite small variation in diameter for electronic conductor particles when their volume fraction is low; the coarsening of electrolyte particles, on the other hand, indirectly causes the development of new contacts between the sparse electronic conductor particles, giving rise to a percolating network after some time of operation. So, for the case described, there is no possibility of catastrophic degradation since electrodes belonging to compositions of zone II have a beneficial effect from coarsening instead of being pushed out of the electronic percolation threshold.
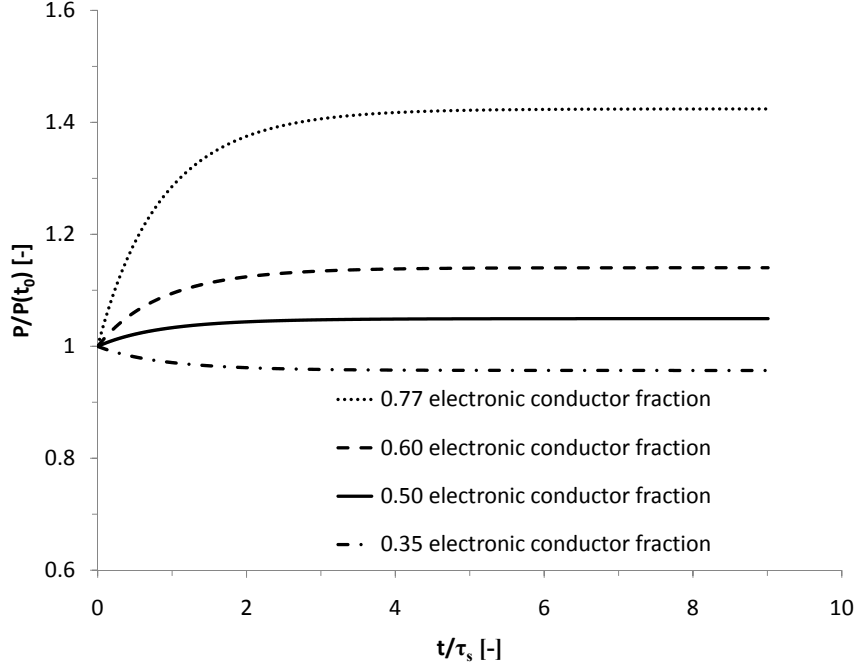
Figure 4.7. Temporal evolution of the P with respect to its initial value during the coarsening of both phases. The time scale has been normalized through τ_s, the characteristic time for the coarsening process.

As already mentioned, the simulations have been run with values typical for LSM/YSZ SOFC cathodes; in these conditions, the maximum performance is found for compositions slightly enriched in electrolyte, because the LSM is more conductive than YSZ. Still, the difference in conductivity is much smaller than the one existing between Ni and YSZ and the optimal composition is expected to be not far from 50% in volume of each phase commonly used for commercial electrodes[63]; in effect, as shown in Figure 4.9, a composition of around 45% of electronic conductor phase brings the optimal performance. It is interesting to see that the optimal composition gives the best performance both before and after coarsening. However, the degradation is heavier on the best electrode with respect to the standard 50% composition and this despite the fact that the coarsening of the electronic conductor is smaller for the former, according to Eq. 4.7. In effect, performance
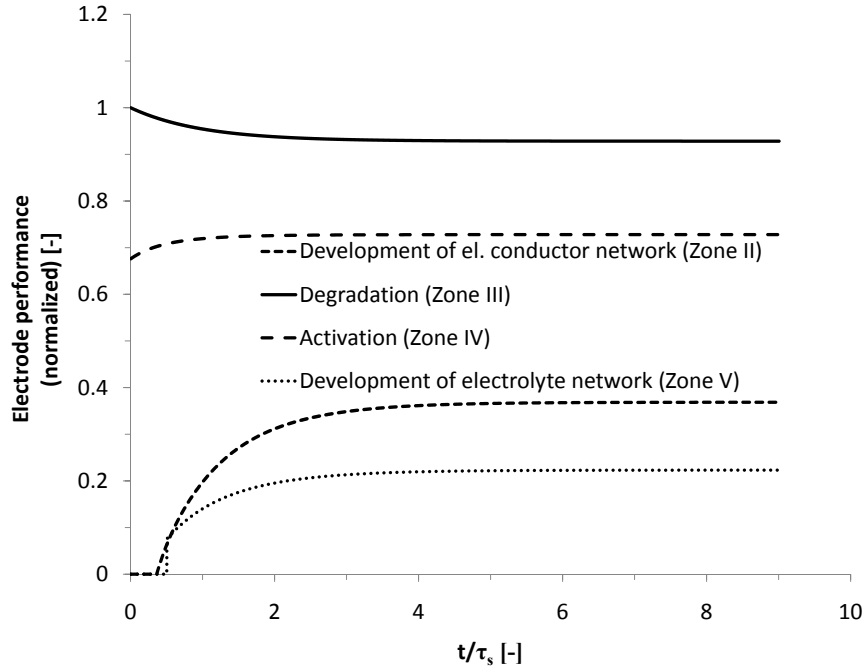
Figure 4.8. Temporal evolution of the electrode performance during the coarsening of both phases. Values have been normalized with respect to the maximum value obtained. The time scale has been normalized through τ_s, the characteristic time for the coarsening process.

loss from the beginning to the point at which the coarsening is complete is 7.2% for the 50% composition and 9.3% for the electrode with the optimal performance.

In order to explain this phenomenon, it is necessary to examine Figure 4.10, reporting the electrode performance as a function of the electrode composition at several coarsening times. Several observations are possible. First of all, it is evident the effect of the composition on the coarsening process: the bell-shaped curve enlarges at both sides while time passes, as it was expected after the analysis of Figure 4.8. As a second remark, it is visible the asymmetry of the curve, caused by the difference in conductivity between the two phases. Finally, from this figure it is graphically evident the reason for which the optimal composition undergoes the highest loss performance: the coarsening process causes the shift from one curve to another where the gradient is the largest. This is explained by the
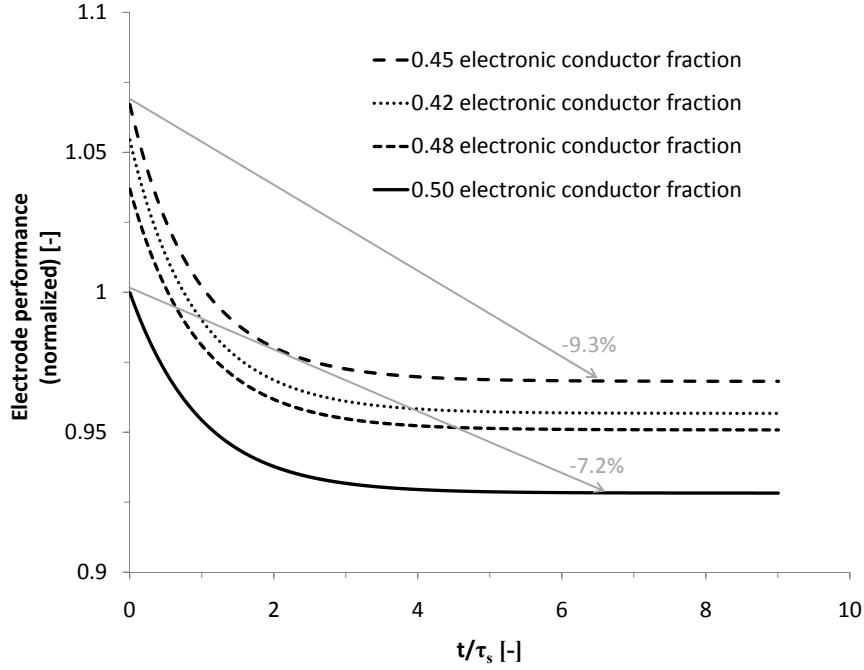
Figure 4.9. Temporal evolution of the electrode performance during the coarsening of both phases near optimal composition. Values have been normalized with respect to the initial value obtained for 0.5 electronic conductor fraction. The time scale has been normalized through τ_s, the characteristic time for the coarsening process.

fact that in the central part of the curve, far from percolation thresholds, the statistical effects are negligible and the limiting factor is the extension of the geometric TPB area and the difference in conductivity between the two phases; coarsening has a bigger impact on the compositions with optimal trade-off between TPB area and relative conductivity of the percolating networks.

As a final remark, the reason for the fact that the composition-dependent coarsening according to Eq. 4.7, does not favor the electrode richer in electrolyte phase is that the difference between the two cases analyzed is negligible: there is only 3% variation in the value of $r_{el(\varphi_{el}^0)}^{max}$ reached after the coarsening is complete.

In any case, it is evident from this last graph that there is no possibility for inversions, that is, that the electrode with optimal performance, although undergoing a more severe
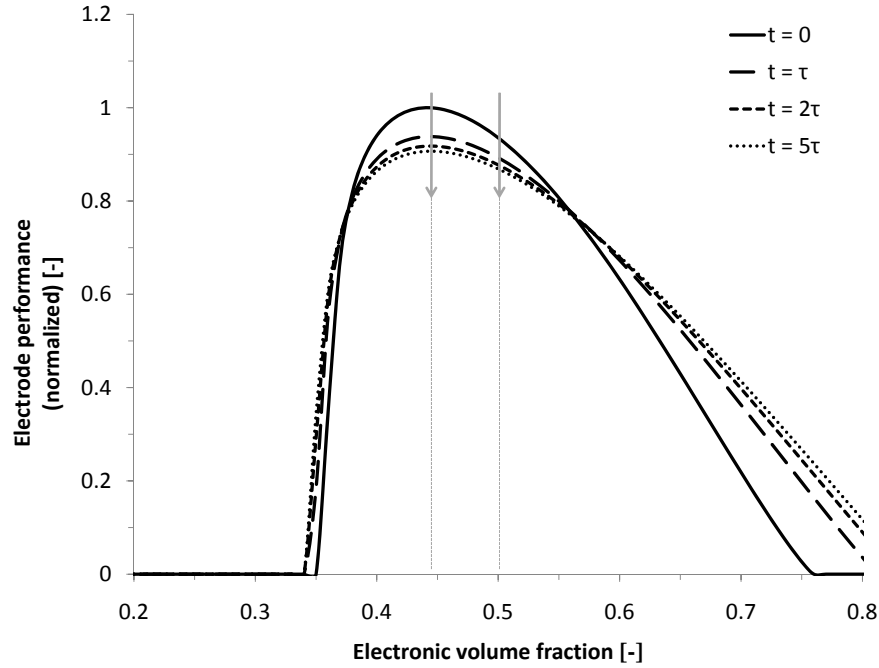
Figure 4.10. Temporal evolution of the electrode performance as a function of the electrode composition during the coarsening of both phases. Values have been normalized with respect to the highest value obtained. The curves have been calculated at different multiples of τ_s, the characteristic time for the coarsening process.

degradation, remains the most efficient after the coarsening is complete.

Case 4: Variable porosity

While both phases have an increase in particle dimension, it is likely that the electrode undergoes a sintering process, i.e. a densification and therefore a change in porosity. This was not the case for section 4.2.1, because the electrolyte backbone acts as a supporting medium for the electrode while the electronic conductor phase coarsens, like it has been observed for SOFC anodes [12, 98]. The situation is somewhat different if both phases coarsen - which can likely be the case for SOFC cathodes, especially if the initial microstructure is very fine and the operating conditions harsh and close to the sintering temperature.

The change in porosity can give rise to different situations: in effect the number of particles per unit volume is a function of the porosity and their average dimensions. The coarsening brings to a general decrease of the number of particles in the electrode, for instance by coalescence of the smaller particles (see Fig. 4.11 A). If one of the phases stands still, as it was the case considered in Section 4.2.1, the coarsening can be considered as a redistribution of voids and material of the coalescing phase in the space. Obviously, the total amount of each phase in a certain control volume is conserved, and an increase in the average dimensions of one phase means that less particle will be present in that control volume. Also, average size of pores is expected to increase, but not the total porosity. A decrease in porosity goes in the opposite direction: it is clear from Figure 4.11 B that a densification process brings new particles from outside through the borders of the control volume. This effect can compensate or even overcome the previous, depending on the change in porosity that is considered.

A decrease of porosity can be introduced in the model and simulated numerically; an exponential form similar to Eq. 4.4 has been chosen; the decreasing trend is mathematically correspondent to the equation relative to a discharging capacitor:

$$\varepsilon_{(t)} = \left(\varepsilon^0 - \varepsilon^{min}\right) e^{(-t/\tau_s)} + \varepsilon^{min} \tag{4.8}$$

The value for τ_s was fixed equal to the one for the coarsening process. In Figure 4.12 is shown the evolution of the performance of the electrode for different ratios $r = \varepsilon^{min}/\varepsilon^0$; the conditions for simulation are otherwise the same used in Section 4.2.2.

In Section 4.2.2, for the studied case, the total number of particles in the electrode was almost halved down during the coarsening process, causing a net and important decrease of the active area; this is the case reported in Figure 4.12 for $r = 1$. While imposing higher densification, the decrease in particles per unit volume is compensated from one side to the reduction of void spaces; on the other side, each single contact between two particles increase in size, since it is considered proportional to the particle diameter in the model. As a consequence of these two combined effects, in particular the former, the loss in active
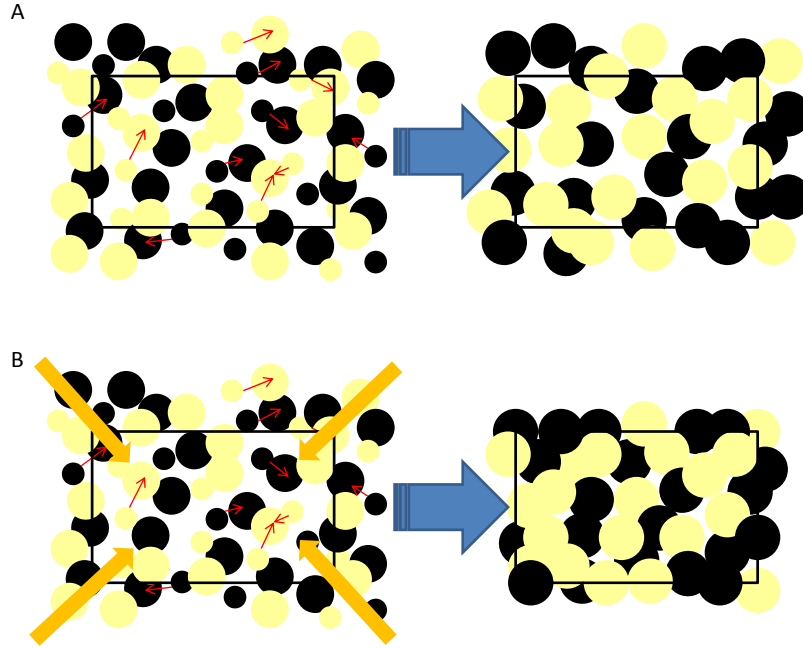
Figure 4.11. Schematic representation of different coarsening processes. A) Constant porosity: the total amount of each phase in the control volume is conserved. B) Variable porosity: new particles are brought through the border of the control volume while the porosity decreases.

area is reduced with decreasing r, and from a certain point it may even increase.

Figure 4.13 shows the evolution of active area for the cases presented in Figure 4.12; it is evident that the "turning point" is around $r = 0.66$, where the densification compensates exactly the coarsening effect, and the active area remains constant. It is interesting to observe comparing the two figures, that the iso-performance curve and the iso-active area curve are found at a slightly different r. This is because in this situation the topological effect tied to the improvement of the ionic conducting percolating network becomes visible again: this contribution is small and negligible as long as there is a considerable variation of the geometric and active area, as seen in Section 4.2.2. But in the situation currently analyzed, the value of r ensures that the active area is maintained constant so that the coarsening of the electronic conductor phase, comparatively bigger than the one of the

Figure 4.12. Temporal evolution of the electrode performance during the coarsening of both phases and densification. r represents the ratio between final and initial porosity $\varepsilon^{min}/\varepsilon^0$. Values have been normalized with respect to the initial value. The time scale has been normalized through τ_s, the characteristic time for the coarsening process.

electrolyte phase, brings to an indirect improvement of the ionic percolating network and therefore to a gain in performance. Of course, since topological effects are limited for intermediate compositions, the performance improvement is small.

A last remark has to be made concerning the case $r = 0$ and, generally speaking, for severe densification: the expected increase in performance shown in Figure 4.12 is unrealistic since it does not take into account the hindered diffusion for gaseous oxygen that must reach the TPB active sites through pores. Indeed, very dense cathodes would suffer limitations due to insufficient mass transfer inside the cathode layer, and this is especially true for repeat elements or real stacks that have to deal also with progressive conversion along the flow. However, the assumption to have no limiting oxygen diffusion is reasonable for most of technological SOFC cathode layers, which are relatively thin (few
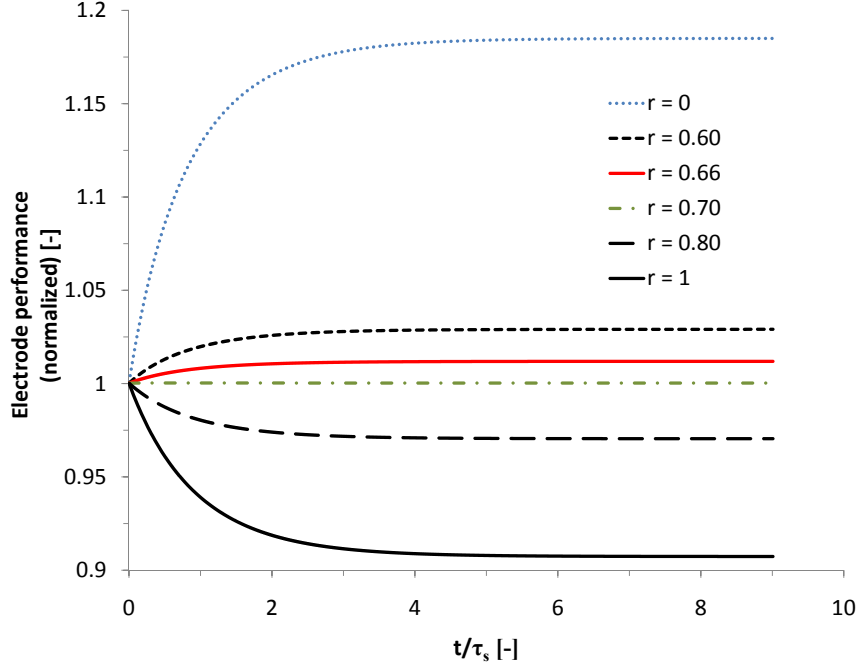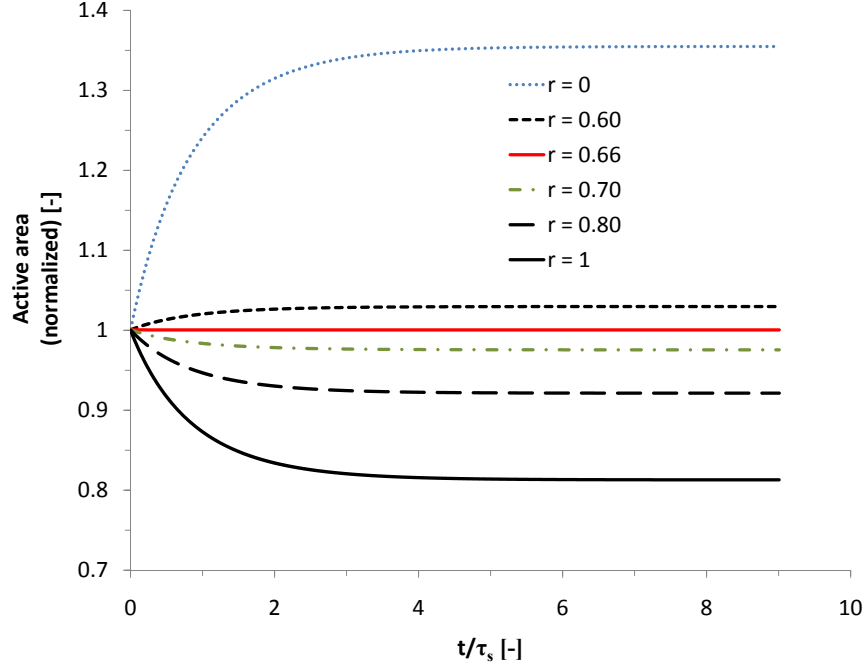
Figure 4.13. Temporal evolution of the active area during the coarsening of both phases and densification. r represents the ratio between final and initial porosity $\varepsilon^{min}/\varepsilon^0$. Values have been normalized with respect to the initial value. The time scale has been normalized through τ_s, the characteristic time for the coarsening process.

tenths of micrometers) and porous (30% to 40% relative porosity) and it is unlikely that a coarsening during operation would modify the microstructure so deeply to make this phenomenon a relevant factor.

The location of the optimal porosity to have the better trade-off between the extension of active area and the oxygen mass transfer would be more properly the objective of the optimization of the sintering process for the preparation of the cathode layer. Special care should be taken studying this subject, since the depletion of oxygen near the electrode-dense electrolyte layer influences the performances but also the durability of the cells, promoting the formation of undesired insulating phases [44].

4.3   Experimental validation of the proposed model

The objective of this series of experiments was to operate cells under the same conditions and to stop the tests after different operation times in order to carry out the microscopic investigation and take a snapshot of the microstructure of each cell. In particular, a very interesting quantitative value that could be extracted was the average particle size of each phase during time. In this way, as it will be further discussed, it was possible to run the electrode micromodel feeding it with the coarsening time laws found experimentally in order to evaluate the electrode overall loss predicted by the model and obtain, for each operating time, a theoretical value related to the microstructure observed.

Temporal evolution of cell potential

All cells were tested at 850℃ and polarized with a total current of 0.6 A, about 0.5 A/cm^2. A typical value of the cell potential measured during the aging on the cell at constant current density is shown in Figure 4.14. After polarization, the cells present an activation period that is almost complete in about 24 h; the same kind of activation has been reported by several authors [100, 101, 102, 103, 104, 105] and seems to be related to the dissolution of non-conductive phases formed during sintering or cationic migration to the surface of the LSM. Follows a period of about 200 h in which the potential difference is constant and no noticeable degradation occurs. In the case of the longest test, it can be observed that a strong degradation appears after the plateau; the same behavior has been observed in other long-term tests performed in our laboratory.

Four cells were tested for different operation times: 0 h (only reduction), 24 h, 200 h and 1000 h; they will be referred to as cell A, B, C and D respectively. The choice has been made in order to investigate some significant evolution of the potential value: the cell B has been operated for the time needed to have an almost complete activation, while cell D has been taken as a long-term operation and cell C as an intermediate time at which degradation just begins to occur. Even if the cells were produced and tested in nominally identical conditions, the absolute value of the operating potential had a dispersion; this is
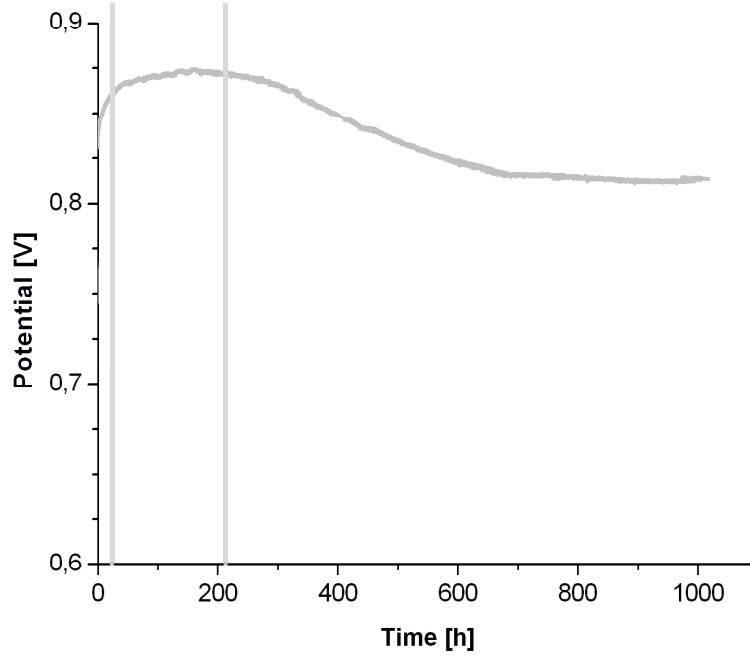
Figure 4.14. Temporal evolution of potential of cell D operated at constant current density (about 0.5 A/cm^2) at 850°C for 1000 h. The vertical lines mark the times at which the operation was stopped for cell B (24h) and cell C (200h). Cell A was only reduced, and extracted at 0 h.

a consequence of the experimental error on the area during deposition of the cathode layer and of the fact that all the cells have been operated at the same overall current of 0.6 A. Thus, since the different cells operate at current densities that are not exactly identical, the voltages also show dispersion. However, the trend during time is the same for all the cells, and this is the most important aspect from the point of view of the modelling analysis.

Morphological analysis of the cathode

Five images were analyzed for the cathode of cell A (0 h of operation) in order to determine the reproducibility of the measurements and the dispersion obtained was around 10%. In Figure 4.15, an image of the cross-section and the corresponding three-phase map of the

Phase volume fraction [%]

	Cell A	Cell B	Cell C	Cell D	average	solid volume fraction
Pore	44	43	42	42	42.5	-
YSZ	29	28	30	30	29.1	50.6
LSM	28	28	29	29	28.4	49.4

Particle size [μm]

	Cell A	Cell B	Cell C	Cell D
Pore	0.47 ± 0.05	0.44 ± 0.04	0.42 ± 0.04	0.44 ± 0.04
YSZ	0.33 ± 0.03	0.31 ± 0.03	0.32 ± 0.03	0.33 ± 0.03
LSM	0.45 ± 0.04	0.40 ± 0.04	0.40 ± 0.04	0.45 ± 0.04

Table 4.1. Results of image analysis for the cathodes of the cells

cathode layer are shown. One image per cathode was then treated and analyzed in the case of the other cells; Table 4.1 presents the results of the image analysis carried out on the cathodes (with ±10% error imposed on all values). For all the samples investigated, the volume fraction occupied by the pores has been found to vary between 41% and 44% depending on the sample; these values fall within the error of the method. The solid part of the cathode is occupied by LSM and YSZ with a proportion that has been to be close to 1:1 in volume, as expected from the theoretical composition (since LSM and YSZ were 50% in volume in the ink). An interesting point is that all the volume fractions (voids, LSM and YSZ) remain practically constant for all the samples tested for different times, indicating that there was no noticeable densification of the electrode during operation under the condition and times investigated. Overall, we could not find any noticeable variation of the cathode microstructure in the conditions that have been tested. Of course, this analysis does not exclude the possibility that other phenomena independent of a change in microstructure can intervene in the cathode, leading to the activation process or contributing to the degradation.
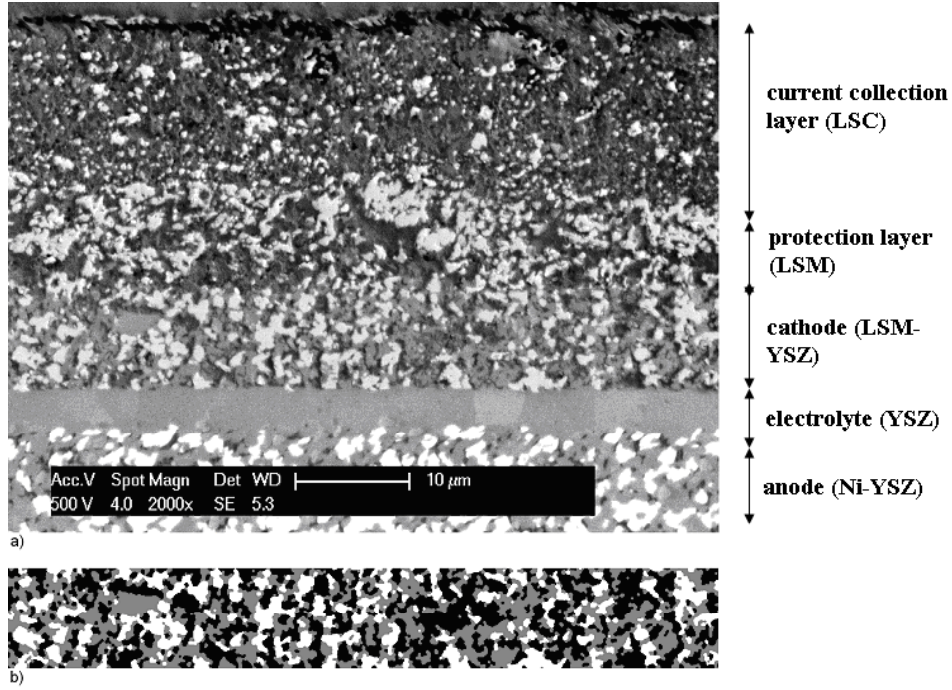
Figure 4.15. A) Cross-section of a cell and B) corresponding three-phase map of the cathode layer, obtained after image treatment.

Morphological analysis of the anode

Five images were analyzed for the anode of cell A, two for cell B and four for cells C and D; the dispersion obtained was less than 3% for cells A, C and D and 5% for cell B. In Figure 4.16, an image of the cross-section and the corresponding three-phase map of the anode support are shown. Table 4.2 presents the results of the image analysis. For all the samples investigated, the measured volume of the pores represented about 15% of the anode; the volume fraction occupied by the Ni accounted for about 30% while the YSZ represented around 55% of the volume. The values have been found to be constant for all the samples, indicating that, as it has been already observed in the cathode, there was no noticeable densification of the electrode or Ni evaporation during operation. With respect to the solid phase only, the Ni fraction was around 35% v/v, which is close to the theoretical percolation threshold, which has been calculated to be about 30% at the
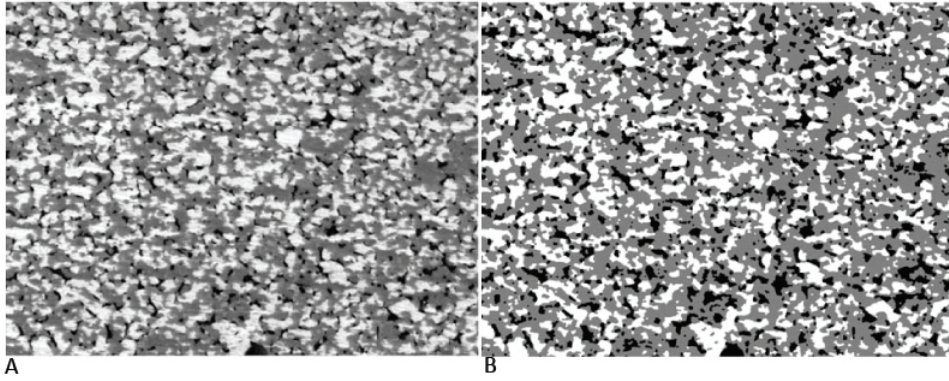
Figure 4.16. A) Cross-section of an anode support and B) corresponding three-phase map, obtained after image treatment.

starting time. This composition is the one expected to provide the best performance at starting time, due to the much higher conductivity of Ni with respect to YSZ [99, 63]. From the data reported in the Table 4.2, it appears that Ni particles did change the average size with the time passing under operation, while the dimensions of the YSZ particles were substantially unchanged. This phenomenon has been reported and already recognized as a source of degradation of the anode, and it is caused by the operation temperature close to the melting point of Ni (1450 °C) and the surface tension between Ni and YSZ. The size of Ni particles displayed the biggest change in morphology during the first part of the operation (Figure 4.17). We have reported the experimental data in Figure 4.17 fitted through the least squares method with Eq. 4.4 and Eq. 4.7; the value of $\frac{1}{2}$ used for ξ in Section 4.2.1 has been found from this data; τ_s has been found equal to 444 h.

By comparing Figure 4.17 to Figure 4.14, we can make two remarks:

- There seems to be no correlation between the initial activation of the cell (in the first 24 h) and morphological variations occurring in the electrodes, since neither the anode nor the cathode exhibits any noticeable change in this range of time.

- On the other hand, the decay in performance of the cell detected between 200 and 1000 h of operation (Figure 4.14) appears to be strictly related to the phenomenon of Ni coarsening occurring in the anode (Figure 4.17). In particular, both the decay of voltage and the Ni growth appear to reach a plateau after about 800 h of operation.

Phase volume fraction [%]

	Cell A	Cell B	Cell C	Cell D	average	solid volume fraction
Pore	15	14.5	14.5	15	15	-
YSZ	55	55	55	55	55	64.6
Ni	30	31	30	30	30	35.4

Particle size [μm]

	Cell A	Cell B	Cell C	Cell D
Pore	0.31 ± 0.01	0.44 ± 0.04	0.42 ± 0.04	0.44 ± 0.04
YSZ	0.60 ± 0.02	0.59 ± 0.03	0.61 ± 0.01	0.62 ± 0.01
Ni	0.64 ± 0.02	0.64 ± 0.03	0.69 ± 0.02	0.77 ± 0.02

Table 4.2. Results of image analysis for the anodes of the cells

Comparison of experiment data with simulation

The results obtained from the simulation of the degradation of a composite SOFC anode are reported. All the results are obtained with the same operating conditions used experimentally and with the geometrical features found in Section 4.3 and 4.3.

Equation 4.7 has been introduced for the variation of the dimensions of Ni particles; the percolation thresholds shift to a bigger amount of Ni during time as a consequence of the increase of the size ratio P. Figure 4.18 shows that at the beginning of the operation, the percolation thresholds are for 30.4% of Ni particles and 28.4% of YSZ particles, whereas after 2000 h of operating life, they reach an asymptote and in particular, they are 34.8% for Ni and 24.5% for YSZ. It is possible to see that the percolation threshold shifts towards the composition of the electrode, causing a loss of the connectivity of the Ni percolating network; the behavior is the one described for zone III in Section 4.2.1. It must be noticed that the percolation threshold after coarsening is complete is very close to the Ni percolation threshold; crossing this composition would have caused a catastrophic degradation, as described for electrodes belonging to zone II.

In Figure 4.19, the simulated anode performance as a function of time is reported
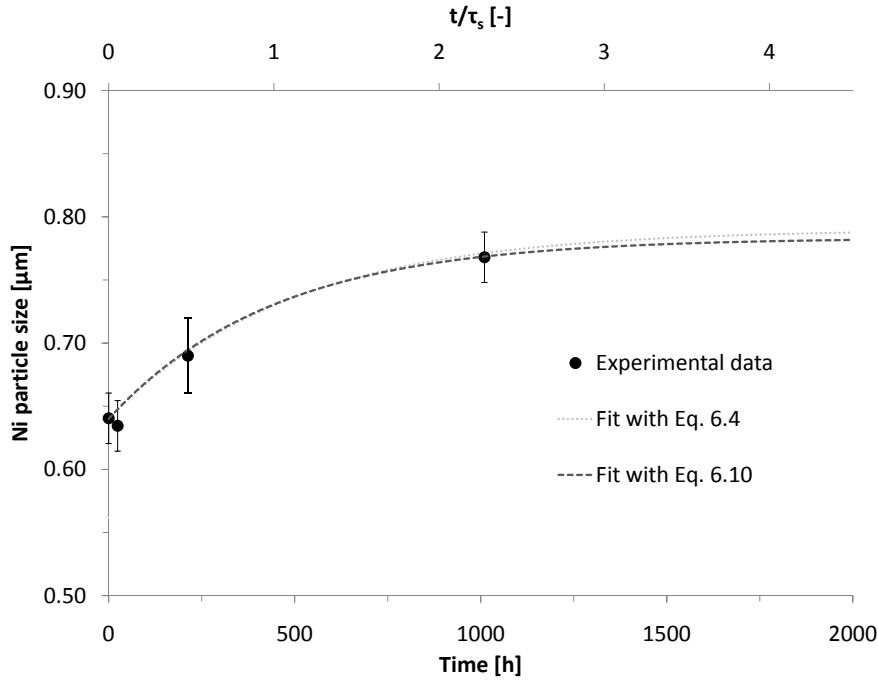
Figure 4.17. Measured average diameter for Ni particles in the anode after different operating time. The dashed lines have been obtained by best fitting through least square method using Eq. 4.4 and Eq. 4.7. The upper horizontal axis reports the time scale normalized through τ_s, the characteristic time for the coarsening process.

for the Ni composition experimentally determined. Keeping in mind that Figure 4.14 shows the operating voltage, while Figure 4.19 the electrode performance, there is a good similarity between the experimental data reported in Figure 4.14 and the simulation results of Figure 4.19. Of course, we must exclude the early operating times (before 200 h), where the experimental cell increases its performance due to an activation phenomenon which is not related to any microstructural change in the cell, as explained previously. After 200 h, it is possible to observe that the trend of the experimental data is well predicted by the simulation (Figure 4.19). Only, the time scale is different, since the plateau of the experimental performance (Figure 4.14) is found after about 800 h, while the plateau of the simulated results is found after about 3000 h. To explain this, we must consider that the composition of the anode of the experimental cell D (35.4% of Ni), is only slightly above
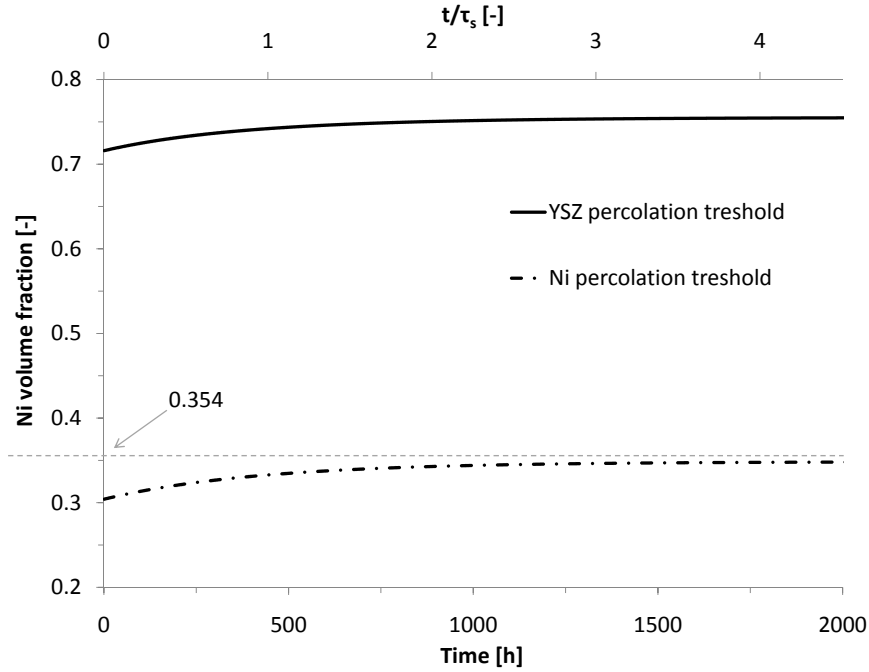
Figure 4.18. Percolation thresholds as function of time. The ordinate displays the Ni volumetric fraction in the solid portion of the electrode; the experimental value is put in evidence. The upper horizontal axis reports the time scale normalized through τ_s, the characteristic time for the coarsening process.

the asymptotic percolation threshold of Ni (34.8% of Ni, see also Figure 4.18). Under these conditions, it is clear that even a small error in the measurement of the electrode composition strongly affects the results of the simulation. For example, by looking at the results reported in Figure 4.19 for an anode with 37% of Ni, still within experimental error, it is possible to notice that, even if the trend during time is still the same, the plateau is found at much earlier operating times (about 1200 h).

Also, from data reported in Figure 4.19, it is possible to calculate the expected performance loss predicted by the model, which is between 15 mV for 37.0% of Ni and 63 mV for 35.4% of Ni, that means very close to the value found experimentally, about 65 mV.

We believe that the close agreement between the behavior of the simulation results and the experimental data for time > 200 h is a confirmation of the strict relationship
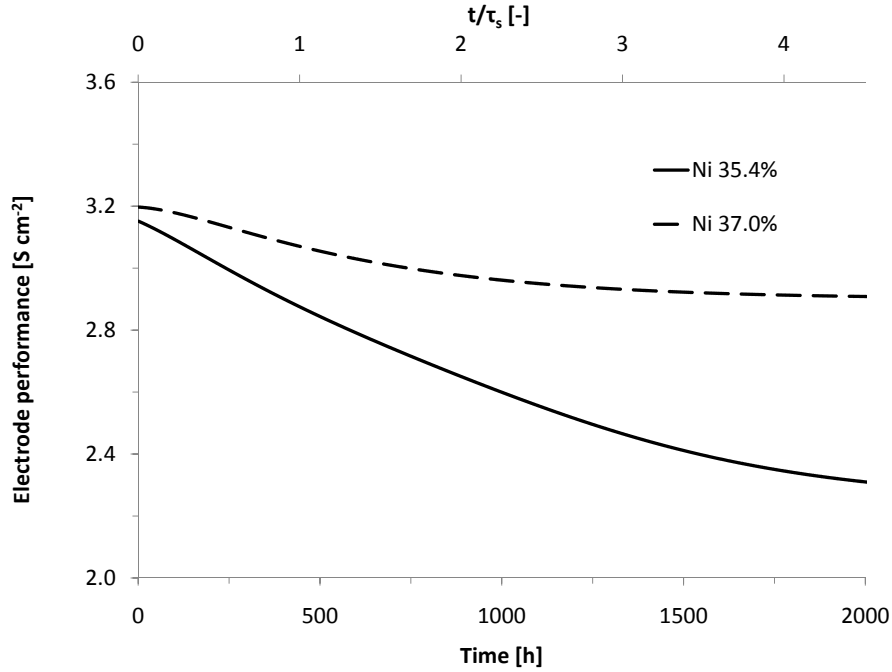
Figure 4.19. Temporal evolution of the electrode performance during the coarsening of the electronic conductor phase. Results are show for the experimental composition, 35.4% of Ni, and another composition within experimental error, 37.0% of Ni, that matches better the time scale for the degradation. The upper horizontal axis reports the time scale normalized through τ_s, the characteristic time for the coarsening process.

between the degradation of the whole cell and the microstructural changes occurring at the anode side, which is in line with other findings reported in the literature [15].

4.4 Conclusions

The modifications performed on Costamagna's percolation model permitted to explore the effect of morphological variations through the insertion of time-laws governing the main parameters that affect the electrode performance: particle dimensions, ratio between average diameters, porosity. The time-dependent model has been used to investigate theoretically a number of case-studies.

Several observations were possible, determining case-by-case what parameter was the most important between statistical effects tied to percolation, geometrical extension related to TPB area or relative conductivity of percolating network. Generally speaking, coarsening is a undesirable phenomenon that causes a performance loss in composite SOFC electrodes; cases exist in which a beneficial effect is brought by coarsening, but only for compositions not used for standard technological electrodes. However, the developed model gives a predictive capability and permits to find trade-offs between performance and durability and in particular, as explained for Ni/YSZ anodes, identify compositions that may have an initial good performance but would suffer catastrophic degradation because of the loss of electronic percolation during coarsening. The model, even if validated on anode electrodes, has general validity and can be applied to LSM/YSZ cathodes or, more generally, to two-phase mixed ionic/electronic composite electrodes.

The predictive capability of the model has been validated comparing theoretical results from simulation with electrochemical results obtained experimentally, which were found in good agreement.

We conclude that a composite mixed electronic-ionic conductor electrode is a very complex system where the transport of electronic and ionic charges is entangled with the electrochemical reaction, and that the initial morphology, coupled to a variation during operation, affects in many ways (sometimes non-intuitively) the electrochemical output of the cell.

Chapter 5

Degradation by chromium poisoning

In this chapter, the poisoning of active sites by chromium species in the LSM/YSZ electrodes is investigated. Deposition of Cr species is assumed to be preferential at the active sites; starting from this assumption, modeling based on percolation theory is used to simulate the distribution of overpotential along the electrode thickness and to derive the distribution of pollutant species within the electrode in case of low deactivation. Results from simulation are compared to Cr concentration profiles and to degradation rates obtained experimentally after a relatively short testing time (1000 h) in presence of Cr.

The model is then extended to the case of high deactivation, i.e. for times on the order of several 10k h, difficult to achieve experimentally. The impact of electrode composition on the performance loss due to Cr poisoning is then investigated from the theoretical point of view.

Results and modeling exposed in this chapter were published in the following papers:

- J. A. Schuler, P. Tanasini, A. Hessler-Wyser, C. Comninellis, and J. Van herle. Cathode thickness-dependent tolerance to Cr-poisoning in solid oxide fuel cells. Electrochemistry Communications, 12(12) :1682-1685, 2010.

- A. Nakajo, P. Tanasini, S. Diethelm, J. Van Herle, and D. Favrat. Electrochemical model of solid oxide fuel cell for simulation at the stack level. part II : Implementation

of degradation processes. Journal of the Electrochemical Society, submitted.

5.1   Introduction

In Chapter 2 it has been mentioned that there is disagreement in recent literature on the localization of the deposited Cr in SOFC electrodes, and therefore on the mechanism that controls it. It is our belief that the disagreement comes from the experimental difficulties to quantify small and localized amounts of Cr in the electrode.

Recent quantification techniques developed by A. Schuler et al. at EPFL permitted a reliable quantification in presence of LSM of Cr species with concentrations as low as 0.1 at% [97]. This permitted to extract mappings of Cr distributions in aged cells during post-mortem analysis, confirming a preferential deposition near the electrode/electrolyte interface and a progressive decrease of Cr concentration while moving away from the interface [106]. This behavior has a close correspondence with the distribution of overpotential predicted by micromodeling, and suggests that the accumulation of poisoning species is faster at the most active electrochemical sites.

Starting from this observation, a polarization-driven mechanism of Cr is assumed, with deposition rate dependent on the local overpotential [47]. The percolation-based model described in Chapter 2 is used for calculating the local overpotential and therefore the local deposition rate. Mass transfer in the gaseous phase is coupled to the model in order to obtain concentration profiles of Cr volatile species. Results from simulations are compared to deposited Cr concentration profiles obtained experimentally from post-mortem analyses performed on cells tested for about 1000 h and presenting a relatively low degradation (order of 1% per 1000 h).

In a second step, a more complex model from A. Nakajo [47] is used in order to introduce the progressive deactivation of active sites in the cathode layer; the simulations are performed with different cathode compositions, in order to predict the degradation

behavior in several cases and individuate the parameters that may give robustness against Cr poisoning.

5.2 Overpotential-driven Cr poisoning: low deactivation case

Modelling of the overpotential-driven Cr deposition

The percolation-based model described in Section 2.2 is used to estimate the distribution of the local overpotential along the electrode thickness. The local overpotential η is defined as the deviation from the equilibrium potential at one specific distance x from the electrode/electrolyte interface:

$$\eta_{(x)} = (V_{io}^{eq} - V_{el}^{eq}) - (V_{io} - V_{el})|_x \tag{5.1}$$

as opposed to the overall electrode overpotential

$$\eta_0 = (V_{io}^{eq} - V_{el}^{eq}) - (V_{io}|_{x=a} - V_{el}|_{x=0}) \tag{5.2}$$

where $V_{io}|_{x=a}$ is the potential of the ionic conductor phase at the electrode/electrolyte interface, while $V_{el}|_{x=0}$ is the potential of the electronic conductor phase at the electrode surface. Figure 5.1 shows an example of the distribution of overpotential for a typical cathode, calculated from Eq. 2.29. It is evident that, due to the higher resistivity of the ionic conductor percolating network, the local overpotential is the highest there and decays rapidly with the distance, therefore the oxygen reduction reaction takes place mainly near the electrode/electrolyte interface. As a consequence, the performance of cathodes of increasing thickness would increase until a certain point, and then any additional material would be electrochemically inert.

As already shown in Section 2.2, coupling Ohm's law for the ionic and electronic conductor phase with the linearized version of the Butler-Volmer equation and introducing adimensional variables and parameters permits to solve the differential equation problem in analytical way, so as to obtain an expression for the local overpotential as a function of x. It is then possible to put in relation the Cr deposition to the distribution of local overpotential. This has been done following the approach from Nakajo et al. [47], where
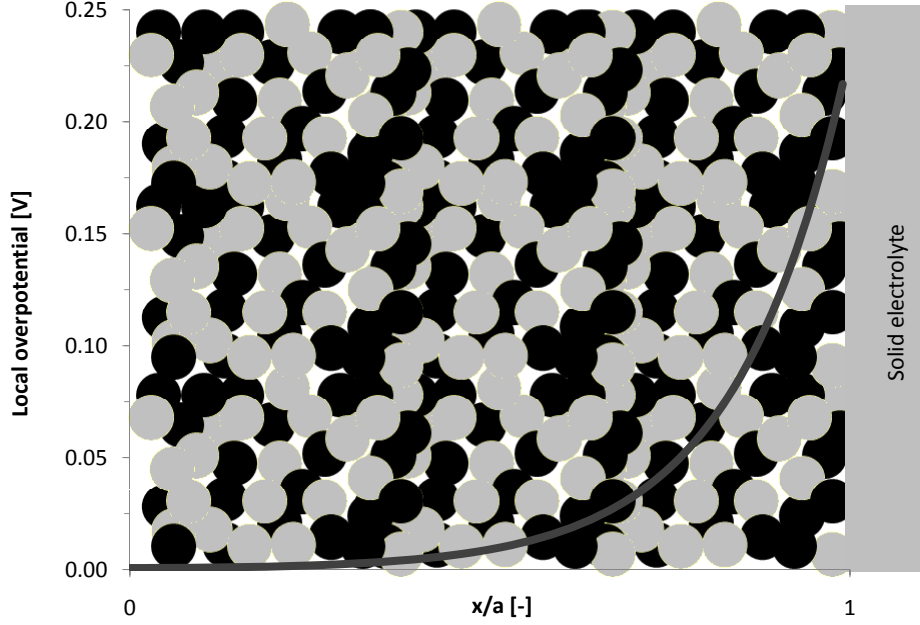
Figure 5.1. Distribution of the local overpotential η along the thickness of the electrode, as calculated from Eq. 2.29

the direct electrochemical reduction of Cr(IV) volatile species to Cr(III) blocking oxides is assumed:

$$CrO_2\left(OH\right)_{2(g)} + \frac{3}{2}V_{\ddot{O}} + 3e^-_{LSM} \rightleftharpoons \frac{1}{2}Cr_2O_{3(s)} + H_2O_{(g)} + \frac{3}{2}O^{2-} \tag{5.3}$$
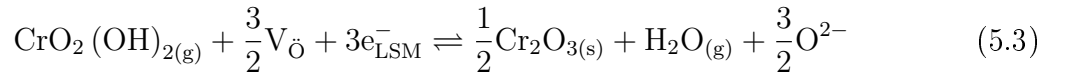
and the rate of deposition is expressed in a Butler-Volmer form, as reported in Eq. 5.4. Derivation is provided in [47]

$$j_{Cr} = i_{o,Cr} \cdot y^{1/2}_{CrO_2(OH)_2} \cdot y^{1/2}_{H_2O} \cdot 2\sinh\left(\frac{1}{2}\frac{F\eta}{RT}\right) \tag{5.4}$$

Here $y_{CrO_2(OH)_2}$ and y_{H_2O} are the gas molar fractions of Cr oxide-hydroxide and water vapor respectively, and $i_{o,Cr}$ is the exchange current density for the electrochemical reduction of $CrO_2\left(OH\right)_2$. In the simulation, the current density derived from the reaction of

Cr deposition has been neglected and it is not taken into account as a part of the total current density.

Only the Cr oxide-hydroxide has been considered as a poisoning species, since its equilibrium partial pressure is one order of magnitude bigger than for CrO_3 even at small partial pressure of water, for instance when lab compressed air is used ($4 \cdot 10^{-9}$ atm for CrO_3 and $1.3 \cdot 10^{-8}$ atm for $CrO_2 (OH)_2$ respectively [106] at 1123 K and $1.8 \cdot 10^{-3}$ atm of water vapor partial pressure).

The molar deposition rate can be obtained using Faraday's law:

$$r_{Cr} = \frac{1}{3F} j_{Cr} \tag{5.5}$$

In Eq 5.4, the partial pressure of water vapor is considered constant, since the amount present in compressed air ($\sim 2 \cdot 10^{-3}$ atm) is several orders of magnitude higher than the concentrations of reactants and products in Reaction 5.3. Also, the concentration of $O_{2(g)}$ is expected to be roughly constant in the electrode thickness and not affecting the performance of the electrode, as shown in Section 2.2. However, as it will be discussed later, even small differences in the concentration of $CrO_2 (OH)_{2(g)}$ may have an effect on the poisoning on the time scale of the thousands of hours. Therefore, the calculation of the Cr concentration profile along the thickness has been introduced by coupling the diffusion-reaction equation for mass conservation.

We apply the general equation for diffusion in a stagnant medium and in presence of a reaction to $CrO_2 (OH)_{2(g)}$ obtaining:

$$D_{eff} \nabla^2 C_{CrO_2(OH)_2} + R_{C_{CrO_2(OH)_2}} = \frac{\partial C_{CrO_2(OH)_2}}{\partial t} \tag{5.6}$$

Since the system is stationary, the accumulation term is eliminated; furthermore, we simplify the equation adapting it to our one-dimensional model:

$$D_{eff} \frac{d^2 C_{CrO_2(OH)_2}}{dx^2} = -R_{C_{CrO_2(OH)_2}} \tag{5.7}$$

The reaction can be expressed as the product of the specific reaction rate with the specific active area A:

$$R_{C_{\text{CrO}_2(\text{OH})_2}} = -A \cdot r_{\text{Cr}} \tag{5.8}$$

The negative sign has been applied to represent the fact that the reaction represents the consumption of $\text{CrO}_2(\text{OH})_{2(\text{g})}$, and r_{Cr} is a positive quantity from its definition in Eq. 5.5. Rearranging, we obtain:

$$\frac{d^2 C_{\text{CrO}_2(\text{OH})_2}}{dx^2} = r_{\text{Cr}} \frac{A}{D_{eff}} \tag{5.9}$$

Where D_{eff} is the effective diffusion coefficient and has been calculated as:

$$D_{eff} = D \frac{\varepsilon}{\tau_{pore}} \tag{5.10}$$

where ε is the electrode porosity, and τ_{pore} the pore tortuosity, estimated to 0.4 and 4, respectively.

As predicated by Eq. 5.4 and 5.5, the Cr deposition is expected to happen according to the distribution of the local overpotential. Indeed, as shown by Figure 5.2 (black curve), the Cr deposition rate follows the same type of trend than the local overpotential, predicting the highest contamination rate at the interface.

It is possible to solve numerically the differential equation system and obtain the profile of the $\text{CrO}_2(\text{OH})_{2(\text{g})}$ concentration putting together Eq. 2.29 and Eq. 5.4-5.9, along with the boundary conditions

$$\begin{cases} \text{I)} \quad D_{eff} \frac{dC_{\text{CrO}_2(\text{OH})_2}}{dx} \Big|_{x=a} = 0 \\ \text{II)} \quad C_{\text{CrO}_2(\text{OH})_2} \Big|_{x=0} = C_{\text{CrO}_2(\text{OH})_2,\text{airflow}} \end{cases} \tag{5.11}$$

Eq. 5.11, I represents the diffusion flux calculated with Fick's law at the dense electrolyte surface; it must be equal to zero since the dense electrolyte is impermeable to gas diffusion. Eq. 5.11, II represents the known value of the concentration of Cr oxide-hydroxide in the air flow feed. The shape of the solution is shown schematically in Figure 5.2 (green curve).

A further manipulation is needed to obtain the total rate of Cr deposition in the electrode. It is necessary to integrate the local deposition rate $r_{Cr(x)}$ along the electrode thickness to obtain the total rate of Cr deposition :

$$R_{Cr,tot} = A \int_V r_{Cr} dV \tag{5.12}$$

From Eq. 5.9 and 5.12, it is possible to obtain, normalizing with respect to the electrode surface S:

$$r_{Cr,tot} = \frac{R_{Cr,tot}}{S} = A \int_0^a r_{Cr} dx = D_{eff} \int_0^a \frac{d^2 C_{CrO_2(OH)_2}}{dx^2} \tag{5.13}$$

developing the integral, and knowing that $D_{eff} \frac{dC_{CrO_2(OH)_2}}{dx}\Big|_{x=a}$ is zero as a boundary condition, we obtain:

$$r_{Cr,tot} = -D_{eff} \frac{dC_{CrO_2(OH)_2}}{dx}\Big|_{x=0} \tag{5.14}$$

Eq. 5.14 simply indicates that the Cr deposited inside the electrode volume per unit of time and surface ($r_{Cr,tot}$) is equal to the diffusive flux, calculated through Fick's law, entering the electrode at its surface. No exit flux is considered, the Cr is assumed to be permanently deposited somewhere inside the cathode and re-evaporation is neglected. This assumption is based on the fact that re-evaporation would need the oxidation of Cr(III) back to Cr(IV), considered unlikely under polarization conditions near the TPB.

This concept is graphically illustrated in Figure 5.2.

From the experimental point of view, the accessible information about the Cr deposited inside an electrode is the quantification of the deposited profile after a certain time, which is an physical quantity different from the deposition *rates* that have been obtained with Eq. 5.5 (local rate) and Eq. 5.14 (total rate). In order to compare the results of the model with experimental data is therefore necessary to make an assumption: we consider that, while the degradation is small (on the order of 1% performance loss), the local overpotential profile shown in Fig 5.1 is constant and equal to the initial condition $\eta_{(x)}\big|_{t=0}$. While this
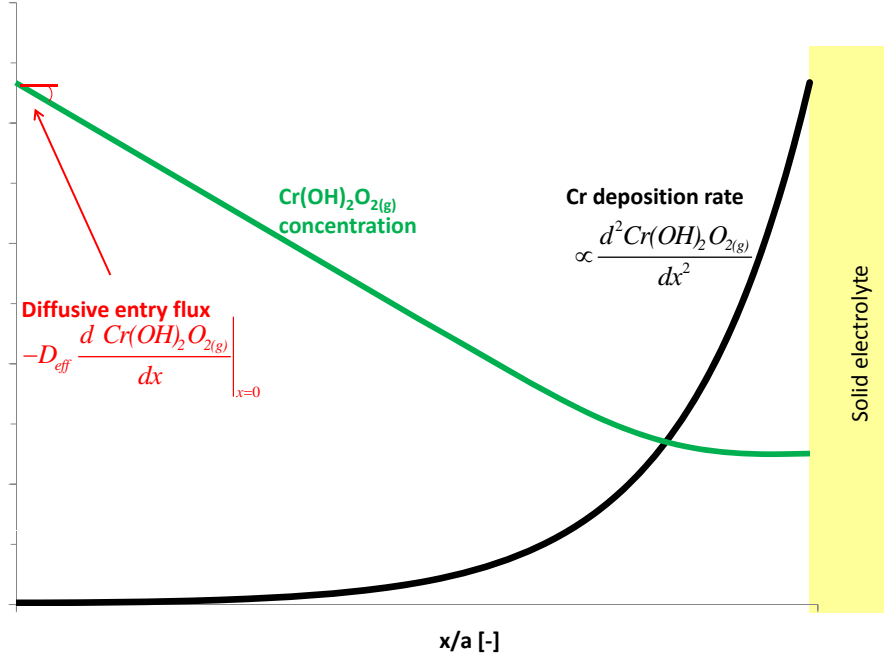
Figure 5.2. Schematic representation of the profile of the concentration of $CrO_2(OH)_{2(g)}$ and of the Cr deposition rate in the cathode. The physical meaning of Eq. 5.13 and 5.14 is put into evidence, showing that the specific total reaction rate $r_{Cr,tot}$ is equal to the diffusing flux of $CrO_2(OH)_{2(g)}$ at the electrode surface.

cannot be considered true for very long operating times and heavy performance losses (since the poisoning will change the shape of $\eta_{(x)}$), the "initial conditions" approximation permits to assume, as a consequence of the invariance of $\eta_{(x)}\big|_{t=0}$, that the local and global deposition rates don't change with time. This allows estimating q_{Cr}, the total amount per unit surface of Cr deposited in the electrode during the test, by simple multiplication with the experimental time:

$$q_{Cr} = t_{test} \cdot r_{Cr,tot} \tag{5.15}$$

Furthermore, the expected profile of deposited Cr will be exactly correspondent to the local deposition rate r_{Cr} shown in Figure 5.2 (black line) since a constant $\eta_{(x)}$ implies

a constant local rate $\left(r_{\text{Cr}(x)} = r_{\text{Cr}(x)}\big|_{t=0}\right)$ and consequently the local concentration of deposited Cr $C_{Dep\text{Cr}}$ will be equal to:

$$C_{Dep\text{Cr}(x)} = t_{test} \cdot Ar_{\text{Cr}(x)} \tag{5.16}$$

As a final step, the model has been completed with the addition of a non-reactive, 10 μm thick current collection layer (CCL), in order to match the real experimental conditions. This layer has obviously no electrochemical activity; only diffusion in the gas phase happens there and, as a consequence, we have:

$$-D_{eff}\frac{dC_{\text{CrO}_2(\text{OH})_2}}{dx}\bigg|_{CCL} = const = -D_{eff}\frac{dC_{\text{CrO}_2(\text{OH})_2}}{dx}\bigg|_{x=0} \tag{5.17}$$

It has been said that one of the boundary conditions necessary to solve the equation is the $\text{CrO}_2(\text{OH})_{2(\text{g})}$ concentration in the air flow; with the addition of this extra layer the boundary is now located at the air/CCL interface i.e. shifted of a distance a_{CCL} equal to the thickness of the CCL. Eq. 5.18 replaces the previous boundary condition in the case of the presence of a CCL:

$$\text{CrO}_2(\text{OH})_{2(\text{g})}\bigg|_{x=-a_{CCL}} = \text{CrO}_2(\text{OH})_{2(\text{g}),\text{airflow}} \tag{5.18}$$

The last point for completing the model is the estimation of the parameters. For the simulations, the value for D has been taken from literature [107] and is $2.2 \cdot 10^{-5}$ m^2/s. The value for $\text{CrO}_2(\text{OH})_{2(\text{g}),\text{airflow}}$ has been calculated: the evaporation of Cr species from the alloy used in the test equipment in usual experimental conditions (450 ml/min of air, 5% relative humidity, 1123 K) is estimated to $1 \cdot 10^{-11}$ kg/m^{2}s under equilibrium evaporation conditions [106, 108], i.e. when the amount of Cr transported by solid-state diffusion through the surface oxide scale is equal to the Cr species evaporating from the surface (the oxide scale is in equilibrium and the growth is zero). Knowing that the internal surface of the feeding alloy tube is $4.7 \cdot 10^{-3}$ m^2, the partial pressure of $\text{CrO}_2(\text{OH})_{2(\text{g})}$ was estimated to $3 \cdot 10^{-9}$ atm. No diffusion layer has been considered in the air near the CCL surface, because of the high velocity of the air provided by the feeding flux. The

parameter $i_{o,\text{Cr}}$ is unknown and has been considered an adjustable parameter of the model and fixed to have q_{Cr} agreeing with the amount of Cr found experimentally in a cell tested for about 1000 h, i.e. $\sim 2\ \mu\text{g/cm}^2$ (see Section 5.2). The value obtained is $\sim 4\ \text{A/m}^2$, in good agreement with the value calculated by Nakajo et al. (6.44 A/m^2) [47] using data from the literature. Finally, the profile of $\eta_{(x)}$ has been calculated with the percolation model shown in Section 2.2, using typical values for LSM/YSZ cathodes.

In summary, a model has been developed assuming an overpotential-driven Cr poisoning of the cathodes and coupling Cr transfer by diffusion in the gas phase inside the pores. The model developed permits the calculation of the $\text{CrO}_2\,(\text{OH})_{2(g)}$ concentration profile in the cathode thickness and allows an estimation of the expected profile of the deposited Cr in the cathode material for cells that underwent a small degradation.

Comparison of experimental results with the model, using different electrode thicknesses

The model presented in the previous Section allows a prediction of the profiles of deposited Cr for cells that underwent a relatively low degradation, of the order of a few percent. In order to compare the prediction obtained by modelling with experimental results, in this Section will be presented the electrochemical characterization and post-mortem analysis of a cell test carried out in presence of a Cr source. The multicathode setup allowed the testing of four cathodes of different thickness at the same time and under the same conditions, giving the possibility of studying the effect of the cathode thickness both from the experimental and modelling point of view.

A multicathode test was carried out to investigate cell operation in presence of the Cr-containing test-rig tubular pipes for air feeding and test flanges (made of Inconel 602). Four cathodes of identical composition (50% v/v LSM/YSZ, average particle diameter $d_{v,50} = 0.3\ \mu\text{m}$) were deposited on the anode support by screen-printing successively a different numbers of layers. Each layer consisted of approximately 5 μm of cathode material; as described in Chapter 3 , a current collection layer (CCL) made of LSM and about 10 μm thick has been deposited on top of the active layers. The segments have been tested at

850 °C in 7% humidified H_2 at 0.6 A/cm^2 for about 1100 h. Figure 5.3 shows the operating voltage of the four segments during operation; the monolayer cathode (5 μm) shows worse performances than the three other cathodes, which have a quite similar behavior after activation. This can be explained by the fact that a too thin electrode has its active area limited by the thickness. Micro-modeling based on percolation theory predicts that, in typical SOFC conditions, the reaction extends for 5-10 μm from the electrolyte; the performance of thin electrodes is limited and they benefit from an increase of thickness until this critical thickness is reached [63, 64], because of the geometrical extension of the active area. An additional increase in thickness does not extend the active zone; only the electronic current passes through. Figure 5.4 shows the predicted performance for electrodes of different thicknesses, using the parameters corresponding to the operating conditions of the experimentally tested cells. The experimental data obtained follow, within experimental error, this behavior showing that an increase in electrode thickness increases the performance only below a critical value, but that extra layers above that cause no further improvement.

Simulations varying the electrode thickness permit to compare the predicted distribution of local overpotential, as shown in Figure 5.5; from the graphic it is possible to observe that indeed the 10, 15, and 20 μm thick electrodes behave in a similar way, with about 10 μm active zone near the electrode/electrolyte interface and a marginally active zone beyond that. The 5 μm electrode is working more homogeneously and at a higher local overpotential in order to provide the same amount of current, imposed equal on all the segments in galvanostatic mode .

Results in Figure 5.3 show an interesting element concerning electrode degradation: there is a clear trend, since degradation increases with decreasing thickness. In effect, the degradation rate, expressed as loss of operating voltage percent, has been estimated to be about ∼0.9%/1000 h for the 20 μm cathode, ∼1.5%/1000 h for the 15 μm cathode, ∼2.2%/1000 h for the 10 μm cathode and ∼6%/1000 h for the 5 μm cathode. This has been considered related to the presence Cr as contaminant into the active cathode layer stemming from the tubing elements and test flanges, since short-term re-activation caused
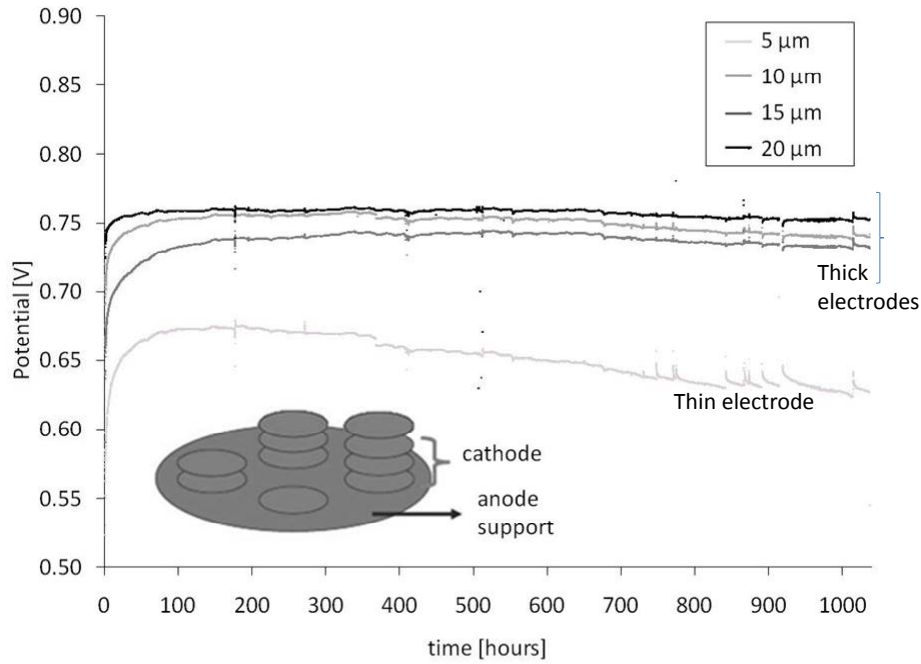
Figure 5.3. Operating voltage of segments of different thickness. After activation, the 5 μm thick segment has limited performance while thicker segments have a similar and better performance. Thickness is also related to degradation, with thicker cathodes showing a better stability.

by the interruption of the current has been found, followed by a rapid decay, as it has already been reported in literature in the case of Cr-poisoning [23, 24].

Chromium quantification has been performed on cathode cross-sections as described in Section 3.4.2, in order to obtain the concentration profile for each segment. Results are shown in Figure 5.6. It is clear comparing Figures 5.6 and 5.5, that there is a very close correspondence between the distribution of the Cr species found experimentally and the distribution of local overpotential simulated by modelling in Section 5.2. That means, the mechanism of Cr deposition appears to be directly related to the electrochemical activity of the TPB sites, either by direct or indirect electrochemical deposition. As a consequence, not only the poisoning is believed to happen selectively on active sites, but it is expected to block *especially* the most active sites. This can explain why degradation can be severe even
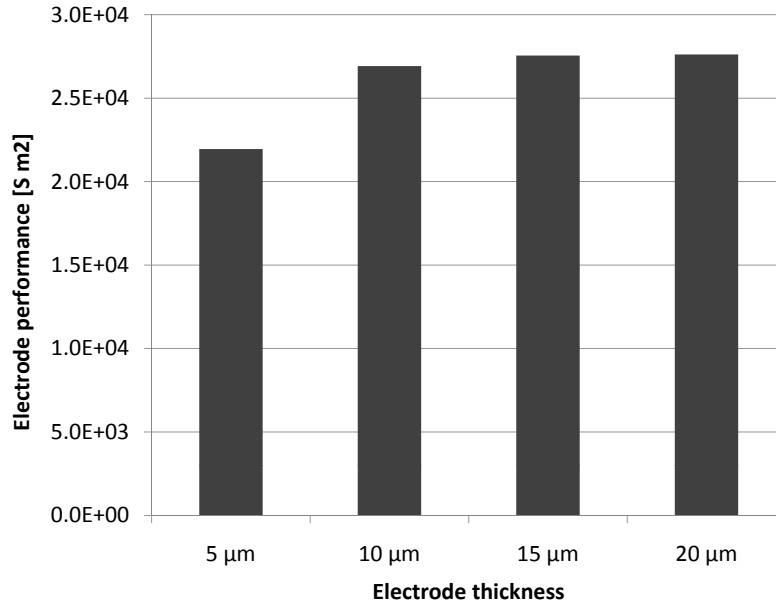
Figure 5.4. Simulated performance (reciprocal ASR) of segments of different thickness. It is evident that, for an electrode of this composition, the active layer can extend to about 10 μm, and further layers above this value would be inactive. On the other hand, a thickness of 5 μm causes the performance to be limited.
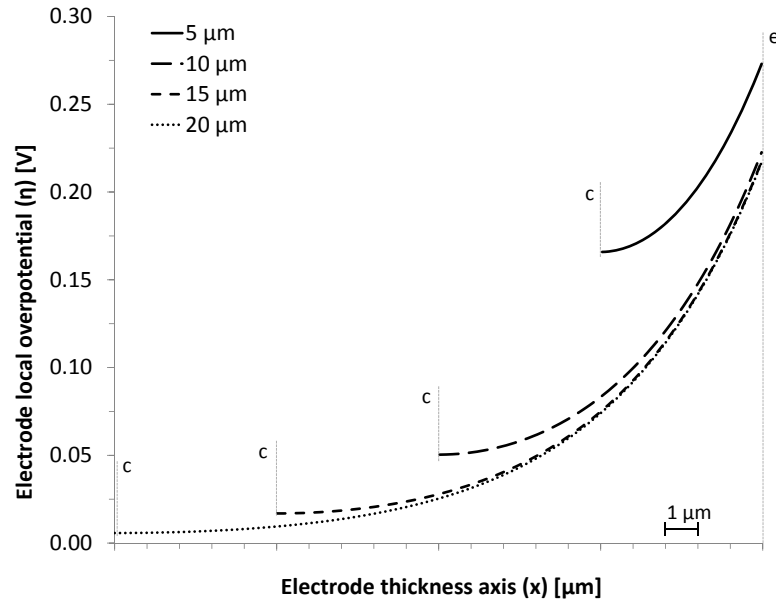
Figure 5.5. Local overpotential η of electrodes with different thickness. The 5 μm thick segment has limited performance while thicker segments have a similar and better performance. (e): electrode/electrolyte interface (common for all the curves). (c): CCL/electrode interface.
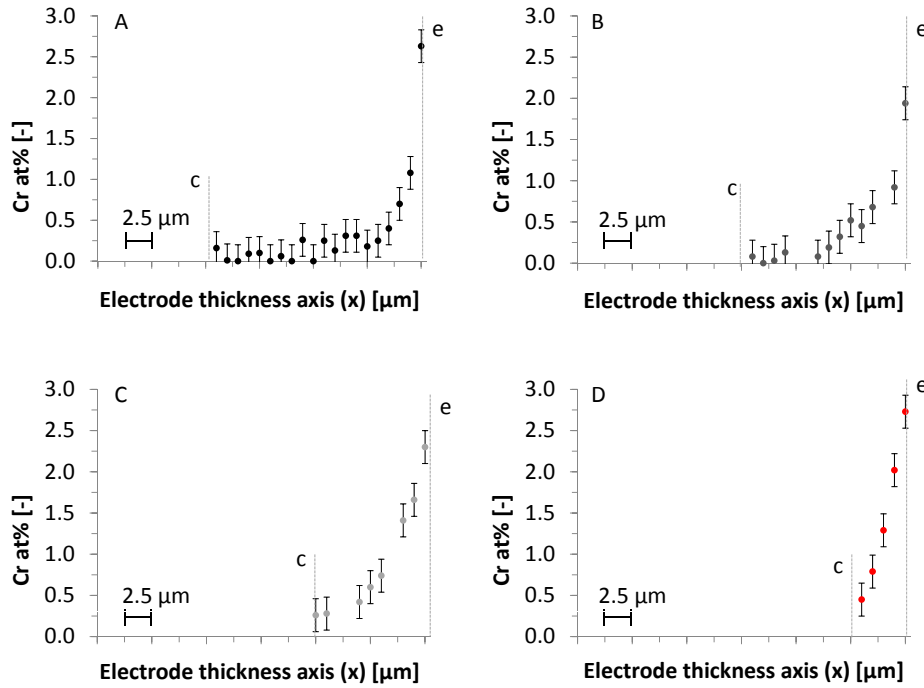
Figure 5.6. Deposited Cr concentration profiles in cathodes with 5, 10, 15 and 20 μm thicknesses after 1000 h of operation. Cr is preferentially located in the active cathode region near the electrode/electrolyte interface (e). The left end of each curve is the CCL/electrode interface (c); no Cr was found in the CCL layer. A) 20 μm thick cathode. B) 15 μm thick cathode. C) 10 μm thick cathode. A) 5 μm thick cathode.

in presence of a small concentration of contaminant in the air flow, and even if quantities as small as 0.1 at% are deposited in the electrode.

The fact that, as already mentioned, the distribution of local overpotential is similar for the 10, 15, and 20 μm thick electrodes should imply a similar degradation behavior for these three segments according to Eq. 5.4, if we consider constant the gas concentrations; in practice, a thickness-dependent tolerance to Cr-poisoning is observed. Our hypothesis, based on the observations and measurements presented above, is that the additional cathode thickness acts as a diffusion barrier, decreasing the effective concentration of Cr species in the underlying active area and therefore slowing down its accumulation [106].

In order to explain this phenomenon, an effect of the difference in $CrO_2 (OH)_{2(g)}$ concen-

tration is supposed, caused by a "diffusion-barrier" effect. Figure 5.7 shows $CrO_2(OH)_{2(g)}$ profiles obtained with the model presented in Section 5.2, illustrating that the diffusion causes a small decrease of the Cr concentration in the active part of the cathode. The overall gradient accounts for about 3% of the $CrO_2(OH)_{2(g)}$ concentration in the air flow, and the difference between the concentrations at the electrolyte surface has a variation of the order of the 1% between each cell. According to Eq. 5.4, this has a direct influence on the deposition rate, supporting the hypothesis of the beneficial effect of a diffusion barrier.

On the other hand, the higher degradation for the 5 µm thick cathode is easily explained by the fact that, as shown in Figure 5.5, a higher local overpotential is required to sustain the same overall rate for the ORR . According to Eq. 5.4, this implies a deposition rate generally higher than for the other electrodes, i.e. a faster poisoning. Moreover, the vicinity of the cathode/electrolyte interface zone, which has the highest electrochemical activity, with the air flow, means that the barrier effect is minimal for such a thin cathode.

The profiles of deposited Cr obtained by modelling are compared to the experimental results in Figure 5.8. The agreement, within experimental error, is good for the 10, 15, and 20 µm thick cathodes. However, the expected Cr profile is quantitatively different for the 5 µm thick cathode, and only the trend is captured by the simulation. In our opinion, this is may be due to the fact that the degradation for this electrode is higher than for the others (6% versus 1-2%), so that the criterion for the "initial conditions" approximation is not respected.

In conclusion, the results obtained by modelling agree with the Cr profiles found experimentally on the operated cells. This confirms not only that the deposition of Cr poisoning species is indeed overpotential-driven, but also permitted to highlight an influence of the mass transfer of the contaminants on the degradation. Both theoretical simulations and experimental results indicate that the thickness has a two-fold protective effect, decreasing the local overpotential (until a certain critical thickness) and, in any case, creating a diffusion barrier for the contaminants.

On the other side, the model showed limitations in its prediction capability in the case of a performance loss higher than 1-2%. Furthermore, no quantitative relationship has
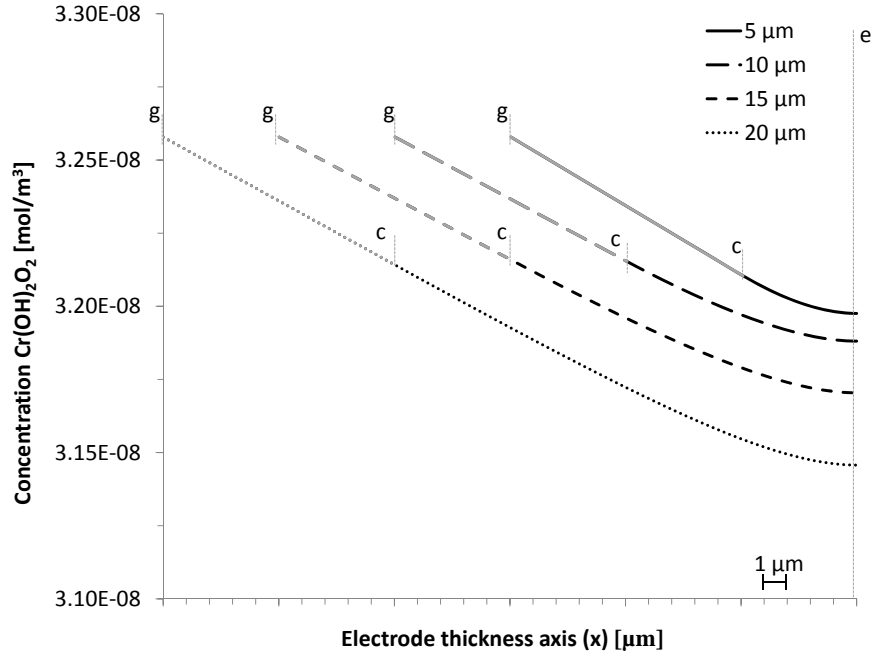
Figure 5.7. $CrO_2 (OH)_{2(g)}$ concentration along the electrode thickness for electrodes with different thickness. The gray part of the curves represent the CCL zone, where only diffusion take place. (g): gas/CCL interface. (e): electrode/electrolyte interface (common for all the curves). (c): CCL/electrode interface.

been established between the amount of deposited Cr and the performance loss of the cell. These two points will be addressed in the following Section.

5.3 Overpotential-driven Cr poisoning: high deactivation case

In the previous sections a simple model has been established to relate the deposition of Cr poisoning species to the local cathode overpotential. However, an assumption has been made that poisoning must be relatively low (on the order of few percents) in order to consider constant the distribution of the local overpotential along the electrode thickness.
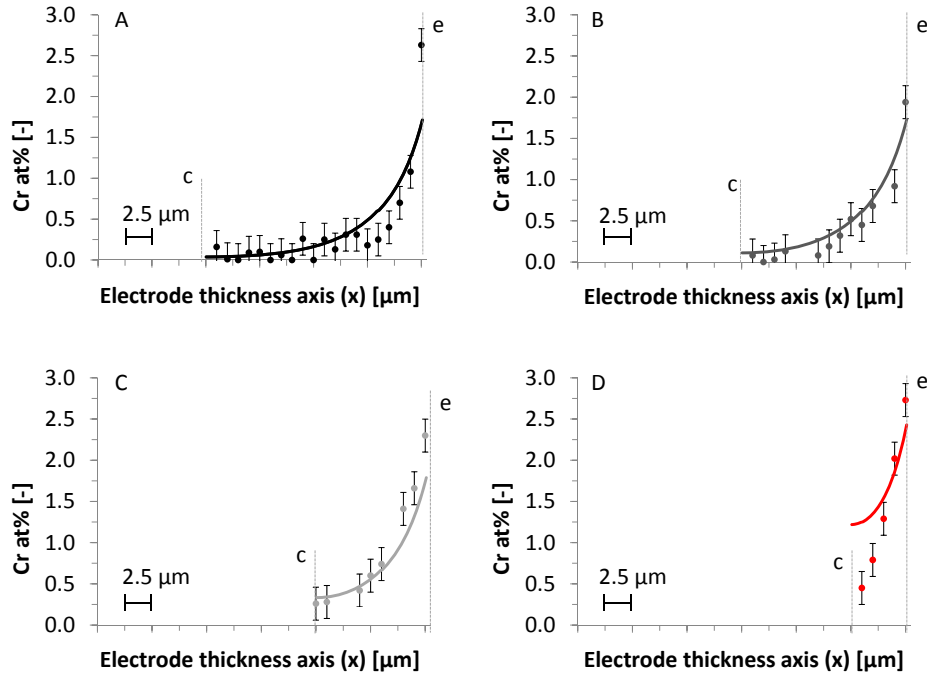
Figure 5.8. The results from simulation (lines) are compared to the experimental data (points) obtained by Cr quantification and already presented in Figure 5.6. A) 20 μm thick cathode. B) 15 μm thick cathode. C) 10 μm thick cathode. D) 5 μm thick cathode. The model has one fitting parameter, $i_{o,Cr}$, that has been adjusted so as to have a total amount of deposited Cr of ~ 2 μg/cm^2, corresponding to the total amount found experimentally. The agreement is good for the 10, 15, and 20 μm thick cathodes, while in the case of the 5 μm thick cathode only the trend is captured. (c): CCL/electrode interface. (e): electrode/electrolyte interface.

In other words, it is a "time-zero model", evaluating the mechanism of deposition of the Cr on a freshly prepared electrode, and for a relatively short period of time.

In reality, the progressive deposition of Cr on the active sites will eventually block them and cause and a variation of the shape of the distribution of the overpotential. The deposition happens especially near the electrode/electrolyte interface, as seen previously; in the case of an electrode operated at constant current, we could expect a progressive "migration" of the electrochemical activity away from the interface in order to maintain the overall rate in the electrode.

In any case, a more complete electrochemical model must be used to introduce a

progressive blocking of the active sites with time. This can be done converting A, the active area initially constant in the whole electrode, as a function of both the x-coordinate and time.

In this Section will be used the electrochemical model for cathode degradation developed at EPFL by A. Nakajo in his thesis [107] and implemented with the equation solver software gProms®. The approach consists in considering the chromia solid phase growing onto the active area until reaching a certain maximum thickness $h_{Cr_2O_3}$. Starting from this assumption, the amount of active area progressively blocked by the chromia scale can be easily calculated from the current related to the Cr deposition (Eq. 5.4) and Faraday's law, knowing the mass of oxide, its molar mass and its density; the value for $h_{Cr_2O_3}$ has been extracted from literature [29] and fixed to 60 nm. The variation of active area, dependent on time and on the local overpotential, is illustrated in Eq. 5.19:

$$\frac{1}{A}\frac{\partial A}{\partial t} = -j_{Cr}\frac{1}{2F}\frac{M_{Cr_2O_3}}{\rho_{Cr_2O_3}\,h_{Cr_2O_3}} \tag{5.19}$$

This scenario of full blocking of the active sites by the Cr poisoning species is an over-simplification, but it allows capturing the time and spatial resolution of the degradation phenomenon and permits a quantitative treatment of the performance loss. For the sake of simplicity, the Cr concentration in the gas phase has been considered constant through the electrode. A last simplification lies in considering the composition of the oxide scale as pure chromia Cr_2O_3.

The simulation is run as follows [107, 47]:

1. The local overpotential $\eta_{(x)}$ is calculated at the starting time, when $A_{(x)}$ has a constant value, homogeneous in the whole electrode and still equal to its initial value A_0.

2. Using the same relationship presented in Eq. 5.4, a local blocking rate is obtained from Eq. 5.19.

3. The active area $A_{(x,t_1)}$ is calculated after a certain time segment t_1 in which the Cr poisoning is considered constant.

4. The new profile of $\eta_{(x)}$ is obtained with the new distribution of the active sites. If, as an example, the operation is considered in galvanostatic mode, the equation solver maintains a constant ORR in the electrode; as a consequence, there is an increase of the overall cathode overpotential. The simulation run in potentiostatic mode would rather bring a decrease of the operating current while the overall electrode overpotential is kept constant.

5. Steps 2 to 4 are then iterated until reaching the final operation time.

It is possible to observe that the steps 1 and 2 correspond to the "initial condition" simplification described in Section 5.2. This approach has been confirmed to give valid results for relatively small degradation, and Eq. 5.19 permits to extend the same procedure to longer times when this assumption is no longer valid. Furthermore, the quantitative determination of the active sites that are progressively blocked permits the actual calculation of the performance loss in terms of increase of overall overpotential or decrease in current density.

The degradation due to Cr poisoning was simulated for a standard LSM/YSZ cathode (50% v/v LSM/YSZ, average particle diameter $d_{v,50}= 0.3$ μm); all operation conditions were fixed equal to the experimental values used for the test described in Section 5.2 (in particular, temperature and current density were 1123 K, 0.6 A/cm^2). The thickness was chosen high to permit the study of the propagation of the contamination in the electrode on a wider scale, and was fixed to 58 μm. In order to find a suitable time interval for the iteration of the model, a number of trials were done using different values. 1000 h was found to be a good time resolution, and the results didn't show noticeable difference when shorter values were used. The simulation was then run for 100 kh in galvanostatic mode, extracting values of interest at each interval: active area distribution, overall cathode overpotential, local overpotential distributions.

As the first thing, it is useful to analyze the results obtained after one iteration of the simulation cycle described above, since it corresponds to the experimental time used for the test carried out in Section 5.2. Figure 5.9 shows the distribution of the overpotential at starting time and after 1000 h of Cr deposition. The first remark is that the absolute values are similar, but not equal to those shown in Figure 5.5; this is due to the fact that the electrochemical model used in this Section calculates the value of the exchange current density i_0 for the ORR after the local conditions, instead of using a fixed and predetermined value. The calculated value for i_0 slightly differs from the one used for previous simulations. The main point, however, is that the distribution of the overpotential can be considered substantially unchanged after 1000 h of degradation, supporting the "initial condition" approximation used in Sections 5.2 and 5.2.

As explained previously, the iterative model allows calculating the evolution of the overall cathode overpotential with time, giving a prediction of the performance degradation. Figure 5.10 shows the cathode overpotential for 100 kh of simulation.

In order to compare the results obtained by simulation with experimental data it is necessary to calculate the voltage decay for the whole cell correspondent to the increase of η_0 obtained. The simulations predict an initial cathode overpotential η_0 equal to 0.144 V; assuming the cathode contribution to be about 40% of the total cell ASR, it is possible to calculate the total overpotential of the cell: $\eta_{cell} = \frac{\eta_0}{0.4} = 0.361$ V which is a very reasonable value for the simulated conditions. The predicted performance degradation of the cell can be calculated neglecting every other contribution to the degradation apart from Cr contamination; the total cell overpotential η_{cell} at 1000 h is considered increased by an amount ΔV_{degr}, deriving from cathode poisoning, as follows:

$$\eta_{cell}|_{t=1000} = \eta_{cell}|_{t=0} + \Delta V_{degr} = \eta_{cell}|_{t=0} + (\eta_0|_{t=1000} - \eta_0|_{t=0}) \tag{5.20}$$

$\eta_0|_{t=1000}$, from the simulation represented in Figure 5.10, is predicted to be 0.148 V which brings η_{cell} from 0.361 V of the starting point to about 0.365 V after 1000 h. Assuming an OCV for the cell of about 1.050 V, this means that the operating potential
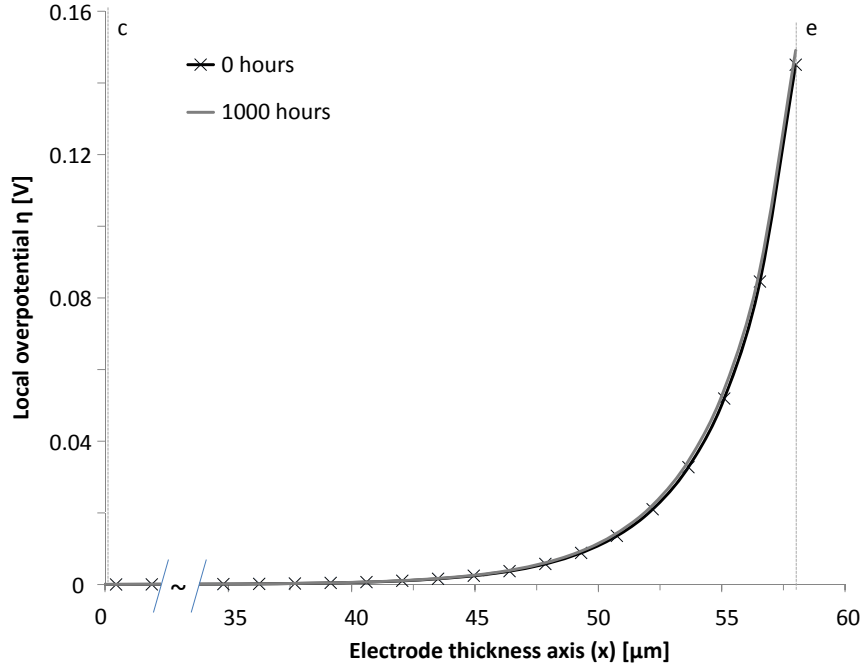
Figure 5.9. Simulated local overpotential η at the starting point and after 1000 h of operation in presence of Cr contaminants for a 58 μm-thick standard cathode (50% v/v LSM/YSZ). The two distributions are very similar; the corresponding performance degradation of the whole cell (calculated as a voltage decay) has been estimated to be around 0.6%. (c): CCL/electrode interface. (e): electrode/electrolyte interface.

of the cell passes from 0.689 V to 0.685 V, corresponding to a voltage decay of about 0.6%/1000 h; this roughly estimated cell degradation, matches well the degradation observed (∼0.9%/1000 h) for the thicker cell in Figure 5.3.

Observing Figure 5.10, more interesting features can be discussed. It is clear from the left part of the curve that the degradation accelerates as times goes on; this effect is due to the fact that the general increase of η due to the poisoning contributes to increase the Cr deposition rate. In this sense, the Cr degradation is a self-accelerating phenomenon.

On the other hand, it is possible to observe a transition point in the curve after about 30 kh, where the slope changes abruptly. This point is marked by the fact that all the active sites at the cathode/electrolyte interface have been blocked by the Cr oxide; from
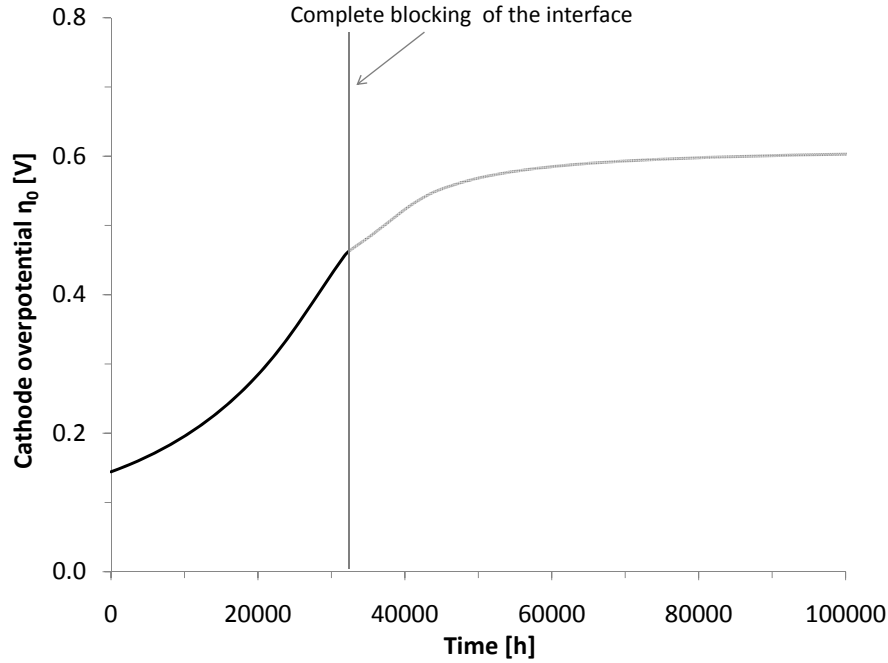
Figure 5.10. The total overpotential η_0 increases during time due to Cr poisoning for a standard cathode (50% v/v LSM/YSZ). A transition is observed around 30 kh, due to the total blocking of the active sites at the electrode/electrolyte interface. The model is considered reliable until that transition; the remaining part of the curve has been reported for the sake of completeness.

this point on, a front characterized by completely inactive material begins to move away from the interface. This "dead zone" cannot contribute anymore to the ORR and simply carries the current (in the form of O^{2-} ions) towards the dense electrolyte.

The model predicts that, starting from this point, the degradation slows down; in effect, while more and more sites are blocked, the overall blocking rate is decreased, as described by Eq. 5.19. The model also predicts a finite value of η_0 for an electrode completely blocked in all its thickness; this prediction is physically inconsistent and it is due to the fact that, for convergence reasons, a minimum value for $A_{(x)}$ must be maintained.

Following these considerations, it has been considered that the model is reliable only until the complete blocking of the interface happens, i.e. at the critical time t_{cb}. Looking at Figure 5.10, it is possible to observe that the complete blocking of the interface happens
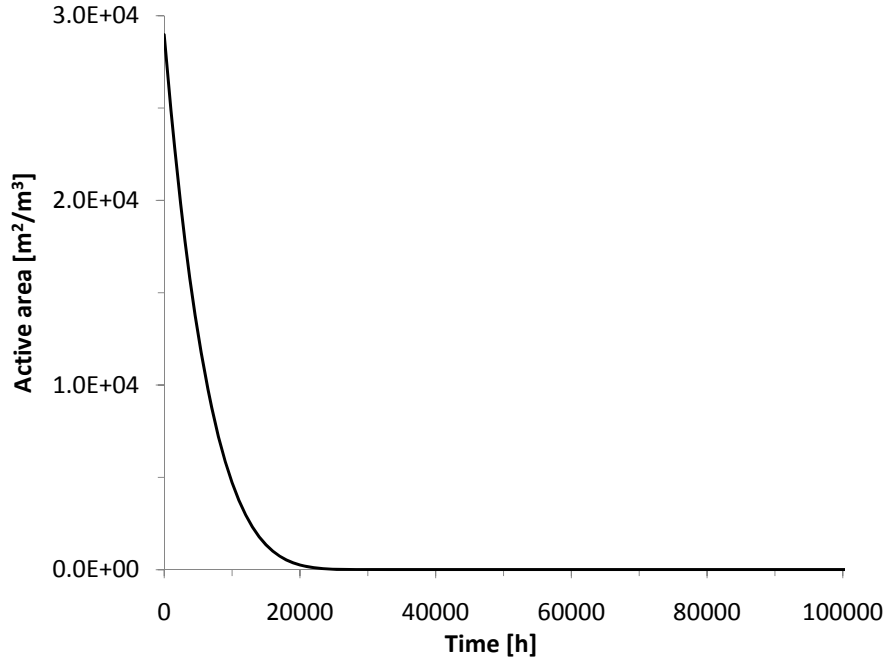
Figure 5.11. $A|_{x=a}$ is represented as a function of time for a standard cathode (50% v/v LSM/YSZ). The local overpotential is the highest at the electrode/electrolyte interface, so this is the first point of the electrode reaching the complete blocking of the active sites, which happens at around 30 kh.

when η_0 has increased three-fold with respect to $\eta_0|_{t=0}$. From a technological point of view, a cell having undergone such degradation has long reached the end of its efficient lifetime. Therefore, the limits within which the model is valid are broad enough to represent the behavior of a cell during its whole efficient lifetime.

Figure 5.12 shows a more complete view of the evolution of the system with the help of 3-dimensional graphs. Figure 5.12 A illustrates how Cr deposition, blocking the active sites, propagates inside the electrode. It is possible to observe that, as a consequence of the diminished availability of active sites near the electrode/electrolyte interface, the local overpotential increases farther away from the interface (as shown in Figure 5.12 B). This causes the deposition of Cr in zones that, inactive at the beginning of the operation, begin to provide a contribution to the ORR; on the contrary, the severely contaminated

zones decrease their chemical activity and, as a consequence, the Cr deposition. In this sense, the two graphs reported in Figure 5.12 are strictly interrelated, since the increase of η is a consequence of the loss of active area, but also the cause of site blocking in the sites that become newly active. In summary, the propagation of the contamination can be represented as a wave (Fig. 5.13) moving away from the electrolyte.

Effect of composition

As seen above, the electrochemical reaction moves away from the electrolyte as a consequence of the blocking of active sites near the electrode/electrolyte interface. Therefore, the increase in overpotential is somehow related to the need to carry the O^{2-} ions produced by the ORR through the ionic percolation network for a longer way, in average. This is a particularly important point in a LSM/YSZ electrode, since the conductivity of YSZ is relatively poor. In order to increase the conductivity of the ionic percolation network we can intervene in two ways: 1) increasing the volume fraction of the electrolyte in the composite cathode 2) using a more conductive electrolyte. Both ways will be analyzed in this Section.

Firstly, calculations have been carried out simulating electrode compositions with a higher content of YSZ; according to Eq. 2.22, this increases σ_{eff}. All other parameters were kept constant with respect to the previous simulations.

Looking at the results from numerical simulations, it is possible to see that the performance is higher for YSZ-rich cathodes. In effect, in Section 2.2 it was pointed out that, due to the relatively poor conductivity of the YSZ with respect to LSM, the optimum performance should be found with a YSZ content higher than 50% in volume. From the percolation-based micromodel [63] it is found that there are two preconditions in order to observe this behavior:

- The microstructure must be fine, meaning that it must provide A high enough not to be the limiting factor for the performance

- The electrode must be thicker than the extension of the electrochemically active zone
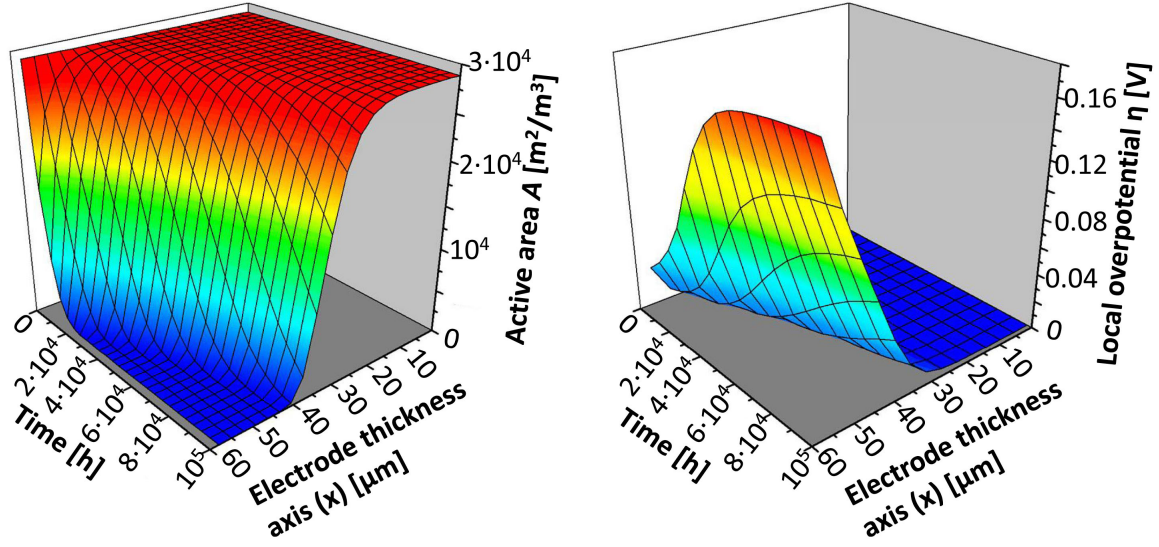
Figure 5.12. Evolution of A) Active area A, and B) local overpotential η as a function of time and position inside the electrode. The propagation of the degradation is a phenomenon related to the interdependence of the decrease of active area near the interface (that forces sites far from the electrolyte to become active) and the Cr blocking (that happens where the sites contribute to the ORR). The electrode/electrolyte interface is located at $x = 0$.
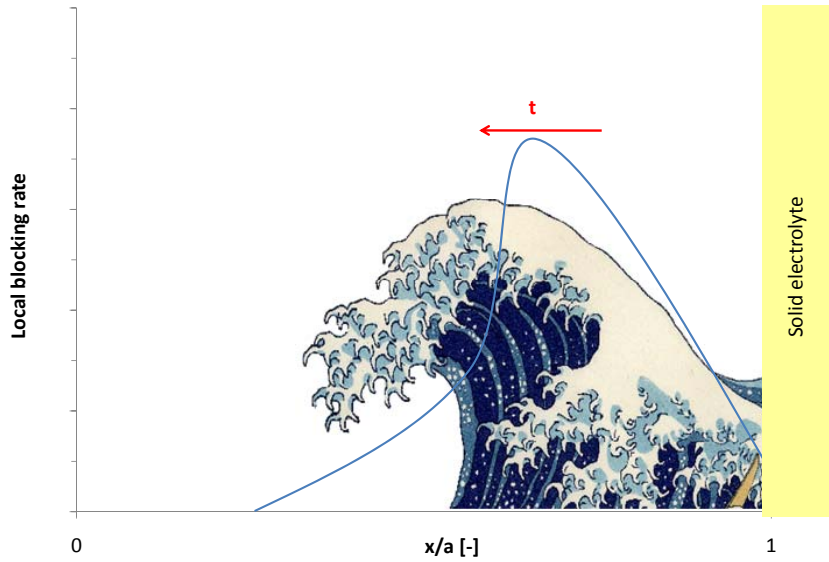
Figure 5.13. Schematic representation of Cr degradation, behaving like a wave that moves away from the electrolyte. The heavily contaminated zone (on the right) gives a small contribution to the ORR, because of the lack of active sites; the blocking rate there is low and decreasing. The highly active zone (climax of the wave) undergoes the fastest degradation. As a consequence of Cr deposition in the cathode and in order to maintain the overall ORR rate, new sites (the front of the wave) must become progressively more active; for these sites the blocking rate is low, yet increasing.

Both these requirements are met by the simulated electrode, since the average particle diameter of 0.3 µm guarantees a dense number of contacts per unit volume, and the electrode thickness has been fixed to 58 µm, which is higher than the expected extension of the electrochemically active zone (see Fig. 5.4, for instance), at least at the starting point. Since it was shown that the Cr deposition is related to the overpotential, it is obvious that more efficient electrodes have a smaller Cr deposition rate, at a given current density.

Figure 5.14 shows the distribution of local overpotential η at $t = 0$ for the four simulated compositions, and it is possible to observe that, increasing the YSZ content, the ionic transport becomes more efficient and allows a more evenly distributed electrochemical reaction, increasing the electrode performance and also slightly extending the electrochemically active zone.

Intuitively, such electrolyte-rich composites should be more robust towards Cr degradation, since the consequences of the displacement of the ORR from the interface would cause a smaller overpotential for the transport of O^{2-} ions. In other words, the same condition necessary to obtain a better performance should also cause a smaller performance loss per quantity of Cr deposited.

Figure 5.15 shows initial cathode degradation rate as a function of the electrolyte content of the electrode: it is possible to observe a net decrease of the degradation rate with increasing YSZ volume fraction. As a consequence, the increase of the time of complete blocking of the interface t_{cb}, reported in the same Figure, gives an indication of the extension of the expected electrode life-time.

Secondly, the efficiency of ionic transport in the electrode has been increased changing the ionic conductor. Scandia-stabilized zirconia (ScSZ) is known to possess a conductivity about 2-3 times higher than the YSZ [109]. According to the results obtained for YSZ electrodes, the introduction of such an electrolyte in the composite would bring not only better electrode performance, but also increased robustness toward Cr poisoning.

Calculations have been carried out, simulating electrodes with different contents of ScSZ; all the parameters were otherwise equal to those used previously. Figure 5.16 shows

Figure 5.14. Initial local overpotential η in presence of Cr contaminants for cathodes of different YSZ content. Higher contents of YSZ causes a more even distribution of the electrochemical reaction in the electrode thickness. The values for the corresponding η_0 are reported in the included table. (c): CCL/electrode interface. (e): electrode/electrolyte interface.
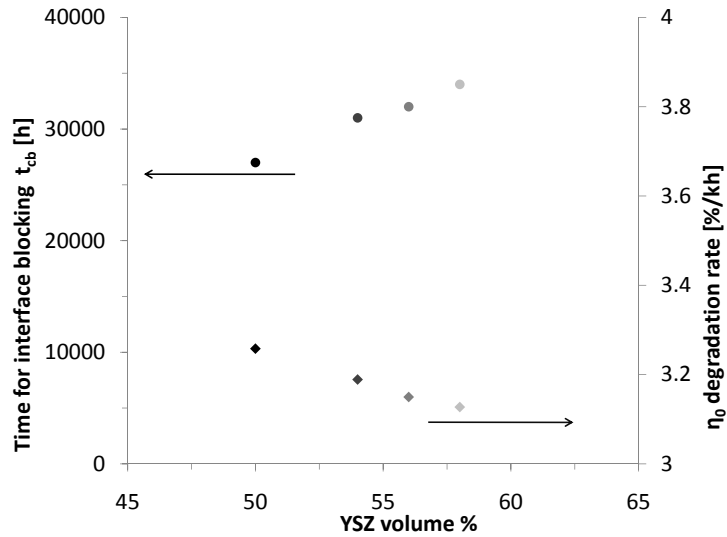
Figure 5.15. Time of complete blocking of the interface t_{cb} and the initial degradation rate of η_0 (measured as the percent increase rate at $t = 0$) are presented as a function of the YSZ content of the electrode. It is possible to observe that the increase in YSZ content has a beneficial effect on the stability of the electrode during Cr poisoning.

the distribution of the local overpotential η at $t = 0$ for the different compositions. Figure 5.17 shows initial cathode degradation rate and the time of complete blocking of the interface t_{cb} as functions of the ScSZ content of the electrode. Comparing these Figures with Figures 5.14 and 5.15 we can take two main points: 1) the enrichment in ScSZ has the same effect than for the YSZ-based electrodes, which is quite obvious 2) the increase in the electrolyte conductivity has a similar effect of the enrichment in electrolyte content, increasing both performances and robustness towards degradation.

The effect of the two methods adopted for increasing the ionic conductivity in the composite cathode goes in the same direction; however, there is a substantial difference between them. Substituting the electrolyte with a better conducting one can have a more dramatic impact, as shown in the previous Figures. This is because the change in electrolyte volume fraction can be effectively operated only in a limited range, since we are limited by the constraint of maintaining a well connected, percolating LSM network, and of the need to maintain an acceptable number of contacts LSM-electrolyte per unit volume. Shortly speaking, while increasing the electrolyte content, a trade-off must be reached between the increase in conductivity and the extension of A; a too high electrolyte content would lead to poor performances. This was already pointed out in Section 2.2, and is still valid when considering degradation. On the other hand, the increase of the intrinsic conductivity is strictly beneficial, and has no constraints whatsoever.

Not withstanding the difference between the two approaches, they can be applied simultaneously and the best results will be obtained with the combination of both. In the specific case, the life-time is expected to increase three-fold while passing from a standard 50% YSZ/LSM to an optimized 58% ScSZ/LSM electrode.

Comparison with experimental results

A multicathode cell has been prepared with four LSM/ScSZ composite segments (from now on referred as Cells 1-4) with thickness of $\sim$10 µm and different compositions and operated in presence of Cr for 3000 h at 850°C. To be more specific, Cells 1-3 were slightly enriched with ScSZ and had 54%, 56% and 58% ScSZ volume content respectively, while
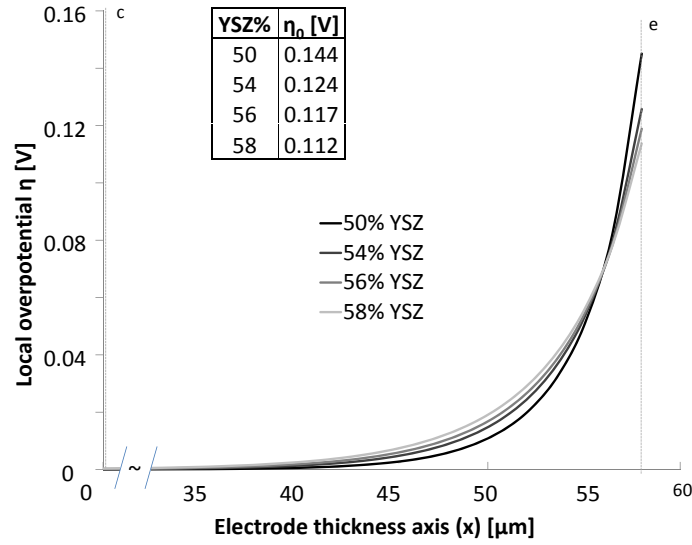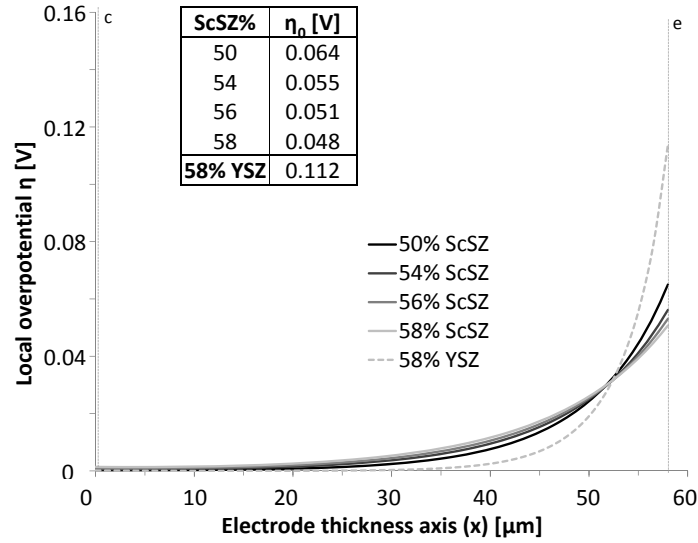
Figure 5.16. Initial local overpotential η in presence of Cr contaminants for cathodes of different ScSZ content. Higher contents of ScSZ cause a more even distribution of the electrochemical reaction in the electrode thickness. The values for the corresponding η_0 are reported in the included table. The results obtained for the 58% YSZ cathode are shown for the sake of comparison; the introduction of ScSZ takes to the extremes the effect already observed in Figure 5.14 as a consequence of the increase of YSZ%. (c): CCL/electrode interface. (e): electrode/electrolyte interface.
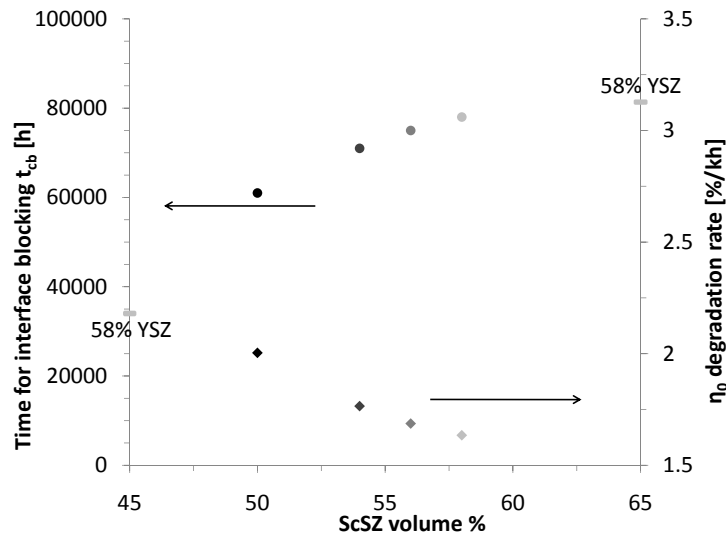
Figure 5.17. Time of complete blocking of the interface t_{cb} and initial degradation rate of η_0 (measured as the percent increase rate at $t = 0$) presented as a function of the ScSZ content of the electrode. On the respective axis, the values obtained for the 58% YSZ are indicated as a reference. It is possible to observe that both the increase in ScSZ content and the substitution of YSZ with ScSZ have a beneficial effect on the stability of the electrode during Cr poisoning.

Cell 4 was heavily enriched in ScSZ (65%), a composition near the percolation threshold for LSM conduction. The cells were deposited on an additional dense thin layer of ceria-doped gadolina (GDC), in order to avoid any kind of reactions between the LSM of the composite cathodes and the standard YSZ dense electrolyte so to isolate as much as possible the contribution of Cr poisoning to the cell degradation. The segments were operated at 0.7 A/cm², apart from Cell 4; this particular segment was operated at 0.7 A/cm² for about 200 h, during which a severe degradation took place bringing the cell potential as low as 0.14 V. For this reason, and to avoid compromising the cell integrity, the operating current density was fixed to 0.3 A/cm² on this segment for the rest of the test . Figure 5.18 shows the operation voltage as a function of time for the four segments. A last word must be spent concerning Cell 2: a different behavior than the other cells could be observed, and the cell eventually failed, as shown in the figure.

EIS measurements have been performed at about 200 h of operation (after the cathode activation period) and at ∼3000 h, the end of the test, permitting to evaluate the cathode degradation and to compare the experimental result with the simulations shown previously. In order to separate the cathode contribution from the ASR, the δZ_{real} function (see Section 3.4.1) has been calculated as a function of the frequency; it showed an evident and dominant peak at ∼20-30 Hz, corresponding to dissociative adsorption of $O_{2(g)}$ at the cathode (see Table 2.1). This indicates that the cathode process gives an important contribution to the cell resistance, especially at OCV. Furthermore, it was this particular contribution that showed the most notable increase during operation, meaning that the degradation of the cell happened mostly at the cathode side and affected specifically the electrocatalytic activity of the LSM; this results corresponds well to the expected effect of Cr poisoning blocking active sites.

Figure 5.19 reports the Bode plot of the imaginary part of the impedance $-Z_{im}$; assuming that the overlapping of the peak at ∼20-30 Hz with the neighboring peak is negligible, it is possible to estimate the resistance R_{ad} of the dissociative adsorption process, which is considered the main contribution to the resistance on the cathode side, as $R_{ad} = 2\left(-Z_{im,peak}\right)$ [91]. It is interesting to look at the measurement at OCV as useful
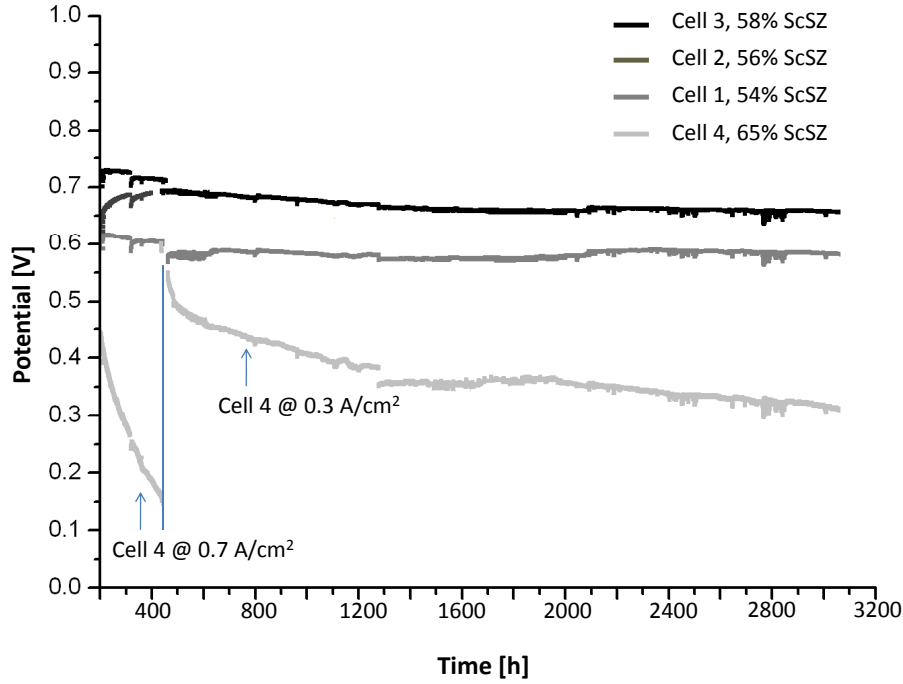
Figure 5.18. Evolution of potential of the four LSM/ScSZ segments operated at 850°C in presence of Cr. The fuel was composed by 7% H_2O and 93% H_2. From the analysis of the overall cell performance, it is possible to observe that the performance increases with the content of ScSZ, but that an electrode overly rich in ScSZ has bad performance and undergoes severe degradation if operated in the same conditions.

indicators of the cathode performance and degradation, since the size of the peaks permits to isolate and measure them easily. Table 5.1 shows the values found experimentally for R_{ad} at the beginning of the test the four segments, compared to the corresponding values found at the end of the test.

To complete the analysis, Figure 5.20 shows the subtractions spectrum-to-spectrum between the δZ_{real} functions obtained at the beginning and at the end of the test. The subtraction permits to eliminate all the constant contributions to the spectrum, and highlight the changes occurred during operation due to degradation. It is possible to see that in effect, the major change is located at ~20-30 Hz, which was already evident from the data in Table 5.1. However, a closer look at the graphs permits to identify two minors
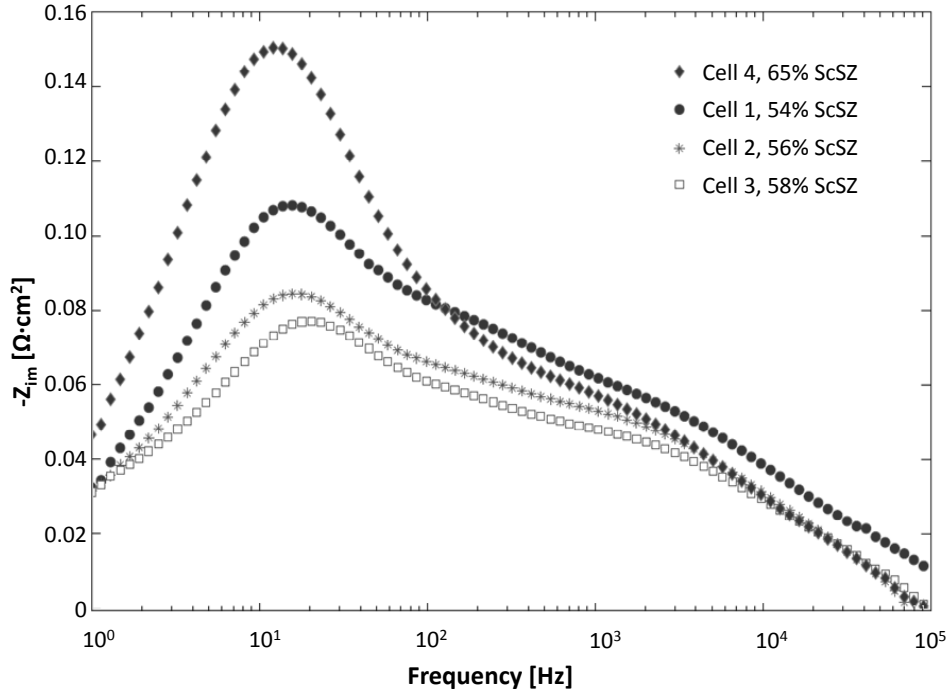
Figure 5.19. Imaginary part of the impedance $-Z_{im}$ plotted as a function of the frequency, measured at the start of the test. The peak value $-Z_{im,peak}$ has been used to estimate the values presented in Table 5.1 according to the relationship $R_{ad} = 2\left(-Z_{im,peak}\right)$. Cell 4 underwent a strong degradation from the beginning of the test, therefore the reported value has been measured at 0 h rather than after the activation.

	Composition	$R_{ad,OCV}$, start	$R_{ad,OCV}$, end
Cell 1	54% ScSZ	0.107	0.25
Cell 2	56% ScSZ	0.083	-
Cell 3	58% ScSZ	0.078	0.12
Cell 4	65% ScSZ	0.15(*)	0.65

Table 5.1. Values for the resistance $R_{ad}/\Omega\text{cm}^2$ of the dissociative adsorption process at OCV, obtained experimentally on the cells at the beginning and at the end of the 3000 h of operation. Cell 2 failed during the test, and no measurement could be done at the end of the test. (*) Cell 4 underwent a strong degradation from the beginning of the test, therefore the reported value has been taken at 0 h rather than after the activation.
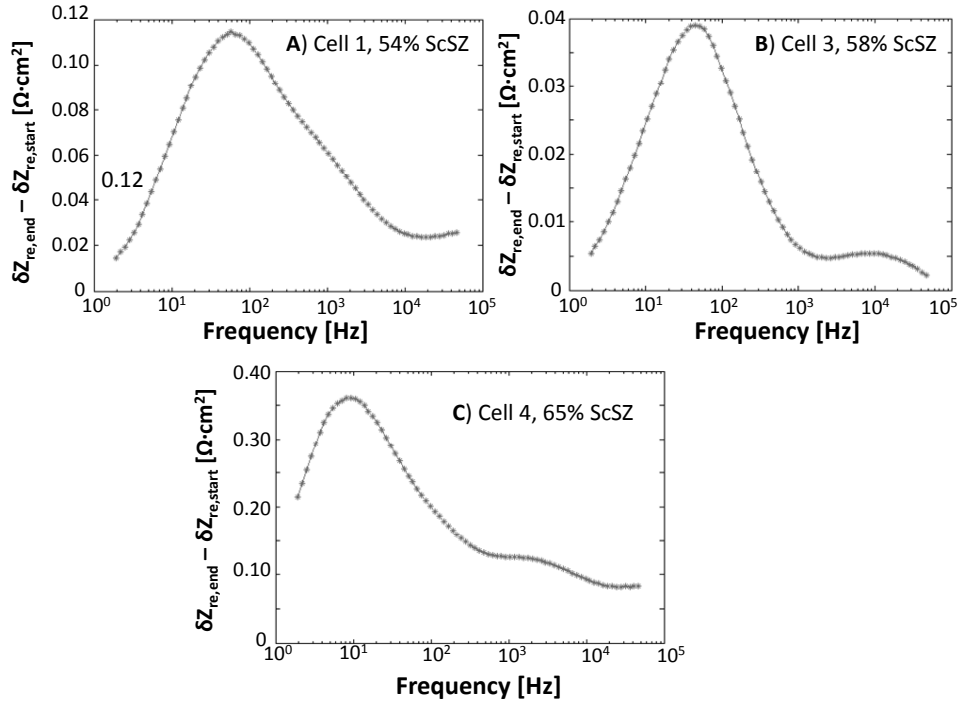
Figure 5.20. The δZ_{real} function has been calculated from the spectra taken at the start and end of the test and subtracted to each other. The resulting plot permits to identify the processes that changed the most between the two measurements; in the specific case, the increase of the cell resistance has a main contribution at around $\sim$20 Hz (dissociative adsorption of $O_{2(g)}$ at the cathode) indicating that the degradation happens mostly at the cathode side.

contributions: the most evident is located at $\sim$10^4 Hz, and can be attributed to O^{2-} transfer at the LSM/YSZ interface (see Table 2.1). The second, less evident contribution is especially visible in Figure 5.20 A, present as a shoulder of the main peak and located at $\sim$10^3 Hz. This contribution can be attributed to charge transfer at the Ni/YSZ interface; in effect, according to Chapter 4, a decrease of the performance related to the microstructural change in the anode support is expected to happen in the time scale of the first 1000 h.

A last remark can be done concerning Figure 5.20 C, reporting the data from Cell 4: this cell underwent the heaviest degradation, and apparently the characteristic frequencies of the two main cathode processes shifted towards lower values ($\sim$10 Hz and $\sim$3.10^3 Hz

for dissociative adsorption and O^{2-} transfer at the LSM/YSZ interface, respectively).

From the ensemble of the electrochemistry two observation are possible:

- The performance of the cathodes increases while increasing the ScSZ content. This result agrees only partially with the simulations since, as already mentioned, it is expected to have a benefit from the enrichment in electrolyte only above a certain thickness. For LSM/ScSZ at 850°C with $d_{v,50} = 0.3$ μm, this value is expected to be around 15 μm, above the value measured for the tested cells. In any case, the cell containing 65% ScSZ is expected to give the worse performance, and this has been confirmed by the experimental result.

- The degradation for Cell 3, with 58% ScSZ, was lower than for Cell 1, containing 54% ScSZ, in agreement with the predictions obtained by modeling. It must be added that the overly enriched cathode showed not only the worse performances, but also a extremely severe degradation. We believe that the degradation was not only related to Cr poisoning, however, but that in the extreme overpotential caused by the test condition other degradation phenomena kicked in like, for example, the formation of zirconates [15].

Post mortem analyses have been carried out on the segments, and Figure 5.21 reports the profiles of deposited Cr obtained by SEM-EDX. It was found that the presence of the GDC layer introduces an overestimation of the Cr when using the method reported in Section 3.4.2, therefore the value obtained near the interface must be ignored. The profiles of deposited Cr are otherwise comparable to those found for YSZ cells (see Fig. 5.6), but after an operation time three times longer; this is in qualitative agreement with the results obtained by modelling. The difference between the profiles is small compared to the experimental error; however, it is possible to observe that Cell 1 has a Cr concentration generally higher than Cell 3, which is in line with the prediction from simulation. The profile of Cell 4 cannot be directly compared because of the different conditions under which it was tested (0.3 A/cm^2); the fact that the Cr found is generally lower than for
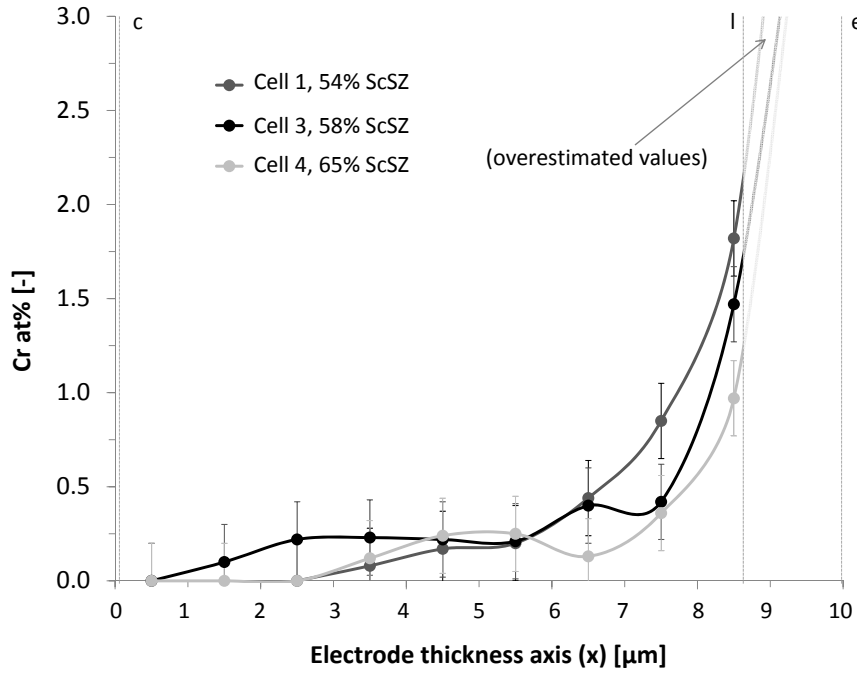
Figure 5.21. Deposited Cr concentration profiles in cathodes with 54%, 58% and 65% ScSZ after 3000 h of operation. (c): CCL/electrode interface. (e): electrode/electrolyte interface. (l) limit for the validity of Eq. 3.4 for Cr quantification. The values between (i) and (e) are overestimated because of the interference of the GDC dense electrolyte, and must be neglected.

the other segments confirms the fact that the severe degradation was not only due to Cr poisoning but also to other phenomena.

In conclusion, the test performed with LSM/ScSZ partially confirmed the predictions obtained by modelling. An unexpected positive effect of the composition on the cathode performance, not predicted by simulation for the electrode thickness used, was found experimentally; on the other hand, there is agreement between predictions and experimental data about the performance losses, and a beneficial effect of the increase of the electrolyte content was confirmed. It was also shown experimentally that the enrichment is limited by the constraint of maintaining an acceptable A; not doing so brings not only bad performances, but also severe degradation.

5.4 Conclusions

Cr volatile species present in the air feed are considered practically non-avoidable in technological devices, so that solutions should be put in place to either decrease the total amount of Cr blocking the active sites and/or reduce the performance loss tied to a fixed amount of Cr deposited in the electrode.

A theoretical model has been developed, putting in relation the distributed Cr deposition to the local electrochemical activity in cathode. This model, validated on the basis of experimental results, gives an insight and a prediction capability concerning the effect of several operative parameters on the degradation caused by Cr poisoning. From this analysis we can deduce that both the geometrical extension of the electrode (specifically its thickness) and the composition (type and volume fraction of the electrolyte) can be optimized to decrease the performance loss when in presence of Cr species.

In particular, extra thickness is considered to cause a "barrier effect", decreasing the absolute amount of Cr deposited in the cathode. A higher efficiency in the ionic transport in the electrode, achieved by both the introduction of a more conductive electrolyte (ScSZ instead of YSZ) and the increase of the volume fraction of the ionic conductor, leads to lower total overpotential and, again, to lower amount of deposited Cr. But in this second case, there is also an indirect advantage: the poisoning forces the electrochemical reaction to take place farther away from the dense electrolyte, creating the need to move them for a longer way - and therefore causing a performance loss. In this sense, a more efficient transport of O^{2-} ions leads to a smaller performance loss per quantity of deposited Cr.

Chapter 6

Other cathode degradation and analysis aspects

In this chapter, the results obtained in the final part of the thesis are exposed. These investigation routes were taken as a result of the work shown in the preceding Chapters, and are currently under development. In particular, new methods for 3D reconstruction of the microstructure (FIB and XCT) have been tested and validated on SOFC cathodes, as an alternative to the 2D analysis shown in Chapter 4.

Furthermore, a method has been established for the study of the reactivity of LSM/electrolyte systems, that can give useful elements for the loss of performance due to the formation of insulating phases (zirconates).

The XCT and FIB techniques will be presented from the experimental point of view and some results will be shown. We believe that these first results are promising and open perspectives for the advancement of the investigation on cathode degradation.

Finally, the Cr deposition is investigated experimentally on modified cathodes, containing Mn-enriched YSZ as an electrolyte phase in the composite. First experiments have been done, showing that the presence of Mn can catalyze the Cr deposition via the formation of a Cr-Mn intermediate.

Some of the results exposed in this chapter have be submitted as a paper:

- G. J. Nelson, W. M. Harris, J. J. Lombardo, J. R. Jr. Izzo, W. K. S. Chiu, P. Tanasini, M. Cantoni, J. Van Herle, C. Comninellis, J. C. Andrews, Y. Liu, P. Pianetta,

and Y. S. Chu. 3D elemental mapping of the composite LSM-YSZ SOFC cathode microstructure using XCT and FIB-SEM. Submitted to Electrochemistry Communications.

6.1   3D characterization of cathode microstructure

In Chapter 4 emphasis has been put on the fact that the microstructure of a composite electrode influences deeply its performances. On the one hand, the geometry of the electrode determines the density of TPB area. On the other hand, the topology determines whether a particle belongs to a spanning cluster, making a TPB site active, but also influences the relative conductivity of the percolating networks, therefore affecting the extension of the electrochemical reaction in the cathode layer.

The characterization of the electrode microstructure was performed in Chapter 4 through analysis of SEM images and an extrapolation of 2D data to 3D quantities. Even though this procedure gave valid and interesting results, it has two main disadvantages:

- It is destructive.

- The extraction of information of a 3D structure from 2D images can lead to some artifacts and must be done carefully in order not to introduce excessive errors.

In order to avoid one or both these disadvantages, alternatives for the characterization have been found. Both the focused ion beam (FIB) and the X-ray computed tomography (XCT) techniques, whose fundamentals have been explained in Chapter 3, provide direct 3D reconstruction of the cathode volume with a resolution on the order of 10 nm. They are both capable of capturing the smallest features of the microstructure yet permit avoiding the possible artifacts coming from 2D to 3D extrapolation. XCT has the additional advantage to be non-destructive.

In the following, the results coming from the characterization of several cathode microstructures with XCT and FIB are shown, along with a comparison between the two

methods. Furthermore, EIS characterization has been carried out on the different microstructures with 3-electrodes measurements, in order to correlate the microstructure to the electrochemical performance.

X-ray computed tomography (XCT)

X-ray computed tomography (XCT)) is a nondestructive imaging method using a full-field transmission X-ray microscope to reconstruct a 3D image of a volume of porous electrode [110, 111, 112]. Measurements and image treatment have been done at the University of Connecticut, Storrs, US, within a collaboration with EPFL. During the present work, XCT imaging has been developed on LSM/YSZ cathodes, giving access to an alternative high-resolution technique for 3D reconstruction.

Sample preparation

Cathode material has been deposited on a YSZ support in the form of successively screen-printed layers, with a drying step on a hot plate at 70 °C between layers. 20 - 30 layers were deposited, for a total thickness of about 100 - 150 µm. Sintering performed at 1050 °C for 1 hour on such a thick layer caused the sintering forces to create small cracks in the cathode material. It was then possible to mechanically separate pieces of LSM/YSZ composite.

Focused ion beam (FIB) of Ga ions was then used to carve a cylindrical volume of about 10 µm diameter and 20 µm height, successively glued to the point of a pin. Few small Au clusters were sputtered on the sample to be used as reference points for image aligning.

X-ray microscope imaging

Full-field XCT measurements of the SOFC cathode were conducted at the Stanford Synchrotron Radiation Lightsource (SSRL) beamline BL6-2c, a transmission X-ray microscope (TXM) with a spacial resolution of about 38 nm. A schematic representation of the experimental setup is shown in Figure 6.1. The XCT was obtained by rotating the sample
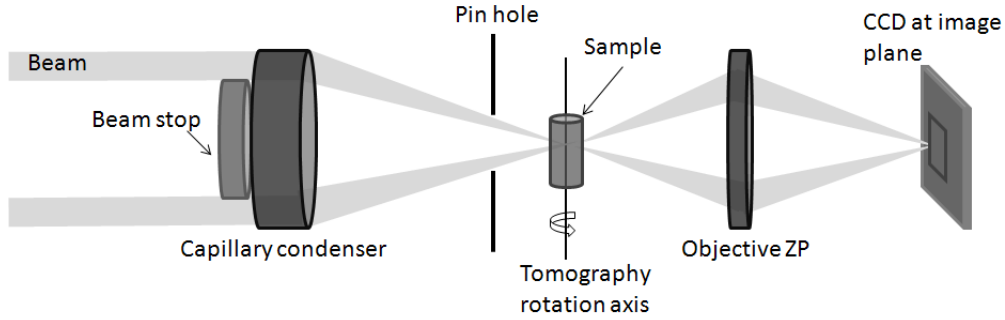
Figure 6.1. Schematic of the full-field XTM used for XCT imaging. The monochromatic X-rays coming from the synchrotron are focused on the sample and the transmitted beam is magnified by a Au Fresnel lens on a CCD detector.

and collecting a series of 2D absorption contrast images, and recombining them in a 3D stack. In order to permit the identification of the different phases, a differential absorption contrast technique was used, that means the adsorption images were taken using X-rays slightly above and below the Mn K-edge (6.54 keV) [113] . Images obtained "below edge" presented an accentuated contrast between the pores and the dense phases, while images obtained "above edge", thanks to the absorption of the Mn, permitted the contrast between the Mn-rich LSM phase and the rest of the sample.

Image treatment

The data obtained from the TXM, for easier manipulation, were first reduced in size by a binning process, i.e. by replacing pixels within a certain interval of gray level with the central value of the interval. The 3D matrix of voxels was then subdivided in 2D slices stacked along the rotational axis of the sample. The stacks were converted into 8-bit grayscale, then a 3σ Gaussian blur filter was applied to remove pixilation and enhance the contrast; moreover, a maximum-likehood expectation maximization (MLEM) algorithm [114] was used to enhance contrast between LSM and YSZ phases. Finally, each tomographic image was cropped to generate a representative volume element (RVE).

The "above edge" and "below edge" stacks were then aligned and overlapped using common points of reference. A cropping of a selected region was isolated for the study of

the morphology, eliminating possible edges or other defects. Thresholds were applied for reducing the 8-bit grayscale stacks to binary representations, identifying the LSM-other regions from the above edge stack, and the pore-other regions from the below edge stack. Finally, the YSZ regions were obtained by the overlapping of the two binary stacks. The result of the image processing is a 3D matrix of voxels where phases are represented with unique integers (e.g. pores: 0, LSM: 1, and YSZ: 2).

Focused ion beam (FIB) nanotomography

SEM imaging coupled to the focused ion beam (FIB) technique permitted the 2D imaging of successively carved slices of the studied material. The recomposition of the images of the stack brought to a 3D reconstruction. FIB nanotomography was performed in the CIME department at EPFL.

Sample preparation

Pieces of cathode material were prepared and impregnated with resin in the same way described in section 3.4.2. Resin pellets were cut with a diamond saw (Well, Switzerland) to have two exposed surfaces of cathode material at approximately 80° angle. Polishing was performed on both surfaces with diamond lapping films down to 0.1 µm, with water as cooling and lubrication medium. A gold coating of about 600 nm was sputtered on the sample surface for extraction of charge during imaging.

As a last step, a protective carbon layer of about 1 µm thickness was deposited on the worn surface by ion beam induced deposition, in order to avoid the formation of a rounded edge during slicing.

Imaging conditions

Serial sectioning is an alternating procedure in which the uppermost layer from the sample is eroded with an ion beam exposing the underneath section, which is then polished with the same ion beam. The newly exposed surface is then imaged with SEM.

For our SOFC cathode samples, a volume of the dimensions of about 5x5x5 μm^3 was sliced every 10 nm; a gallium liquid metal ion source was used to mill and polish the sections. Cross beam microscopy allowed SEM imaging during milling and polishing. Figure 6.2 shows the schematic of the slicing process, while Figure 6.3 shows the sample at the end of the slicing and the location of the imaging area. Scanning electron microscope (Zeiss NVision 40 Crossbeam) equipped with a Schottky field emission gun (0.1 − 30 kV), a Gemini column and energy selective back-scattered secondary electron (EsBSE) detector was used for imaging the samples, with an incident angle of 52°. Images were taken with 10 nm of lateral definition i.e. the pixels of each image had a dimension of 10x10 nm^2. The slicing-imaging process was automatically done overnight; every slice took approximately 30 s, so that the processing of the whole volume took 4 to 5 hours. Slow scan permitted to maximize the signal-to-noise ratio. The optimal conditions to differentiate the LSM and the zirconia phases using the EsBSE detector were an accelerating voltage of 1.87 kV and slow scan (Fig. 6.4). The volume of interaction is very small in these conditions, even in the resin phase, so that the lateral definition was very high. The EsB detector with energy filtering allowed the contrast between the two phases.

3D reconstruction

First of all, it was necessary to shrink the SEM images in order to compensate for the deformation given by the incident angle of the SEM beam; the correction factor is sin(52°). Then the slices were put in sequence using Fiji, an Open Source image processing package based on ImageJ, and a volume constituted by voxels with 10x10x10 nm^3 dimensions was obtained. Using a automatic comparison tool, the images were shifted in order to compensate for drift occurred to the sample during the measurement. The obtained volume can be deformed as a result of this alignment; in that case, a proper cuboid sub-volume was cropped for further data processing. Anomalous regions (edges, defects, zones with low contrast) were also eliminated during cropping.

Image treatment involved the application of filters (gaussian filter for a better rendering and/or sharpening filters), and successively the histogram of gray levels was thresholded for
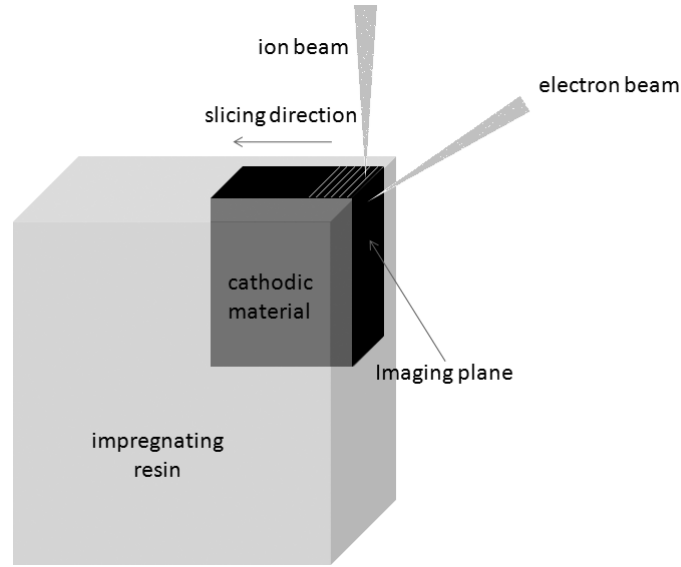
Figure 6.2. Schematic representation of the beam configuration during FIB slicing and SEM imaging of an impregnated sample. The incident angle of the electron beam for the SEM imaging was 52° with respect to the surface to be imaged.
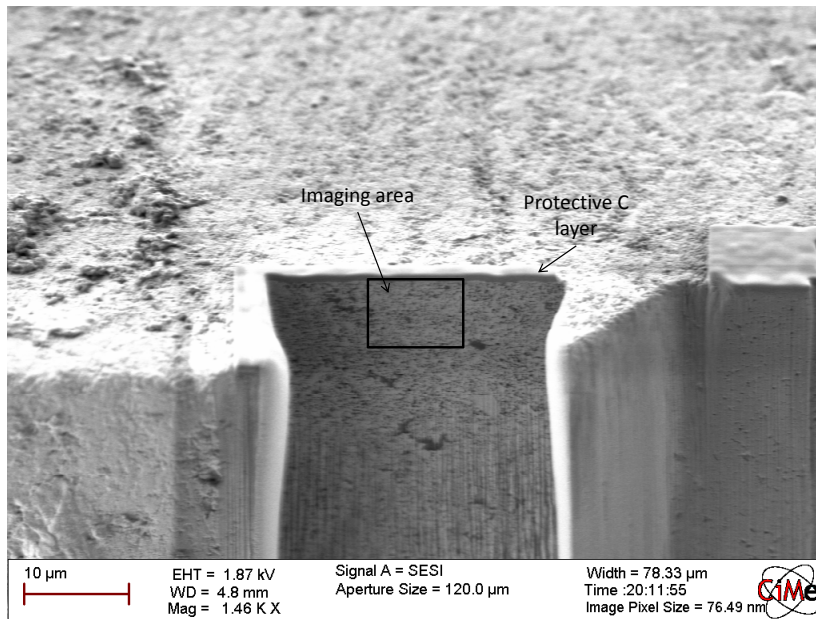
Figure 6.3. Sample after FIB slicing. It is possible to observe the cavity obtained by serial slicing. In order to avoid fringes ("curtain effect") the imaging area is near to the C protection layer. Furthermore, the slicing cuts a surface approximately three times wider that the imaging zone, to avoid shadowing by the lateral walls.
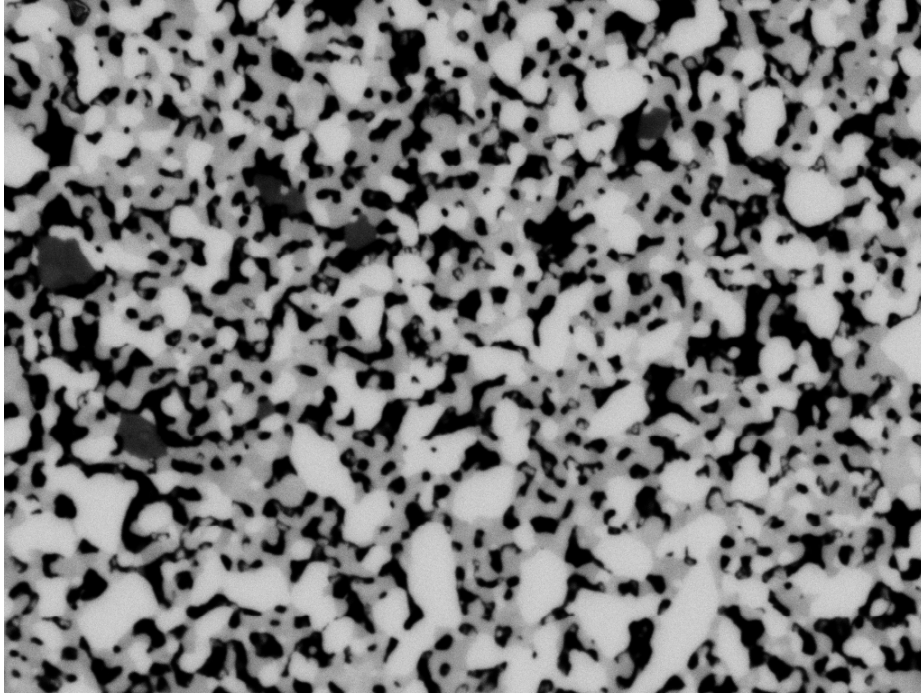
Figure 6.4. SEM image of a slice, with contrast identifying the three phases present: white: LSM, light gray: YSZ, dark gray: pores

the separation of phases. In the specific case, the darkest level of gray was assigned to the pore phase, while the lighter voxels were assigned to the LSM phase. The remaining voxels, characterized by intermediate gray levels, were attributed to the YSZ phase. Another operation of image processing was necessary, since the boundaries between pore and LSM zones presented necessarily a gradient containing all the intermediate gray levels, so were automatically considered as a small stripe of YSZ separating the LSM grain from the pore. This artifact was eliminated using a filter present in Fiji to detect steep gradients and by attributing these zones equally to the LSM and pore volumes. Figure 6.5 shows as an example the reconstruction of the LSM phase; for clarity purpose, YSZ and pores are not represented.

The ternary voxel data represents the basis for the subsequent computational 3D analysis: parameters like the volume fractions, exposed surface areas (LSM/pore and YSZ/pore
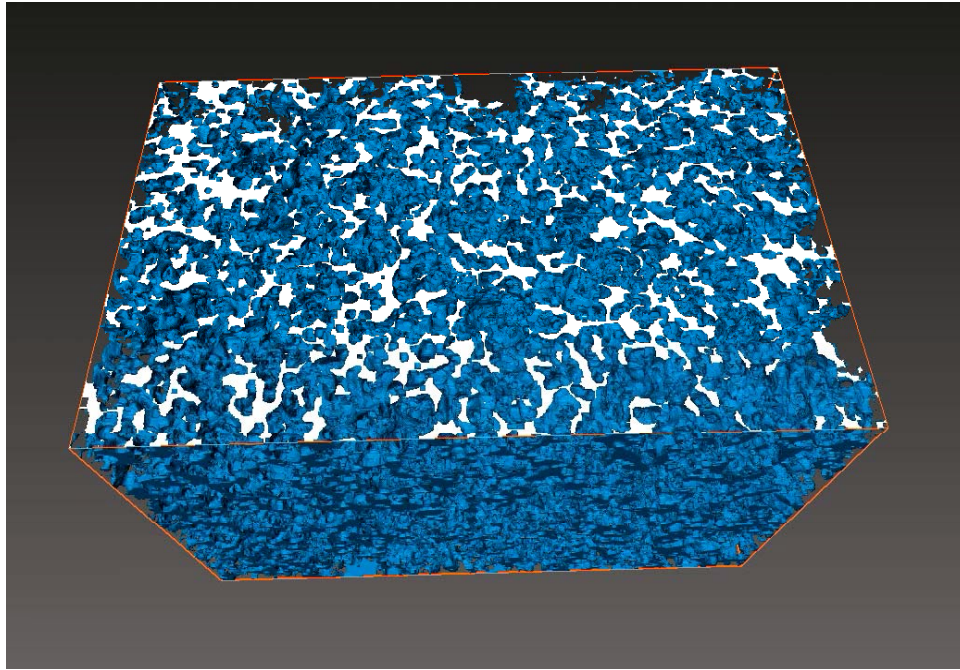
Figure 6.5. 3D reconstruction of the LSM phase; YSZ and pores are not represented. The white color indicates the 2D LSM zones in the uppermost slice

interfaces), contact area (LSM/YSZ interface), TPB lenght (LSM/YSZ/pore boundaries) can be extracted.

Comparison between XCT and FIB

The final product of the segmentation and thresholding process is a digitized version of the representative volume element (RVE) that delineates the LSM, YSZ, and pore phases with unique integer identifiers. This form facilitates the computational characterization of the microstructure including phase sizes, volume fraction, two phase interfacial area, triple phase boundary length, and phase contiguity. This characterization provides a means of quantitatively comparing the results of the XCT and FIB-SEM measurements.

Initial comparisons of the XCT and FIB-SEM imaging results were conducted in terms of the phase size distributions (PSD) predicted from images produced by each method. The phase size distributions were calculated using a ray-shooting routine based on a three-dimensional Lattice Boltzmann method (LBM) formalism using 19 lattice directions (D3Q19) [112]. Individual voxels in the 3D image were treated as grid points, with rays originating from each point in 18 directions corresponding to the non-zero lattice velocities. The characterization routine involves an iterative search of the volume that identifies interfaces containing the phase of interest followed by the propagation and tracking of rays from these interfaces. The rays terminate upon reaching a second interface of the phase of interest, and the length of each ray is tabulated and later analyzed to determine the phase size distribution. The resulting phase size distribution provides a histogram outlining the number of rays of a given length seen in each phase. The discrete distribution of rays is then recast in terms of the volumetric contribution specific phase diameters make to the overall phase volume. Further details outlining this approach are provided by Grew et al. [112]. In addition to generating a discrete PSD, a cumulative size distribution (CSD) is also calculated, providing a continuous function that describes the size of microstructural features. This continuous form enables mathematical operation on a set of size distributions. In particular, the mean phase size distributions for the XCT results were estimated by the averaging and subsequent numerical differentiation of the CSD data from two RVEs.

The calculated phase size distributions for the XCT and FIB-SEM images are shown in Figure 6.6. The solid lines in each plot represent the mean PSD calculated from data taken from two separate XCT sub-volumes of size 5^3 μm^3. Note that a smaller example volume, taken from the larger 5^3 μm^3 volume, is shown in Figure 6.6 a. strictly for illustration purposes. The symbols represent the PSD calculated from a single FIB-SEM sub-volume of size 3.5^3 μm^3. The predicted size distributions match quite well, particularly considering that the imaged samples were taken from distinct locations within bulk cathode.

Further comparison of the XCT and FIB-SEM images were made with respect to volume fraction, two phase interfacial area, triple phase boundary length,and phase conti-
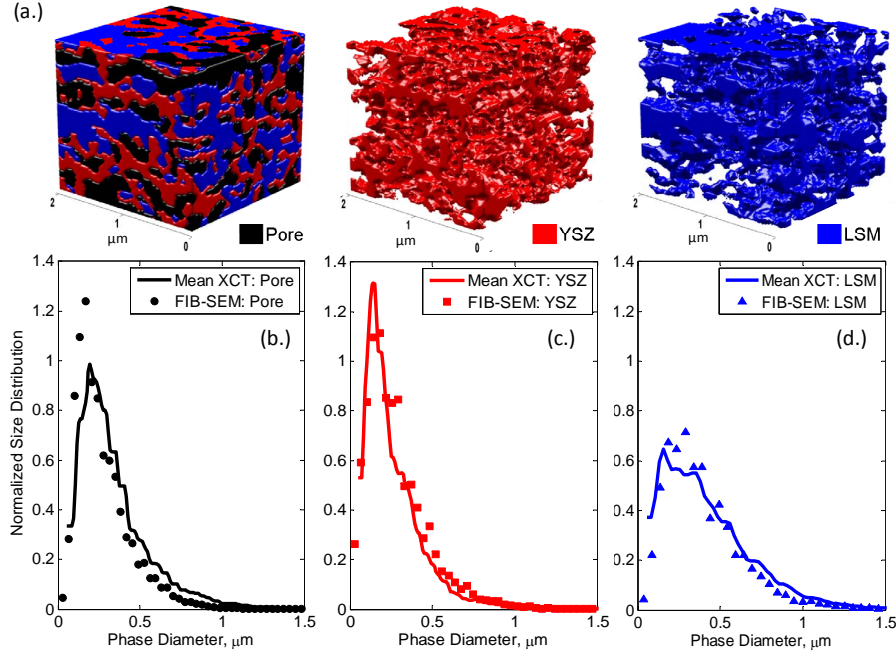
Figure 6.6. Digitized composite, YSZ, and LSM structures obtained from the reconstructed XCT (a.) and FIB-SEM (not shown) images can be analyzed and compared using microstructural characterization routines. Phase size distributions for the (b.) pore, (c.) YSZ, and (d.) LSM phases of a solid oxide fuel cell cathode estimated from XCT (solid lines) and FIB-SEM (symbols) provide comparable assessments of the microstructure. The distributions shown are for distinct samples taken from the same cathode, with the XCT distributions representing the mean of two separate subvolumes.

guity. These parameters can be readily determined from straightforward search algorithms used to analyze the digitized structure produced from the image processing steps [111]. The results of this analysis are outlined in Table 6.1. For the XCT images average values were computed for two RVEs segmented from the full sample image stack. The data for the FIB-SEM RVE was down-sampled using 3×3×3 binning, which produced a 3D image with an effective resolution of 30 nm. Close agreement is seen for most of the parameters investigated, with the exception of the LSM contiguity value. It is possible that this difference in contiguity is related to the difference in resolution of the imaging approaches. However, further investigation is needed to better understand the effects of

Parameters and Phases	Mean XCT		FIB-SEM (Down-sampled)	
Mean Phase Diameter (µm)				
Pore	0.34 (±0.025)		0.27 (±0.03)	
YSZ	0.27 (±0.025)		0.28 (±0.03)	
LSM	0.42 (±0.025)		0.40 (±0.03)	
Vol. Fraction				
Pore	0.3388		0.3410	
YSZ	0.3254		0.3260	
LSM	0.3358		0.3330	
Contiguity (%)				
Pore	99.65		99.80	
YSZ	99.85		99.40	
LSM	98.25		94.30	
Interfacial Characteristics	Total	Effective	Total	Effective
TPB Length (m m^{-3})	6.61E+13	5.98E+13	8.30E+13	7.01E+13
Interfacial Area (m m^{-2})				
Pore-YSZ	7.68E+06	7.58E+06	7.45E+06	7.32E+06
Pore-LSM	2.92E+06	2.74E+06	3.40E+06	3.12E+06
YSZ-LSM	6.42E+06	6.09E+06	5.66E+06	4.89E+06

Table 6.1. Microstructural characterization results for the cathode samples imaged using XCT and FIB-SEM. The FIB-SEM results were down-sampled using 3×3×3 binning to allow comparison of measurements at comparable spatial resolutions.

imaging resolution on microstructural characterization results.

Conclusions

In conclusion, microstructural characterization of an SOFC cathode based on XCT and FIB is compared for each these techniques with general agreement found between predictions of phase size distributions and key microstructural parameters. The effects of instrument resolution on microstructural characterization were primarily evident in predictions of phase contiguity. The agreement found in the results presented demonstrates the viability of XCT as a characterization technique and provide key insights into the SOFC cathode microstructure.

6.2 Reactivity study on LSM/electrolyte systems

X-ray diffraction technique allows identifying and quantifying the presence of a foreign phase resulting from the reaction between SOFC components. In particular, it is a useful

tool to study phase compatibility between perovskites such as LSM and electrolytes such as YSZ, ScSZ or GDC, permitting the identification of products of interfacial reaction (e. g. zirconates of La or Sr) that can form with time due to inter-diffusion at operating temperature.

However, in state-of-the-art systems, zirconates often appear in very limited amounts and are confined to the YSZ-LSM interfaces, reaching less than 1% of the total volume. In this case, standard software-based XRD analysis is often unable to detect the product of the interfacial reaction; on the other hand, it is important to find a technological solution for lowering the detection limit since a limited yet localized formation of insulating phases can have a non negligible effect on the electrode performance. One possible solution is the preparation of TEM lamellae containing an interface, but the extension of the sample is too limited to be representative. Therefore, we chose to perform XRD measurements, followed by Rietveld analysis, which has a higher sensitivity and permit to analyze a representative volume of the sample.

XRD measurements were performed both at EPFL and at Universidad del País Vasco, Bilbao, Spain. Rietveld data analysis was performed at the Universidad del País Vasco.

Sample preparation

Cylindrical pellets of pure materials (LSM, YSZ, ScSZ, GDC) or couples LSM-electrolyte were fabricated in a uni-axial press (P. Weber, Germany), using a 8 mm diameter die and pressing at 10 kN for 1 minute. Powders mixtures, composed of 50% by weight of each phase, had been previously homogenized by planetary ball milling (Fritsch, Germany) in dry conditions at 200 rpm for 2 hours, in presence of zirconia spheres. Thermal treatments were performed in a furnace (Rohde, Germany), placing the pellets in alumina crucibles for different times (1 to 1900 hours) and temperatures (850 °C to 1300 °C), using 5 °C min^{-1} heating speed.

XRD measurement conditions at EPFL

X-ray powder diffraction was recorded at room temperature, using a PHILIPS X'PERT automatic diffractometer, equipped with a Cu-Kα radiation tube (λ = 1.5418 Å). The software X'PERT High Score Plus was used for the automatic identification of spectra. The power generator has been provided at 40 kV and 50 mA. The patterns were recorded in 2ϑ steps of 0.017° in the 10–89° range, counting for 40 s per step.

XRD measurement conditions at Universidad del País Vasco

In situ variable-temperature X-ray diffraction data were collected using a Bruker AXS D8 Advance diffractometer equipped with a Cu-Kα radiation tube (λ = 1.5418 Å), a Vantec-1 PSD. The patterns were recorded in 2ϑ steps of 0.02° in the 19–91° range, counting for 1 s per step.

Rietveld analysis

Some spectra were submitted to Rietveld analysis. Preliminary identification of the initial oxides and the formation of new phases were evaluated using the Powder Diffraction File (PDF) database. In all the cases, the deconvolution of the initial two diffraction maxima provides an indication of the number of phases present in each XRD diagram. This procedure was carried out using the peak-fit option of the WinPLOTR program without structural model. The simulated profiles were then used to recalculate the starting unit cell parameters from the 2ϑ peak positions.

Once the present phases were identified and the starting unit cell parameters were obtained, the Rietveld method allowed the quantitative analysis of each individual phase observed for each XRD pattern at different processing temperatures and times.

Results

Effect of sintering

A first series of samples had been produced from $(La_{0.75}Sr_{0.25})_{0.95}MnO_{3\pm\delta}$ (LSM25) and 8% Y_2O_3 - 92% ZrO_2 (8YSZ), 10% Sc_2O_3 - 1% CeO_2 - 89% ZrO_2 (Praxair, US, indicated as 10ScSZ) or gadolina-doped ceria 10% Gd_2O_3 - 90% CeO_2 (Nextech Material, US, indicated as 10GDC). Each couple LSM-electrolyte has been checked with XRD analysis after three different treatments: compressed pellet, sintered pellet (1100°C, 1 h) and aged pellet. The aging process has been performed exposing a *sintered pellet* for 1900 h at cell operation temperature (850°C) in air. In all cases no foreign phase formation was identified by standard XRD analysis in EPFL, which did not include Rietveld analysis. Since the software-based analysis has a detection limit of about 1%, it is possible that small amounts of zirconates at the interface were present but not detected.

Nevertheless, it was possible to observe a change occurred during high-temperature treatment in the powder: an evident peak thinning showed that the sintering process increases the crystallite size in the powders. Most of the variation occurred during sintering, and further increase during aging was negligible.

Effect of the LSM and electrolyte composition

A second series has been produced using $(La_{0.70}Sr_{0.20})_{0.90}MnO_{3\pm\delta}$ (LSM30) and one between 8YSZ, 10ScSZ, 10CGO. The A-site deficiency and La/Sr ratio for this cathode were optimized in order to hinder the formation of zirconates, with respect to the previous series; the average particle diameter was $\sim$ 0.3 μm. Each couple LSM-electrolyte has been checked with standard XRD analysis in EPFL after three different treatments: sintered pellet (1100°C, 1 h), aged at 1000°C and aged at 1100°C. The aging processes have been performed exposing a *sintered pellet* for 100 h at the chosen temperature. Two of these samples have in addition been prepared and analyzed by TEM: the mixture LSM30-10ScSZ, aged 100 h at 1100°C, and the mixture LSM30-8YSZ, aged 100 h at 1000°C. In both cases, no zirconates were found in the small volume of the TEM lamellae examined.

Further treatment of the XRD data was performed through Rietveld analysis within a collaboration with the University of Bilbao. When conducting detailed phase analysis of XRD spectra using Rietveld refinement on the reaction couples, secondary phases could be identified (analyses performed by Dr. Aitor Larrañaga). The analyzed sample volume by XRD is more representative than for TEM analysis where only a minute volume is studied. The Rietveld refinement was conducted on the data obtained with both LSM25 and LSM30 mixed with the 3 electrolyte powders (8YSZ, 10ScSZ, 10GDC). Figures 6.7 - 6.9 show the phases identified with this method.

The formation of foreign phases deriving from the reaction of Sr with the electrolyte has been quantified. From these results it is possible to say that LSM30, with 10% A-site deficiency, appears to be more stable than LSM25 (only 5% A-site deficient) since the latter, sintered 1 hour with the ScSZ, show formation of Sr zirconate, while the former needs to be aged 100 hours at 1100°C to shows formation of zirconates and even 100 hours of aging at 1000°C don't lead to an observable reaction. This could be explained by the fact that, even if the increase of Sr increases the reactivity of $SrO_{(LSM)}$, pushing towards the formation of Sr zirconates, the increase in A-site deficiency compensates this effect.

A second observation is that LSM-8YSZ samples show a higher formation of zirconates in all cases than LSM-10ScSZ (e.g. 2.1% $SrZrO_3$ after 100 h at 1100°C for the former, while 1.4% for the latter in the same conditions). As a final remark, it must be added that the detection of Mn_3O_4 (LSM25 samples) has been explained by the presence of a Si-based contaminant, probably introduced during sample preparation.

Conclusions

Rietveld analysis on XRD data has proved to be a very effective method to investigate the formation of foreign phases present in amounts of the order of 1% (w/w). From the first results obtained, it has been possible to confirm the higher stability of LSM30 and ScSZ with respect to LSM25 and of YSZ respectively.
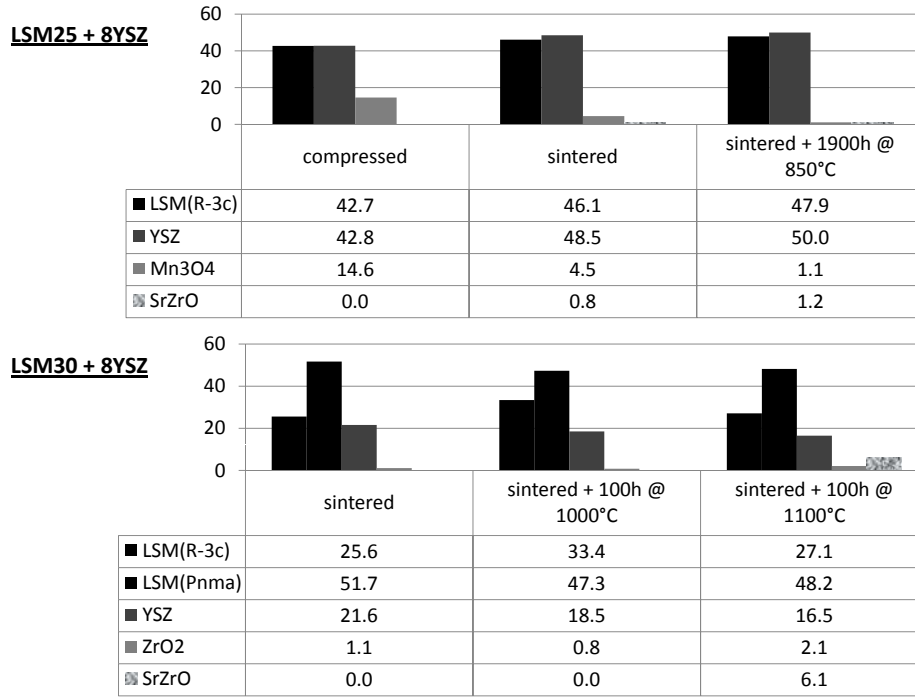
LSM25 + 8YSZ	compressed	sintered	sintered + 1900h @ 850°C
■ LSM(R-3c)	42.7	46.1	47.9
■ YSZ	42.8	48.5	50.0
■ Mn3O4	14.6	4.5	1.1
▨ SrZrO	0.0	0.8	1.2

LSM30 + 8YSZ	sintered	sintered + 100h @ 1000°C	sintered + 100h @ 1100°C
■ LSM(R-3c)	25.6	33.4	27.1
■ LSM(Pnma)	51.7	47.3	48.2
■ YSZ	21.6	18.5	16.5
■ ZrO2	1.1	0.8	2.1
▨ SrZrO	0.0	0.0	6.1

Figure 6.7. phase proportion obtained with XRD-Rietveld refinement on LSM25/YSZ and LSM30/YSZ samples for the identification of the formation of La/Sr zirconates. LSM30 samples present two different crystallographic structures of LSM, stabilized by the higher A-site deficiency.

6.3   Effect of the presence of Mn

The multicathode cell already presented in Section 3.1.3 has been operated in a long-term test in presence of a Cr source, namely the Cr-containing test-rig tubular pipes for air feeding and test flanges (made of Inconel 602). The four cathodes containing LSM and Mn-enriched YSZ composite cathodes have been tested at 850 °C in 7% humidified H_2 at 0.6 A/cm^2 for about 800 hours.

Figure 6.10 presents the temporal evolution of cell voltage of the four segments during operation. The performance loss is severe for all the cells containing Mn-enriched YSZ, reaching 15%/1000 h of voltage decay in the worse case, which is a degradation rate much higher than the one obtained for standard LSM/YSZ cells in presence of Cr (Section 5.2)

This was rather unexpected since manganese, in theory, should have a beneficial effect
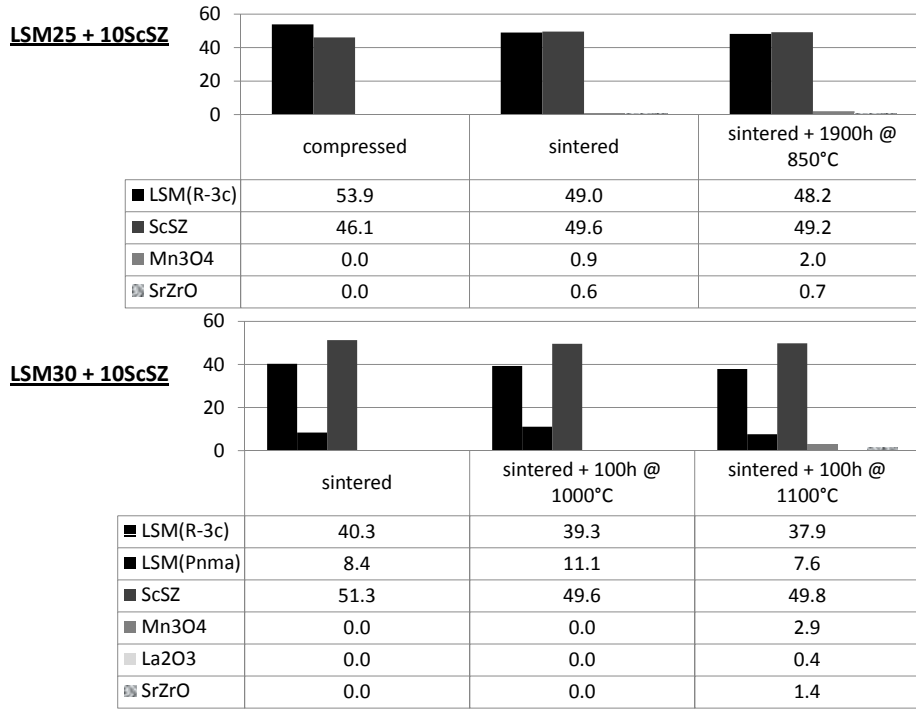
LSM25 + 10ScSZ

	compressed	sintered	sintered + 1900h @ 850°C
■ LSM(R-3c)	53.9	49.0	48.2
■ ScSZ	46.1	49.6	49.2
■ Mn3O4	0.0	0.9	2.0
▨ SrZrO	0.0	0.6	0.7

LSM30 + 10ScSZ

	sintered	sintered + 100h @ 1000°C	sintered + 100h @ 1100°C
■ LSM(R-3c)	40.3	39.3	37.9
■ LSM(Pnma)	8.4	11.1	7.6
■ ScSZ	51.3	49.6	49.8
■ Mn3O4	0.0	0.0	2.9
La2O3	0.0	0.0	0.4
▨ SrZrO	0.0	0.0	1.4

Figure 6.8. phase proportion obtained with XRD-Rietveld refinement on LSM25/ScSZ and LSM30/ScSZ samples for the identification of the formation of La/Sr zirconates. LSM30 samples present two different crystallographic structures of LSM, stabilized by the higher A-site deficiency.

on cell performance and degradation. Indeed, Widmer [93] reports that grains of Mn at the TPB can have a catalytic effect on the ORR thus increasing the cell performance. On the other hand, several authors reported that Mn depletion of the LSM can bring to instability and reaction between LSM and YSZ, forming insulating phases such as Sr and La zirconates [37, 34]. Mn is soluble in YSZ at high temperature up to several molar percent at operating temperature [46], and the electrolyte phase can therefore act as a "well" for Mn, causing depletion in the neighboring LSM, leading to undesired reactions. The pre-introduction of Mn in the YSZ phase was supposed to hinder the Mn depletion of LSM by reducing the driving force for Mn diffusion towards YSZ, therefore avoiding or retarding the formation of zirconates.

Starting from this point, we were expecting the addition of Mn to yield more stable
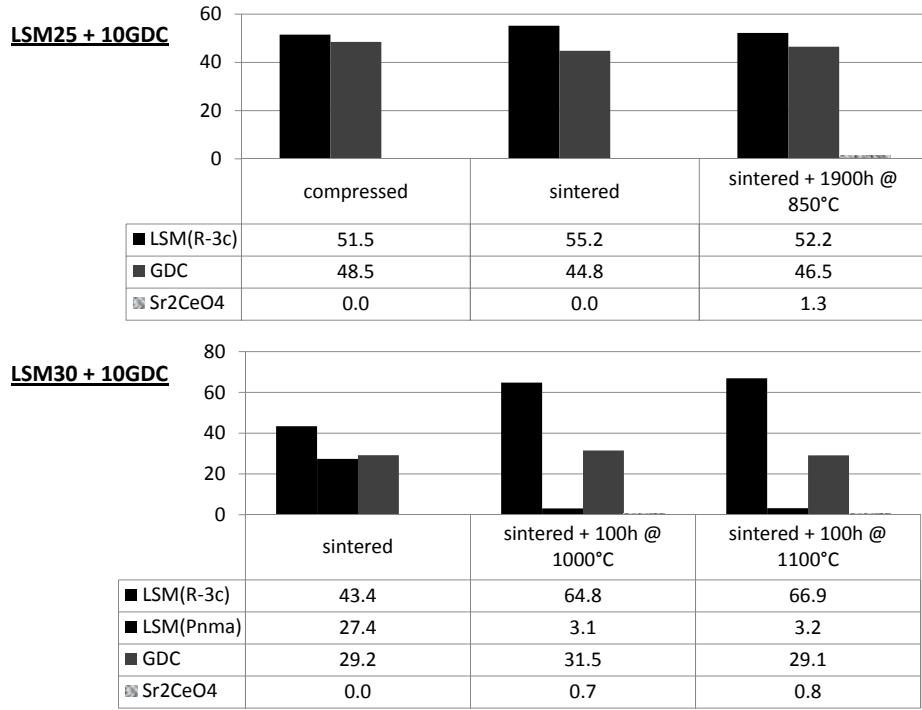
Figure 6.9. phase proportion obtained with XRD-Rietveld refinement on LSM25/GDC and LSM30/GDC samples for the identification of the formation of La/Sr ceriates. LSM30 samples present two different crystallographic structures of LSM, stabilized by the higher A-site deficiency.

electrodes; on the contrary, the observed behavior suggests that in the studied conditions the presence of Mn is detrimental. Indeed, Cr quantification on the cross-section of the segments after operation shows very high contents of Cr in the active layer, as shown in Figure 6.11, suggesting Mn to increase the deposition rate of Cr in the active layer.

From a modeling point of view, this corresponds to an increase of the $i_{o,\mathrm{Cr}}$ parameter in Eq. 5.4, i.e. the increase of the exchange current density for the reaction of reduction of $CrO_2\left(OH\right)_{2(\mathrm{g})}$. According to Eq. 5.4, the Cr deposition rate is expected to scale linearly with $i_{o,\mathrm{Cr}}$. The Cr deposition in Figure 6.11 is 2 to 5 times higher than for the Mn-free reference cell Cat1, we can thus roughly estimate that the value of $i_{o,\mathrm{Cr}}$ was increased accordingly by the presence of Mn.

The catalytic effect of Mn oxide in SOFC cathodes has already been reported for the
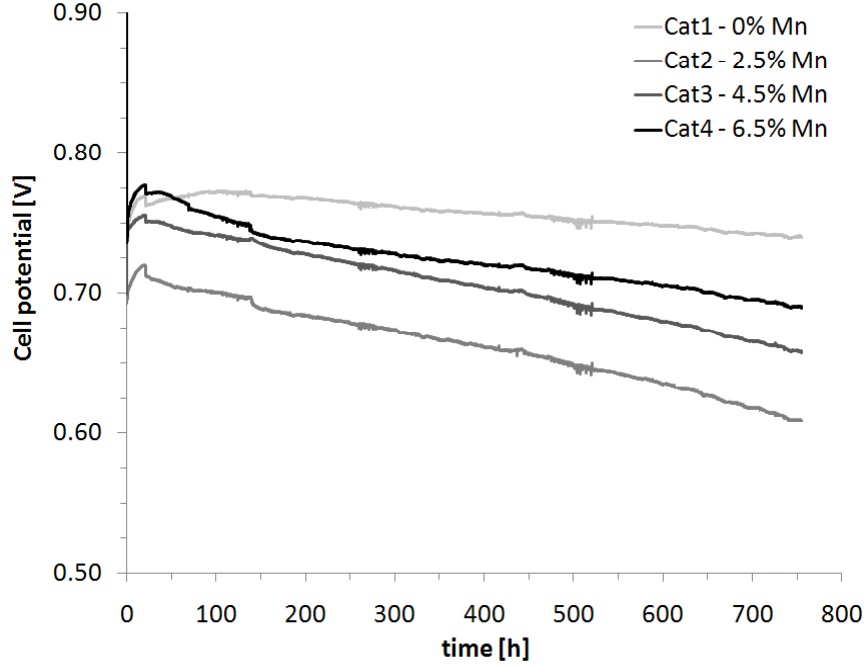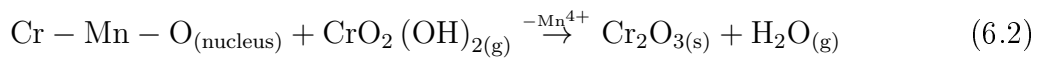
Figure 6.10. Potential during operation of LSM/Mn-enriched YSZ segments. All segments containing Mn show a strong deactivation: Mn appears to have a detrimental effect.

ORR [46, 93], it is logical to assume that the presence of Mn either as a solid precipitate near the LSM/YSZ interface or as a nucleus on the YSZ surface near the TPB can accelerate the reduction of volatile Cr species. This hypothesis agrees with the mechanism proposed by Jiang et al. [33] for Cr reduction through the formation of a Cr-Mn intermediate under the cathodic polarization of LSM electrodes. Adapting the mechanism proposed in [33] to our system we obtain:

$$\mathrm{CrO_2\,(OH)_{2(g)}} \xrightarrow{\mathrm{Mn^{2+}}} \mathrm{Cr-Mn-O_{(nucleus)}} + \mathrm{H_2O_{(g)}} \tag{6.1}$$

$$\mathrm{Cr-Mn-O_{(nucleus)}} + \mathrm{CrO_2\,(OH)_{2(g)}} \xrightarrow{-\mathrm{Mn^{4+}}} \mathrm{Cr_2O_{3(s)}} + \mathrm{H_2O_{(g)}} \tag{6.2}$$
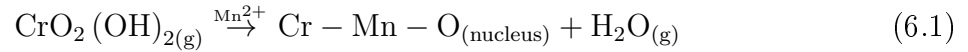
Eq. 6.1 and 6.2, combined and balanced, give the overall reaction:

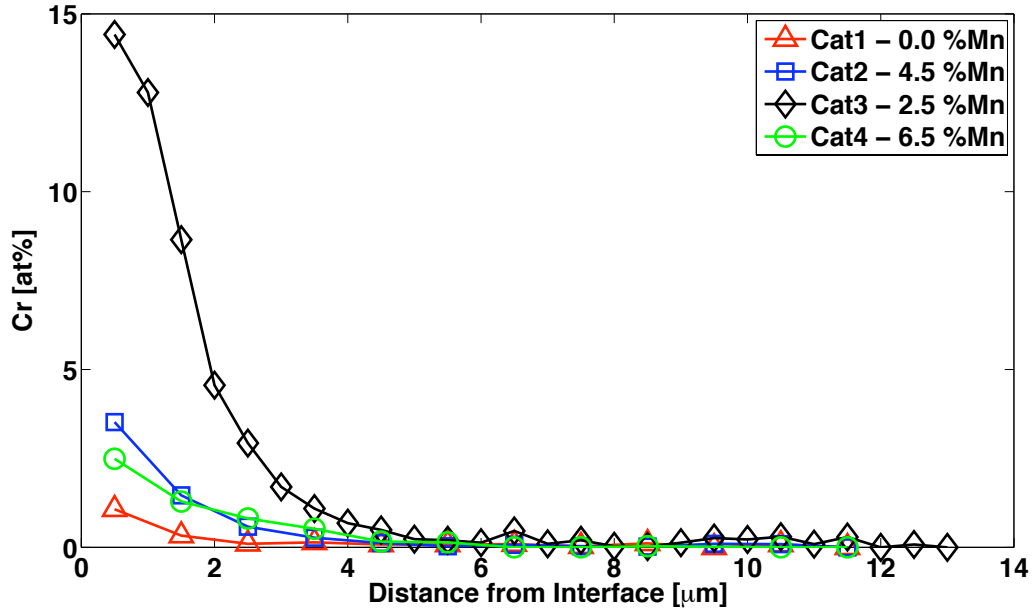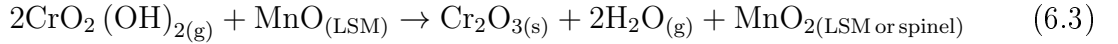**Figure 6.11.** Cr concentration profiles in cathodes with Mn-enriched YSZ after 800 h of operation. Cells containing Mn in the YSZ phase of the composite show Cr contents 2 to 5 times higher than standard LSM/YSZ electrodes such as cell Cat1 or cells investigated in Section 5.2.

$$2CrO_2(OH)_{2(g)} + MnO_{(LSM)} \rightarrow Cr_2O_{3(s)} + 2H_2O_{(g)} + MnO_{2(LSM\,or\,spinel)} \qquad (6.3)$$

The Mn^{4+} formed, represented in its oxide form in Eq. 6.3, can be then either consumed by $Cr_2O_{3(s)}$ to form (Cr,Mn) spinel crystals, or remain in the LSM and eventually be regenerated by electrochemical reduction, under the cathode polarization:

$$Mn^{4+}_{(LSM)} - O + V_{\ddot{O}} + 2e^-_{LSM} \rightleftharpoons Mn^{2+}_{(LSM)} + O^{2-} \qquad (6.4)$$
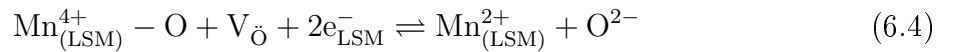
The mechanism presented in Reaction 6.4 would regenerate the Mn^{2+} site for the iteration of Reaction 6.1.

In all cases, the results presented suggest that the use of Mn as a "stabilizer" for the LSM/YSZ interface is inappropriate and detrimental in the case of cells operating in presence of Cr contaminants, leading to important Cr deposition.

Further microscopic analyses permitted to investigate the effect of a heavy contamination of Cr, unusual for standard LSM/YSZ electrodes. SEM images taken near the cathode/electrolyte interface (Fig. 6.12), show that the formation of large amounts of Cr-rich phases causes the consumption of LSM, probably by migration of cations into the Cr-rich phases.

Cell Cat3, containing YSZ with 2.5% Mn and a finer microstructure (see Section 3.1.3), presents loss of contact of a significant part of the cathode/electrolyte interface (Fig. 6.13) and severe Cr poisoning under the studied conditions. We believe that the current constriction in the still contacted part of the cathode leads to higher local overpotential and accelerates all degradation processes, including Cr deposition. In effect, Figure 6.10 shows that, especially for Cell Cat3, the degradation accelerates towards the end of the test and the amount of Cr detected is abnormally high with respect to the other cells, despite the lower amount of Mn.

In summary, the results obtained support the mechanism of the Cr deposition through the formation of a Cr-Mn intermediate as a possible reaction path. This is interesting from a technological point of view, considered the presence of Mn in LSM-based cathodes and especially the frequent use of A-site deficient perovskite (therefore rich in Mn oxide) for avoiding zirconate formation. In effect, the increased Cr contamination rate caused by the presence of Mn rises a conflict between the optimization of the LSM composition for getting phase stability and the technological need for the robustness towards contamination in real operating conditions, where Cr is present.

However, we believe that the two paths Eq. 5.3 and 6.1-6.4 may coexist, and that the first is not necessarily disproved by evidences justifying the second. Results obtained with a different system can give a deeper insight of the phenomenon. In effect, nickelate-based electrodes were recently tested by A.J. Schuler and H. Lübbe at EPFL [115] in presence of Cr contamination. This material is a catalyst for the ORR and a mixed electronic-ionic conductor, therefore the electrochemical reaction is much more distributed inside the porous electrode. After operation, Cr oxide species were found distributed in the whole electrode volume, as shown in Figure 6.14, in complete absence of Mn. This evidence
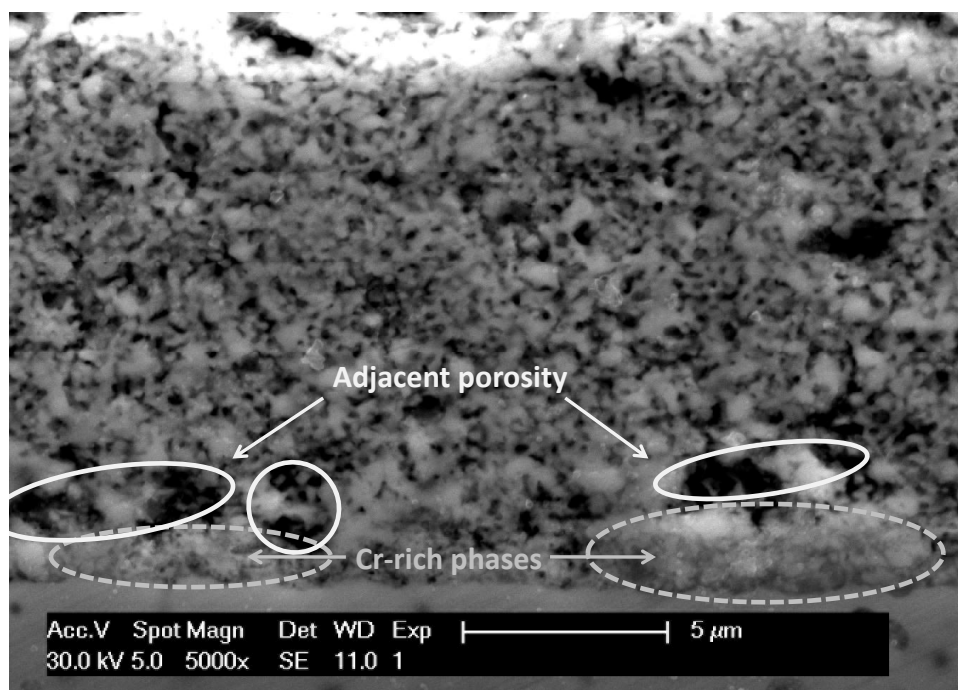
Figure 6.12. SEM image of cell Cat3 (2.5% Mn) after severe Cr contamination. Near the dense electrolyte it is possible to see large agglomerates of Cr-rich phases (presence confirmed by EDX) and, immediately above, an increase in porosity due to the consumption of LSM phase.

shows once again that the Cr deposition is strictly related to the electrochemical activity; reversing the logic, we could actually say that the presence of deposited Cr is an indicator of electrochemical activity. Moreover, for this specific system we can exclude the Mn-intermediate mechanism, and we can therefore suppose that the deposition is occurring by direct electrochemical deposition alone.

In conclusion, from these experimental evidences concerning the mechanism of Cr deposition in LSM-based electrodes we concluded that the model proposed by Jiang et al. [33] is likely to be correct and that the Cr is deposited via a Mn-Cr intermediate. As a direct consequence, we believe - on the basis of our experimental results - that Mn-rich electrodes are more prone to undergo heavy Cr degradation and that the introduction of extra Mn in the electrode, commonly used for reducing the reactivity of LSM towards the
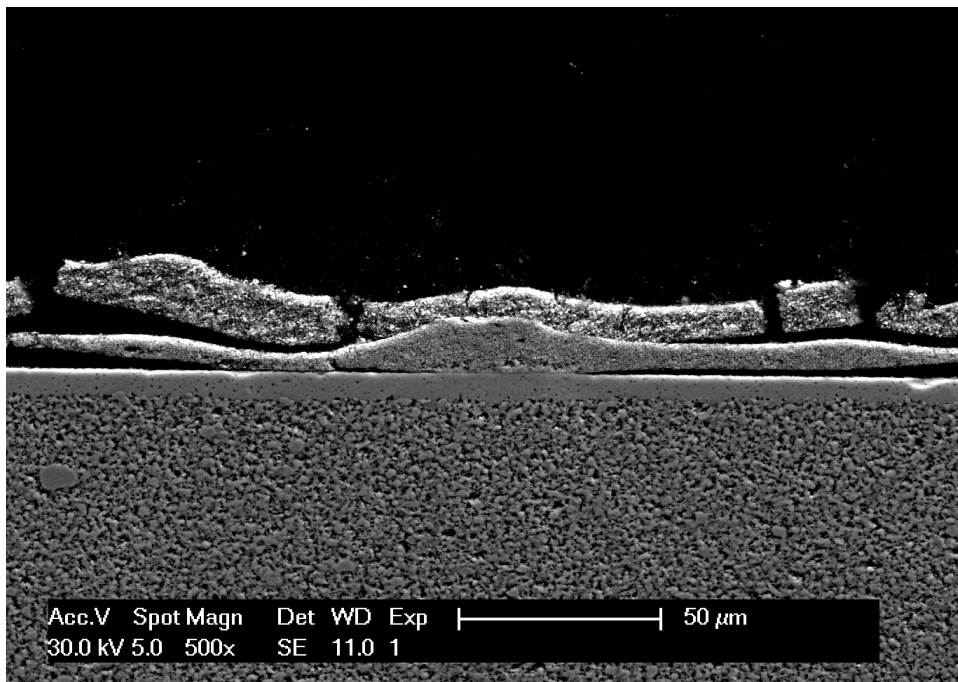
Figure 6.13. Cell Cat2, after 800 h of operation under severe Cr degradation shows wide zones of delaminated cathode.

zirconia, can have a detrimental effect in case of presence of Cr volatile species.
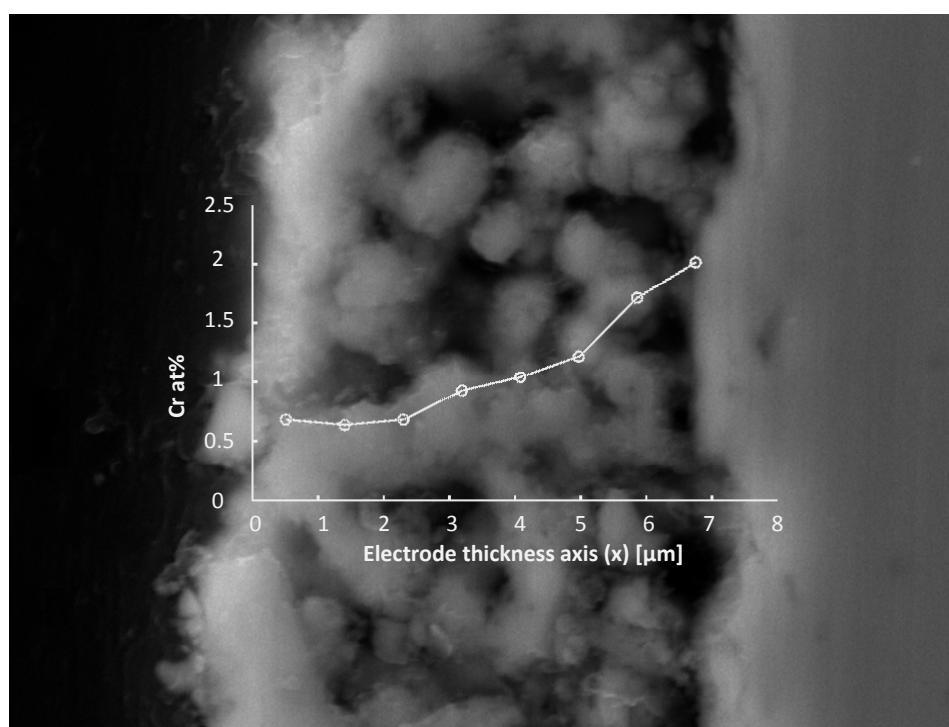
Figure 6.14. A nickelate ($Nd_2NiO_{4+\delta}$) cathode tested in presence of Cr. The deposited Cr is more evenly distributed than in the case of LSM-based composite cathodes.

Chapter 7

Conclusion and perspectives

7.1 Conclusion

- The experimental installation has a major impact on the scientific output in SOFC investigation. The measurement and identification of small variations of performance due to slow, simultaneous, interrelated processes over long time of operation require robust installations capable to give reliable and reproducible results. Moreover, testing time is a limitation in SOFC research since several months/years may be needed to conduct an experimental campaign. A segmented cell for multi-electrode testing solves these two issues, allowing simultaneous testing of segments under the same operating conditions and permitting to decrease n-fold the experimental time needed for the investigation.

- The variation of the microstructure is related to a variation in performance. The loss of performance takes place in two different ways: i) the reduction of the geometrical active area present in an electrode ii) the loss of contacts, creating isolated particles or clusters. This second phenomenon reduces the connectivity of the potentially active sites to the transport paths for the reactants and products of the electrochemical reactions; furthermore, the effective conductivity of the electronic and ionic phases is decreased. In the case of composite electrodes rich in one of the two phases (Ni/YSZ anodes), coarsening can cause loss of percolation of the minority phase and

163

the complete loss of contact, with catastrophic degradation and loss of the cell.

- Using micro-modelling based on percolation theory, it is possible to relate the coarsening of phases during operation to the degradation observed experimentally. The predictive capability of the model has been validated comparing theoretical results from simulation with electrochemical results obtained experimentally, which were found in good agreement. The predictive capability permits to find trade-offs between performance and durability and in particular, as explained for Ni/YSZ anodes, identify compositions that may have an initial good performance but would suffer catastrophic degradation because of the loss of electronic percolation during coarsening.

- Cr poisoning has been shown to be related to the local overpotential in the cathode. A model based on overpotential-driven deposition has been developed, putting in relation the distributed Cr deposition to the local electrochemical activity in cathode. This model, validated on the basis of experimental results, gives an insight and a prediction capability concerning the effect of several operative parameters on the degradation caused by Cr poisoning.

- The degradation due to Cr poisoning can be reduced by i) decreasing the amount of poisoning species present near the active sites during operation ii) decreasing the negative effect tied to the blocking of active sites. It has been shown theoretically and experimentally that the geometrical extension of the electrode (specifically its thickness) can create a "barrier effect", limiting the diffusion of Cr species. On the other hand, the composition (type and volume fraction of the electrolyte) can be optimized to give a two-fold advantage when in presence of Cr species: a higher efficiency in the ionic transport in the electrode leads to lower total overpotential and therefore to a lower amount of deposited Cr. Furthermore, poisoning pushes the electrochemical reaction to take place farther away from the dense electrolyte creating the need to move them for a longer way - and therefore causing a performance loss; in this sense, a more efficient transport of O^{2-} ions leads to a smaller

performance loss per quantity of deposited Cr. It has been predicted a three-fold increase in the life-time passing from 50%LSM/50%YSZ (standard composition for most LSM based cathodes) to 42%LSM/58%ScSZ electrodes (new composition).

7.2 Perspectives

- Microstructural characterization gives important information on the deactivation mechanisms and permits to calculate parameters that are needed for micro-modeling. Two techniques for 3D reconstruction with phase identification have been applied to cathode material and compared, giving a very good matching and resolution of the order of 10^1 nm. These promising results indicate that future investigation could rely on precise 3D characterization of electrode microstructures, in particular in the investigation of i) sintering processes ii) degradation due to microstructural variations during operation iii) relationship between microstructure and performance.

- Rietveld-XRD has been proved to be an effective investigation technique for the analysis of composite systems for identification of reaction phases. The analysis carried out on samples aged for different times, temperatures and pO_2 can provide useful data on the degradation by formation of insulating phases (zirconates) in the electrode. In order to be able to integrate this phenomenon in a model and have predictive capability, data must be gathered on both the thermodynamic stability of the zirconates *in real operation conditions* (e.g. low pO_2 near the interface) and on the kinetics of the formation of zirconate scales in the interface.

- The presence of Mn near the TPB can have a detrimental effect on SOFC operation, catalyzing the deposition of blocking species. Experimental results suggest that the Cr poisoning in Mn-rich cells is heavy and can even cause a morphological variation, the consumption of LSM and the physical blocking of the electrode/electrolyte interface. From the modelling point of view, a parameter ($i_{o,Cr}$) has been identified as a candidate for representing an increased affinity of the electrode towards poisoning.

New tests in this direction could be done for confirming the result and give more precise determination of deposited Cr profiles.

List of references

[1]   Kyoto protocol to the United Nations framework convention on climate change, In COP 3 report, document FCCC/CP/1997/7, Add.1 It., 1997.

[2]   N. Q. Minh. Ceramic fuel cells. *Journal of the American Ceramic Society*, 76(3):563–588, 1993.

[3]   S. Koch, P. V. Hendriksen, T. Jacobsen, and L. Bay.   Electrical behaviour of strontium-doped lanthanum manganite interfaces. *Solid State Ionics*, 176(9-10):861–869, 2005.

[4]   S. P. Jiang. Issues on development of $(La,Sr)MnO_3$ cathode for solid oxide fuel cells. *Journal of Power Sources*, 124(2):390–402, 2003.

[5]   H. Yokokawa, H. Tu, B. Iwanschitz, and A. Mai. Fundamental mechanisms limiting solid oxide fuel cell durability.   *Journal of Power Sources*, 182(2):400–412, 2008. Selected papers from the International Workshop on Degradation Issues in Fuel Cells.

[6]   S. C. Singhal. *Solid oxide fuel cells VI, PV 99-19*. The Electrochemical Society, Inc., Pennington, NJ, USA, 1999.

[7]   S. B. Adler.   Factors governing oxygen reduction in solid oxide fuel cell cathodes. *Chemical Reviews*, 104(10):4791–4844, 2004. PMID: 15669169.

[8]   H. Zhu and R. J. Kee. Modeling distributed charge-transfer processes in SOFC membrane electrode assemblies.   *Journal of The Electrochemical Society*, 155(7):B715–B729, 2008.

[9] A. Bieberle and L. J. Gauckler. Reaction mechanism of Ni pattern anodes for solid oxide fuel cells. *Solid State Ionics*, 135(1-4):337–345, 2000.

[10] J. H. Kuo, H. U. Anderson, and D. M. Sparlin. Oxidation-reduction behavior of undoped and Sr-doped LaMnO$_3$: Defect structure, electrical conductivity, and thermoelectric power. *Journal of Solid State Chemistry*, 87(1):55–63, 1990.

[11] S. P. Jiang. Sintering behavior of Ni/Y$_2$O$_3$-ZrO$_2$ cermet electrodes of solid oxide fuel cells. *Journal of Materials Science*, 38(18):3775–3782, 2003.

[12] A. Faes, A. Hessler-Wyser, D. Presvytes, C. G. Vayenas, and J. Van herle. Nickel-zirconia anode degradation and triple phase boundary quantification from microstructural analysis. *Fuel Cells*, 9(6):841–851, 2009.

[13] H. Tu and U. Stimming. Advances, aging mechanisms and lifetime in solid-oxide fuel cells. *Journal of Power Sources*, 127(1-2):284–293, 2004.

[14] J.-H. Lee, J.-W. Heo, D.-S. Lee, J. Kim, G.-H. Kim, H.-W. Lee, H. S. Song, and J.-H. Moon. The impact of anode microstructure on the power generating characteristics of SOFC. *Solid State Ionics*, 158(3-4):225–232, 2003.

[15] A. Hagen, R. Barfod, P. V. Hendriksen, Y.-L. Liu, and S. Ramousse. Degradation of anode supported SOFCs as a function of temperature and current load. *Journal of The Electrochemical Society*, 153(6):A1165–A1171, 2006.

[16] A. Hagen, Y. L. Liu, R. Barfod, and P. V. Hendriksen. Assessment of the cathode contribution to the degradation of anode-supported solid oxide fuel cells. *Journal of The Electrochemical Society*, 155(10):B1047–B1052, 2008.

[17] S. P. Jiang and W. Wang. Sintering and grain growth of (La,Sr)MnO$_3$ electrodes of solid oxide fuel cells under polarization. *Solid State Ionics*, 176(13-14):1185–1191, 2005.

[18] J. M. Vohs and R. J. Gorte. High-performance SOFC cathodes prepared by infiltration. *Advanced Materials*, 21(9):943–956, 2009.

[19] T. Kadowaki, T. Shiomitsu, E. Matsuda, H. Nakagawa, H. Tsuneizumi, and T. Maruyama. Applicability of heat resisting alloys to the separator of planar type solid oxide fuel cell. *Solid State Ionics*, 67(1-2):65–69, 1993.

[20] B. B. Ebbinghaus. Thermodynamics of gas phase chromium species: The chromium oxides, the chromium oxyhydroxides, and volatility calculations in waste incineration processes. *Combustion and Flame*, 93(1-2):119–137, 1993.

[21] S. Taniguchi, M. Kadowaki, H. Kawamura, T. Yasuo, Y. Akiyama, Y. Miyake, and T. Saitoh. Degradation phenomena in the cathode of a solid oxide fuel cell with an alloy separator. *Journal of Power Sources*, 55(1):73–79, 1995.

[22] H. Yokokawa, T. Horita, N. Sakai, K. Yamaji, M. E. Brito, Y. P. Xiong, and H. Kishimoto. Thermodynamic considerations on Cr poisoning in SOFC cathodes. *Solid State Ionics*, 177(35-36):3193–3198, 2006.

[23] S.P.S. Badwal, R. Deller, K. Foger, Y. Ramprakash, and J. P. Zhang. Interaction between chromia forming alloy interconnects and air electrode of solid oxide fuel cells. *Solid State Ionics*, 99(3-4):297–310, 1997.

[24] Y. Matsuzaki and I. Yasuda. Electrochemical properties of a SOFC cathode in contact with a chromium-containing alloy separator. *Solid State Ionics*, 132(3-4):271–278, 2000.

[25] T. Horita, Y. Xiong, H. Kishimoto, K. Yamaji, M. E. Brito, and H. Yokokawa. Chromium poisoning and degradation at $(La,Sr)MnO_3$ and $(La,Sr)FeO_3$ cathodes for solid oxide fuel cells. *Journal of The Electrochemical Society*, 157(5):B614–B620, 2010.

[26] N. H. Menzler, I. Vinke, and H. Lippert. Chromium poisoning of LSM cathodes - results from stack testing. *ECS Transactions*, 25(2):2899–2908, 2009.

[27] T. Horita, Y. Xiong, M. Yoshinaga, H. Kishimoto, K. Yamaji, M. E. Brito, and H. Yokokawa. Accelerated degradation of SOFC cathodes by Cr vapors. *ECS Transactions*, 25(2):2881–2888, 2009.

[28] T. Horita, Y. Xiong, M. Yoshinaga, H. Kishimoto, K. Yamaji, M. E. Brito, and H. Yokokawa. Determination of chromium concentration in solid oxide fuel cell cathodes: $(La,Sr)MnO_3$ and $(La,Sr)FeO_3$. *Electrochemical and Solid-State Letters*, 12(10):B146–B149, 2009.

[29] E. Konysheva, J. Mertens, H. Penkalla, L. Singheiser, and K. Hilpert. Chromium poisoning of porous composite cathode: Effect of cathode thickness and current density. *Journal of the Electrochemical Society*, 154(12):271–278, 2007.

[30] A. Neumann, N. H. Menzler, I. Vinke, and H. Lippert. Systematic study of chromium poisoning of LSM cathodes: Single cell tests. *ECS Meeting Abstracts*, 902(12):1496–1496, 2009.

[31] J. Guan, S. Zecevic, Y. Liu, P. Lam, R. Klug, M. Alinger, S. Taylor, B. Ramamurthi, R. Sarrafi-Nour, and S. Renou. Performance degradation of solid oxide fuel cells with metallic interconnects. *ECS Transactions*, 7(1):405–412, 2007.

[32] K. Hilpert, D. Das, M. Miller, D. H. Peck, and R. Weiss. Chromium vapor species over solid oxide fuel cell interconnect materials and their potential for degradation processes. *Journal of The Electrochemical Society*, 143(11):3642–3647, 1996.

[33] S. P. Jiang, J. P. Zhang, L. Apateanu, and K. Foger. Deposition of chromium species at Sr-doped $LaMnO_3$ electrodes in solid oxide fuel cells. I. mechanism and kinetics. *Journal of The Electrochemical Society*, 147(11):4013–4022, 2000.

[34] A. Mitterdorfer and L. J. Gauckler. $La_2Zr_2O_7$ formation and oxygen reduction kinetics of the $La_{0.85}Sr_{0.15}Mn_yO_3$, $O_{2,(g)}$YSZ system. *Solid State Ionics*, 111(3-4):185–218, 1998.

[35] H. Oppolzer. Analytics for materials. *Siemens-Review Special - R&D*, Fall 1996:5–7, 1996.

[36] S. K. Lau and S. C. Singhal. Potential electrode / electrolyte interactions in solid oxide fuel cells. In *Corrosion 85*, number 345, pages 1–9, 1985.

[37] H. Yokokawa. Understanding materials compatibility. *Annual Review of Materials Research*, 33(1):581–610, 2003.

[38] H. Yokokawa, S. Yamauchi, and M. Takafumi. Thermodynamic database MALT2 and its applications to high temperature materials chemistry. *Thermochimica acta*, 245:45–55, 1994.

[39] M. Chen, A. N. Grundy, B. Hallstedt, and L. J. Gauckler. Thermodynamic modeling of the La-Mn-Y-Zr-O system. *Calphad*, 30(4):489–500, 2006.

[40] G. Stochniol, E. Syskakis, and A. Naoumidis. Chemical compatibility between strontium-doped lanthanum manganite and yttria-stabilized zirconia. *Journal of the American Ceramic Society*, 78(4):929–932, 1995.

[41] N.Q. Minh and T. Takahashi. *Science and Technology of Ceramic Fuel Cells*. Elsevier, Amsterdam, 1995.

[42] A. Weber, R. Männer, B. Jobst, M. Schiele, H. Cerva, R. Waser, and E. Ivers-Tiffée. The influence of A-site-deficiency to the reaction kinetics of Sr doped La-manganite perovskite type SOFC-cathodes. In F.W. Poulsen, editor, *High Temperature Electrochemistry: Ceramics and Metals*. Risoe National Laboratory, 1996.

[43] M. J. Heneka and E. Ivers-Tiffée. In S. Linderoth, A. Smith, A. Bonanos, N. amd Hagen, L. Mikkelsen, K. Kammer, D. Lybye, P. V. Hendriksen, F. W. Poulsen, M. Mogensen, and W. G. Wang, editors, *Proceedings of the 26th Risoe International symposium on material science*, pages 215–222, Roskilde, Denmark, 2005. Risoe National Laboratory.

[44] M. Chen, Y. L. Liu, A. Hagen, P. V. Hendriksen, and F. W. Poulsen. LSM-YSZ reactions in different atmospheres. *Fuel Cells*, 9(6):833–840, 2009.

[45] J. A. M. Van Roosmalen and E. H. P. Cordfunke. The defect chemistry of LaMnO$_{3\pm\delta}$: 3. the density of (La,A)MnO$_{3+\delta}$ (A = Ca, Sr, Ba). *Journal of Solid State Chemistry*, 110(1):106–108, 1994.

[46] T. Kawada, N. Sakai, H. Yokokawa, and M. Dokiya. Electrical properties of transition-metal-doped YSZ. *Solid State Ionics*, 53-56(1):418–425, 1992.

[47] A. Nakajo, P. Tanasini, S. Diethelm, J. Van Herle, and D. Favrat. Electrochemical model of solid oxide fuel cell for simulation atthe stack level. part II: Implementation of degradation processes. *Journal of the Electrochemical Society*, submitted.

[48] D. Larrain, J. Van herle, and D. Favrat. Simulation of SOFC stack and repeat elements including interconnect degradation and anode reoxidation risk. *Journal of Power Sources*, 161(1):392–403, 2006.

[49] A. Faes, A. Nakajo, A. Hessler-Wyser, D. Dubois, A. Brisse, S. Modena, and J. Van herle. RedOx study of anode-supported solid oxide fuel cell. *Journal of Power Sources*, 193(1):55–64, 2009. cited By (since 1996) 10.

[50] A. Faes, H. L. Frandsen, M. Pihlatie, A. Kaiser, and D.R. Goldstein. Curvature and strength of Ni-YSZ solid oxide half-cells after RedOx treatments. *Journal of Fuel Cell Science and Technology*, 7(5):0510111–0510117, 2010. cited By (since 1996) 0.

[51] E. Perry Murray, T. Tsai, and S. A. Barnett. A direct-methane fuel cell with a ceria-based anode. *Nature*, 400:649–651, August 1999.

[52] K. Sasaki, K. Watanabe, K. Shiosaki, K. Susuki, and Y. Teraoka. Multi-fuel capability of solid oxide fuel cells. *Journal of Electroceramics*, 13:669–675, 2004. 10.1007/s10832-004-5174-z.

[53] Z. Cheng, S. Zha, and M. Liu. Influence of cell voltage and current on sulfur poisoning behavior of solid oxide fuel cells. *Journal of Power Sources*, 172(2):688–693, 2007. cited By (since 1996) 13.

[54] Y. Matsuzaki and I. Yasuda. The poisoning effect of sulfur-containing impurity gas on a SOFC anode: Part I. dependence on temperature, time, and impurity concentration. *Solid State Ionics*, 132(3-4):261–269, 2000.

[55] J. Van Herle and R. Vasquez. Conductivity of Mn and Ni-doped stabilized zirconia electrolyte. *Journal of the European Ceramic Society*, 24(6):1177–1180, 2004.

[56] C. Haering, A. Roosen, and H. Schichl. Degradation of the electrical conductivity in stabilised zirconia systems: Part I: yttria-stabilised zirconia. *Solid State Ionics*, 176(3-4):253–259, 2005.

[57] M. Hattori, Y. Takeda, J. H. Lee, S. Ohara, K. Mukai, T. Fukui, S. Takahashi, Y. Sakaki, and A. Nakanishi. Effect of annealing on the electrical conductivity of the Y_2O_3-ZrO_2 system. *Journal of Power Sources*, 131(1-2):247–250, 2004.

[58] S. B. Adler, J. A. Lane, and B. C. H. Steele. Electrode kinetics of porous mixed-conducting oxygen electrodes. *Journal of the Electrochemical Society*, 143(11):3554–3564, 1996.

[59] C. W. Tanner, K.-Z. Fung, and A. V. Virkar. The effect of porous composite electrode structure on solid oxide fuel cell performance. *Journal of The Electrochemical Society*, 144(1):21–30, 1997.

[60] S. Sunde. Monte carlo simulations of conductivity of composite electrodes for solid oxide fuel cells. *Journal of The Electrochemical Society*, 143(3):1123–1132, 1996.

[61] S. Sunde. Monte carlo simulations of polarization resistance of composite electrodes for solid oxide fuel cells. *Journal of The Electrochemical Society*, 143(6):1930–1939, 1996.

[62] S. Sunde. Calculations of impedance of composite anodes for solid oxide fuel cells. *Electrochimica Acta*, 42(17):2637–2648, 1997.

[63] P. Costamagna, P. Costa, and V. Antonucci. Micro-modelling of solid oxide fuel cell electrodes. *Electrochimica Acta*, 43(3-4):375–394, 1998.

[64] P. Costamagna, P. Costa, and E. Arato. Some more considerations on the optimisation of cermet solid oxide fuel cell. *Electrochemica Acta*, 43(8):967–972, 1997.

[65] Z. T. Xia, S. H. Chan, and K. A. Khor. An improved anode micro model of SOFC. *Electrochemical and Solid-State Letters*, 7(3):A63–A65, 2004.

[66] D. Stauffer and Aharony. A. *Introduction to percolation theory*. Taylor & Francis, 1994.

[67] M. Sahimi. *Applications of percolation theory*. Taylor & Francis, 1994.

[68] P. J. Flory. Molecular size distribution in three dimensional polymers. I. gelation. *Journal of the American Chemical Society*, 63(11):3083–3090, 1941.

[69] I. A. Nairn, M. J. Smith, and C. A. Vincent. Mixed-phase electrodes in solid state cells. *Solid State Ionics*, 9-10(Part 1):383–390, 1983.

[70] K. D. M. Harris, M. D. Rogers, and C. A. Vincent. A comparison between [']mixed phase electrode' and percolation models for composite electrodes in solid state cells. *Solid State Ionics*, 18-19(Part 2):833–837, 1986.

[71] F.F. Lange, L. Atteraas, F. Zok, and J. R. Porter. Deformation consolidation of metal powders containing steel inclusions. *Acta Metallurgica et Materialia*, 39(2):209–219, 1991.

[72] D. Bouvard and F.F. Lange. Relation between percolation and particle coordination in binary powder mixtures. *Acta Metallurgica et Materialia*, 39(12):3083–3090, 1991.

[73] *Proc. Fourth Int. Conf. on Soil Mechanics and Foundation Engineering*, 1983.

[74] D. W. Dees, T. D. Claar, T. E. Easler, D. C. Fee, and F. C. Mrazek. Conductivity of porous Ni/ZrO$_2$-Y$_2$O$_3$ cermets. *Journal of The Electrochemical Society*, 134(9):2141–2146, 1987.

[75] A. Barbucci, R. Bozzo, G. Cerisola, and P. Costamagna. Characterisation of composite SOFC cathodes using electrochemical impedance spectroscopy. analysis of Pt/YSZ and LSM/YSZ electrodes. *Electrochimica Acta*, 47(13-14):2183–2188, 2002.

[76] J.-H. Lee, H. Moon, H.-W. Lee, J. Kim, J.-D. Kim, and K.-H. Yoon. Quantitative analysis of microstructure and its related electrical property of SOFC anode, Ni-YSZ cermet. *Solid State Ionics*, 148(1-2):15–26, 2002.

[77] U. Anselmi-Tamburini, G. Chiodelli, M. Arimondi, F. Maglia, G. Spinolo, and Z. A. Munir. Electrical properties of Ni/YSZ cermets obtained through combustion synthesis. *Solid State Ionics*, 110(1-2):35–43, 1998.

[78] S. K. Pratihar, A. Dassharma, and H. S. Maiti. Processing microstructure property correlation of porous Ni-YSZ cermets anode for SOFC application. *Materials Research Bulletin*, 40(11):1936–1944, 2005.

[79] M. Suzuki and T. Oshima. Estimation of the coordination number in a multi-component mixture of spheres. *Powder Technology*, 35(2):159–166, 1983.

[80] C.-H. Kuo and P. K. Gupta. Rigidity and conductivity percolation thresholds in particulate composites. *Acta Metallurgica et Materialia*, 43(1):397–403, 1995.

[81] M. Juhl, S. Primdahl, C. Manon, and M. Mogensen. Performance/structure correlation for composite SOFC cathodes. *Journal of Power Sources*, 61(1-2):173–181, 1996.

[82] V. Dusastre and J. A. Kilner. Optimisation of composite cathodes for intermediate temperature SOFC applications. *Solid State Ionics*, 126(1-2):163–174, 1999.

[83] J. Deseure, L. Dessemond, Y. Bultel, and E. Siebert. Modelling of a SOFC graded cathode. *Journal of the European Ceramic Society*, 25(12):2673–2676, 2005. Elecro-ceramics IX.

[84] L. C. R. Schneider, C. L. Martin, Y. Bultel, L. Dessemond, and D. Bouvard. Percola-tion effects in functionally graded SOFC electrodes. *Electrochimica Acta*, 52(9):3190–3198, 2007.

[85] L. Holzer, B. Iwanschitz, Th. Hocker, B. Münch, M. Prestat, D. Wiedenmann, U. Vogt, P. Holtappels, J. Sfeir, A. Mai, and Th. Graule. Microstructure degrada-tion of cermet anodes for solid oxide fuel cells: Quantification of nickel grain growth in dry and in humid atmospheres. *Journal of Power Sources*, 196(3):1279–1294, February 2011.

[86] R. Barfod, A. Hagen, S. Ramousse, P.V. Hendriksen, and M. Mogensen. Break down of losses in thin electrolyte SOFCs. *Fuel Cells*, 6(2):141–145, 2006.

[87] R. Barfod, M. Mogensen, T. Klemensoe, A. Hagen, Y. L. Liu, and P. V. Hendriksen. Detailed characterization of anode supported SOFCs by impedance spectroscopy. *Journal of the Electrochemical Society*, 154(4):B371–B378, 2007.

[88] K. V. Jensen, R. Wallenberg, I. Chorkendorff, and M. Mogensen. Effect of impurities on structural and electrochemical properties of the Ni-YSZ interface. *Solid State Ionics*, 160(1-2):27–37, 2003.

[89] P. Tanasini, J. A. Schuler, Z. Wuillemin, M. L. Ben Ameur, C. Comninellis, and J. Van herle. Segmented cell testing for cathode parameter investigation. *Journal of Power Sources*, In Press, corrected proof. doi:10.1016/j.jpowsour.2010.08.034.

[90] Z. Wuillemin, A. Nakajo, A. Müller, A. J. Schuler, S. Diethelm, J. Van herle, and D. Favrat. Locally-resolved study of degradation in a SOFC repeat-element. *ECS Transactions*, 25(2 PART 1):457–466, 2009.

[91] Z. Wuillemin. *Experimental and modeling investigations on local performance and local degradation in solid oxide fuel cells.* PhD thesis, EPFL, Lausanne, 2009.

[92] J. Eaves. *Promotion électrochimique des catalyseurs à base de rhodium et d'iridium.* PhD thesis, EPFL, 2004.

[93] S. Widmer. *Mécanismes de dépolarisation de la réduction de l'oxygène sur des interfaces structurées à haute temperature.* PhD thesis, EPFL, Lausanne, 1997.

[94] S. H. Jensen, A. Hauch, P. V. Hendriksen, M. Mogensen, N. Bonanos, and Jacobsen T. A method to separate process contributions in impedance spectra by variation of test conditions. *Journal of the Electrochemical Society,* 154(12):B1325–B1330, 2007.

[95] J. Ayache, L. Beaunier, J. Boumendil, Ehret G., and Laub D. *Guide de Preparation des Echantillons pour la Microscopie Electronique en Trasmission - Tome II.* Université de Saint-Etienne, Saint-Etienne, 2007.

[96] C. Monachon, A. Hessler-Wyser, A. Faes, J. Van herle, and E. Tagliaferri. Rapid preparation and SEM microstructural characterization of nickel-yttria-stabilized zirconia cermets. *Journal of the American Ceramic Society,* 91(10):3405–3407, 2008.

[97] J. A. Schuler, P. Tanasini, A. Hessler-Wyser, and J. Van herle. Rapid chromium quantification in solid oxide fuel cell cathodes. *Scripta Materialia,* 63(8):895–898, 2010.

[98] P. Tanasini, M. Cannarozzo, P. Costamagna, A. Faes, J. Van herle, A. Hessler-Wyser, and C. Comninellis. Experimental and theoretical investigation of degradation mechanisms by particle coarsening in SOFC electrodes. *Fuel Cells,* 9(5):740–752, 2009.

[99] P. Costamagna, M. Panizza, G. Cerisola, and A. Barbucci. Effect of composition on the performance of cermet electrodes. experimental and theoretical approach. *Electrochimica Acta,* 47(7):1079–1089, 2002.

[100] E. Siebert, A. Hammouche, and M. Kleitz. Impedance spectroscopy analysis of La$_{1-x}$Sr$_x$MnO$_3$-yttria-stabilized zirconia electrode kinetics. *Electrochimica Acta*, 40(11):1741–1753, 1995.

[101] S. Koch, M. Mogensen, P. V. Hendriksen, N. Dekker, and B. Rietveld. Electrode activation and passivation of solid oxide fuel cell electrodes. *Fuel Cells*, 2(2):117–122, 2006.

[102] M.J. Jørgensen, S. Primdahl, and M. Mogensen. Characterisation of composite SOFC cathodes using electrochemical impedance spectroscopy. *Electrochemica Acta*, 44(24):4195–4201, 1999.

[103] F.S. Baumann, J. Fleig, M. Konuma, U. Starke, H.U. Habermeier, and J. Maier. Strong performances improvement of La$_{0.6}$Sr$_{0.4}$Co$_{0.8}$Fe$_{0.2}$O$_{3-\delta}$ SOFC cathodes by electrochemical activation. *Journal of The Electrochemical Society*, 152(10):A2074–A2079, 2005.

[104] A. Weber, R. Manner, R. Waser, and E. Ivers-Tiffée. Interaction between microstructure and electrical properties of screen printed cathodes in SOFC single cells. *Denki Kagaku*, 64(6):582–589, 1996.

[105] S. P. Jiang and J. G. Love. Origin of the initial polarization behavior of Sr-doped LaMnO$_3$ for O$_2$ reduction in solid oxide fuel cells. *Solid State Ionics*, 138(3-4):183–190, 2001.

[106] J. A. Schuler, P. Tanasini, A. Hessler-Wyser, C. Comninellis, and J. Van herle. Cathode thickness-dependent tolerance to Cr-poisoning in solid oxide fuel cells. *Electrochemistry Communications*, 12(12):1682–1685, 2010.

[107] A. Nakajo. *Thermomechanical and electrochemical degradation in anode-supported solid oxide fuel cell stack*. PhD thesis, EPFL, 2011.

[108] J. A. Schuler, C. Gehrig, Z. Wuillemin, A. J. Schuler, J. Wochele, C. Ludwig, A. Hessler-Wyser, and J. Van herle. Air side contamination in solid oxide fuel cell stack testing. *Journal of Power Sources*, In Press, Corrected Proof:–, 2010.

[109] Y. Arachi, H. Sakai, O. Yamamoto, Y. Takeda, and N. Imanishai. Electrical conductivity of the ZrO_2-Ln_2O_3 (Ln=lanthanides) system. *Solid State Ionics*, 121(1-4):133–139, 1999.

[110] K. N. Grew, Y. S. Chu, J. Yi, A. A. Peracchio, J. R. Jr. Izzo, Y. Hwu, F. De Carlo, and W. K. S. Chiu. Nondestructive nanoscale 3D elemental mapping and analysis of a solid oxide fuel cell anode. *Journal of The Electrochemical Society*, 157(6):B783 – B792, 2010.

[111] K. N. Grew, A. A. Peracchio, A. S. Joshi, J. R. Jr. Izzo, and W. K. S. Chiu. Characterization and analysis methods for the examination of the heterogeneous solid oxide fuel cell electrode microstructure. part 1: Volumetric measurements of the heterogeneous structure. *Journal of Power Sources*, 195(24):7930 – 7942, 2010.

[112] K. N. Grew, A. A. Peracchio, and W. K. S. Chiu. Characterization and analysis methods for the examination of the heterogeneous solid oxide fuel cell electrode microstructure: Part 2. quantitative measurement of the microstructure and contributions to transport losses. *Journal of Power Sources*, 195(24):7943 – 7958, 2010.

[113] K.-W. Nam, M. G. Kim, and K.-B. Kim. In situ Mn K-edge X-ray absorption spectroscopy studies of electrodeposited manganese oxide films for electrochemical capacitors. *The Journal of Physical Chemistry C*, 111(2):749 – 758, 2007.

[114] Y. J. Liu, P. P. Zhu, B. Chen, J. Y. Wang, Q. X. Yuan, W. X. Huang, H. Shu, E. R. Li, X. S. Liu, K. Zhang, H. Ming, and Z. Y. Wu. A new iterative algorithm to reconstruct the refractive index. *Physics in Medicine and Biology*, 52(12):L5, 2007.

[115] J. A. Schuler, H. Lübbe, A. Hessler-Wyser, and J. Van herle. Cr-tolerance in Nd-nickelate based solid oxide fuel cell material. *in preparation*.

Curriculum Vitae

Education

- 2007–2011 PhD in Chemical Engineering, Swiss Federal Institute of Technology (EPFL) in Lausanne, Switzerland ; Institute of Chemical Science and Engineering. Thesis director : Prof. Christos Comninellis ; co-director : Dr. MER Jan Van herle

- 2006 Master science in Industrial Chemistry – Università di Genova. Specialization in process membranes (distinction with honor)

- 2004 Bachelor Science in Industrial Chemistry – Università di Genova. Specialization in wastewater treatment (distinction with honor) ; "Leonardo grant" awarded for a three-month bachelor diploma work at EPFL

- 2001-2006 Industrial Chemistry studies – Università di Genova.

Publications

- G. J. Nelson, W. M. Harris, J. J. Lombardo, J. R. Jr. Izzo, W. K. S. Chiu, P. Tanasini, M. Cantoni, J. Van Herle, C. Comninellis, J. C. Andrews, Y. Liu, P. Pianetta, and Y. S. Chu. 3D elemental mapping of the composite LSM-YSZ SOFC cathode microstructure using XCT and FIB-SEM. Electrochemical Communications, submitted

- A. Nakajo, P. Tanasini, S. Diethelm, J. Van Herle, and D. Favrat. Electrochemical model of solid oxide fuel cell for simulation at the stack level. part II : Implementation of degradation processes. Journal of the Electrochemical Society, submitted.

- A. Faes, Z. Wuillemin, P. Tanasini, N. Accardo, S. Modena, H. J. Schindler, M. Cantoni, H. Luebbe, S. Diethelm, A. Hessler-Wyser, and J. Van herle. Design of experiment approach applied to RedOx tolerance of anode supported SOFC part II : Electrochemical and microstructural characterization of tape-cast cells. Journal of Power Sources, In Press, corrected proof. doi : 10.1016/j.jpowsour.2010.11.146.

- A. Faes, Z. Wuillemin, P. Tanasini, N. Accardo, and J. Van herle. Redox stable Ni-YSZ anode support in solid oxide fuel cell stack configuration. Journal of Power Sources, In Press, corrected proof. doi : 10.1016/j.jpowsour.2010.11.047.

- P. Tanasini, J. A. Schuler, Z. Wuillemin, M. L. Ben Ameur, C. Comninellis, and J. Van herle. Segmented cell testing for cathode parameter investigation. Journal of Power Sources, In Press, corrected proof. doi :10.1016/j.jpowsour.2010.08.034.

- J. A. Schuler, P. Tanasini, A. Hessler-Wyser, C. Comninellis, and J. Van herle. Cathode thickness-dependent tolerance to Cr-poisoning in solid oxide fuel cells. Electrochemistry Communications, 12(12) :1682-1685, 2010.

- J. A. Schuler, P. Tanasini, A. Hessler-Wyser, and J. Van herle. Rapid chromium quantication in solid oxide fuel cell cathodes. Scripta Materialia, 63(8) :895-898, 2010.

- P. Tanasini, M. Cannarozzo, P. Costamagna, A. Faes, J. Van herle, A. Hessler-Wyser, and C. Comninellis. Experimental and theoretical investigation of degradation mechanisms by particle coarsening in SOFC electrodes. Fuel Cells, 9(5) :740-752, 2009.

Communications

- Oral presentation in International Symposium on Electrochemistry for Energy Conversion August 2009, Three Gorges, China.

- Oral presentation and one poster in 9th European FC forum, June 2010, Lucerne, Switzerland